AFRL-SA-AR-TR-10-0344

[In-Situ Adhesive Bond Assessment]

Todd, Michael, Lanza di Scalea, Francesco Srivastava,
Ankit Fasel, Tim Bartoli, Ivan

The Regents of the University of California; University of California, San Diego

AUGUST 2010
Final Report

DISTRIBUTION A: Distribution approved for public release.

AIR FORCE RESEARCH LABORATORY
AF OFFICE OF SCIENTIFIC RESEARCH (AFOSR)/RSA
ARLINGTON, VIRGINIA 22203
AIR FORCE MATERIEL COMMAND

20101202160

AFRL-SR-AR-TR-10-0344

REPORT DOCUMENTATION PAGE

PLEASE DO NOT RETURN YOUR FORM TO THE ABOVE ORGANIZATION.

1. REPORT DATE *(DD-MM-YYYY)*
13-08-2010

2. REPORT TYPE
Final Technical Report

3. DATES COVERED *(From - To)*
Jan 2007 - May 2010

4. TITLE AND SUBTITLE
In-Situ Adhesive Bond Assessment

5a. CONTRACT NUMBER

5b. GRANT NUMBER
FA9550-07-1-0016

5c. PROGRAM ELEMENT NUMBER

6. AUTHOR(S)
Todd, Michael
Lanza di Scalea, Francesco
Srivastava, Ankit
Fasel, Tim
Bartoli, Ivan

5d. PROJECT NUMBER

5e. TASK NUMBER

5f. WORK UNIT NUMBER

7. PERFORMING ORGANIZATION NAME(S) AND ADDRESS(ES)
The Regents of the University of California; University of California, San Diego
9500 Gilman Drive, Mail Code 0934
La Jolla, CA 92093-0934

8. PERFORMING ORGANIZATION REPORT NUMBER

9. SPONSORING/MONITORING AGENCY NAME(S) AND ADDRESS(ES)
Air Force Office of Scientific Research
875 North Randolph Street
Arlington, VA 22203-1768

RSA

10. SPONSOR/MONITOR'S ACRONYM(S)
AFOSR

11. SPONSOR/MONITOR'S REPORT NUMBER(S)

12. DISTRIBUTION/AVAILABILITY STATEMENT
A. Approved for public release; distribution unlimited.

13. SUPPLEMENTARY NOTES

14. ABSTRACT

This project considered the optimal application of ultrasonic guided waves (using sparse piezoelectric transducer arrays) for probing composite skin-to-spar adhesive joints used in aerospace structural design for various forms of defects such as delamination and poorly-cured adhesive. An important part of the project was developing compensation in assessment algorithms for changing temperature effects corresponding to normal aircraft operations (-40 °C to +60 °C). Specifically, three fundamental research areas were considered: (1) analytical modeling/experimental validation of wave propagation that accounts for temperature effects on the transducer piezo-mechanical properties over the flight temperature range listed above the transducer-structure interaction, and the structure wave dispersion properties; (2) further development of a Global-Local method to simulate the interaction of the guided waves with structural defects in isotropic and composite panels that takes advantage of the Semi-Analytical Finite Element (SAFE) approach for the "global" simulation that significantly reduces computational time; and (3) development of physics-based and data-based (using a two-step detection/classification procedure) algorithms for assessing the in-situ state of an adhesive bond.

15. SUBJECT TERMS
structural health monitoring, ultrasonics, guided waves, NDE, adhesive bonds

16. SECURITY CLASSIFICATION OF:			**17. LIMITATION OF ABSTRACT**	**18. NUMBER OF PAGES**	**19a. NAME OF RESPONSIBLE PERSON**
a. REPORT	**b. ABSTRACT**	**c. THIS PAGE**			Todd, Michael
U	U	U	SAR	97	**19b. TELEPHONE NUMBER** *(Include area code)* (858) 534-5951

FINAL TECHNICAL REPORT

"In-Situ Adhesive Bond Assessment for Aerospace Structures"

Grant Number FA9550-07-1-0016
Period of Performance: Dec 2006 – May 2010

Michael Todd (PI), Francesco Lanza di Scalea (Co-PI)
Ankit Srivastava, Tim Fasel, Ivan Bartoli

Technical Points of Contact:

Michael Todd (PI)
University of California San Diego
9500 Gilman Drive
Mail Code 0085
La Jolla, CA 92093-0085
Phone: (858) 534-5951
Fax: (858) 534-6373
Email: mdt@ucsd.edu

Francesco Lanza di Scalea (Co-PI)
University of California San Diego
9500 Gilman Drive
Mail Code 0085
La Jolla, CA 92093-0085
Phone: (858) 822-1458
Fax: (858) 534-6373
Email: flanza@ucsd.edu

Business Point of Contact:

Michael Brown
University of California San Diego
Office of Contracts and Grants Administration
9500 Gilman Drive 0934
La Jolla, CA 92093-0934
Phone: (858) 534-2972
Fax: (858) 534-0280
Email: m2brown@ucsd.edu

UCSD Jacobs | Structural Engineering

ABSTRACT

This 3-year AFOSR-sponsored project "In-Situ Adhesive Bond Assessment for Aerospace Structures" (#FA9550-07-1-0016) considered the optimal application of ultrasonic guided waves (using sparse piezoelectric transducer arrays) for probing composite skin-to-spar adhesive joints used in aerospace structural design for various forms of defects such as delamination and poorly-cured adhesive. An important part of the project was developing compensation in assessment algorithms for changing temperature effects corresponding to normal aircraft operations (-40 °C to +60 °C). Specifically, this project considered three fundamental research areas: (1) analytical modeling and experimental validation of wave propagation that accounts for temperature effects on the transducer piezo-mechanical properties over the flight temperature range listed above the transducer-host structure interaction, and the host structure wave dispersion properties; (2) further development of a Global-Local (GL) method to simulate the interaction of the guided waves with structural defects in isotropic and composite panels that takes advantage of the Semi-Analytical Finite Element (SAFE) approach for the "global" simulation that significantly reduces computational time; and (3) development of physics-based (from parts 1 and 2 above) and data-based (using a novel two-step detection and classification procedure rooted in outlier analysis and extreme value statistics) algorithms for assessing the in-situ state of a composite adhesive bond with regards to delamination and bond cure failure modes. All validation experiments were conducted on a Carbon-Fiber Reinforced Plastic (CFRP) $[0/\pm45/0]_S$ laminate subjected to the -40 °C to +60 °C temperature excursion.

EXECUTIVE SUMMARY

This report summarizes the key findings in the three research areas listed above and lists all publications that resulted from the project. This project funded the Ph.D. degree completion of two graduate student researchers in the Department of Structural Engineering at University of California San Diego (Ankit Srivastava and Tim Fasel), who were supervised and mentored by the PI Michael Todd and the Co-PI Francesco Lanza di Scalea. A quad chart summary of the project is included in Figure 1 below.

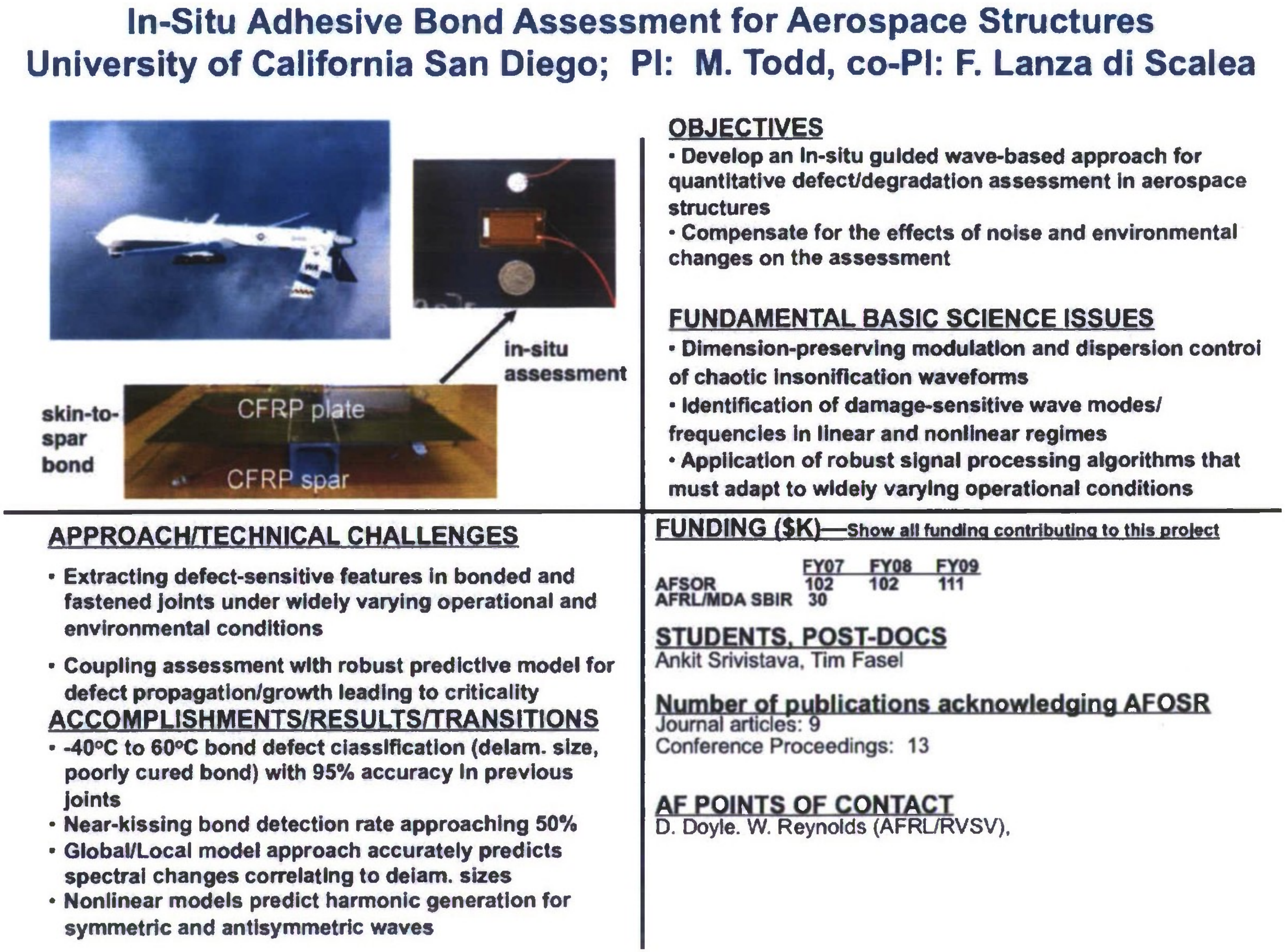

In-Situ Adhesive Bond Assessment for Aerospace Structures
University of California San Diego; PI: M. Todd, co-PI: F. Lanza di Scalea

OBJECTIVES

- Develop an In-situ guided wave-based approach for quantitative defect/degradation assessment in aerospace structures
- Compensate for the effects of noise and environmental changes on the assessment

FUNDAMENTAL BASIC SCIENCE ISSUES

- Dimension-preserving modulation and dispersion control of chaotic insonification waveforms
- Identification of damage-sensitive wave modes/ frequencies in linear and nonlinear regimes
- Application of robust signal processing algorithms that must adapt to widely varying operational conditions

APPROACH/TECHNICAL CHALLENGES

- Extracting defect-sensitive features in bonded and fastened joints under widely varying operational and environmental conditions
- Coupling assessment with robust predictive model for defect propagation/growth leading to criticality

ACCOMPLISHMENTS/RESULTS/TRANSITIONS

- -40°C to 60°C bond defect classification (delam. size, poorly cured bond) with 95% accuracy in previous joints
- Near-kissing bond detection rate approaching 50%
- Global/Local model approach accurately predicts spectral changes correlating to delam. sizes
- Nonlinear models predict harmonic generation for symmetric and antisymmetric waves

FUNDING ($K)—Show all funding contributing to this project

	FY07	FY08	FY09
AFSOR	102	102	111
AFRL/MDA SBIR	30		

STUDENTS, POST-DOCS

Ankit Srivistava, Tim Fasel

Number of publications acknowledging AFOSR

Journal articles: 9
Conference Proceedings: 13

AF POINTS OF CONTACT

D. Doyle. W. Reynolds (AFRL/RVSV),

Figure 1. Final "quad chart" summary of AFOSR project #FA9550-07-1-0016.

The first part of this project has developed a model to predict the amplitude spectrum of pitch-catch guided-wave signals in composite plates probed by MFC piezocomposite transducers. The model accounts for the transducer piezo-mechanical properties, the transducer-plate interaction through shear-lag effects, and the substrate plate properties, all of which can be parametrized with temperature. Theoretical and experimental results obtained on a $[0/\pm45/0]_S$ CFRP laminate between -40 °C and 60 °C show substantial changes in the predominant s_0-mode amplitude (as high as 40% change from the ambient-temperature value). Little change, instead, is seen in the wavelength tuning points (maxima and zeros in the response). It was also observed that the signal amplitude follows two opposite trends below and above ambient temperature.

These findings were applied to the detection of bond defects in a CFRP skin-to-spar adhesive joint. The defects considered were a region of poorly-cured adhesive (50% degradation in stiffnesses) and two different sizes of disbonds. The study used an s_0 ultrasonic frequency (~200 kHz) that corresponded to a wavelength tuning peak for the MFC transducers, as well as to a mode-coupling condition for the multilayered joint structure. The strength of transmission of this frequency was used to monitor bond state in the (-40 °C to 60 °C) temperature range. It was found that a multivariate Outlier Analysis using 8 representative signal features may be successful in detecting the bond defects within the temperature excursions. Correct defect classification was obtained when the baseline distribution for the analysis was partitioned in two regions, below ambient temperature (-40 °C to 20 °C) and above ambient temperature (20 °C to 60 °C). In an on-board system, this suggests that the defects examined can be successfully detected by toggling the baseline between only two operational conditions: in-flight and storage. There are several assumptions in the present work; the model assumes plane waves, thin transducers and neglects damping in the substrate plate. Also, the results on the bond defect detection only apply to the specific CFRP skin-to-spar joint tested. Different choices of wave frequency, Feature Vector dimension, and baseline distribution will likely be required for different applications.

This second part of the project has demonstrated the use of SAFE in a Global-Local framework which allows extracting information on guided waves scattered by defects in isotropic and layered anisotropic plates for quantitative structural health monitoring. The advantage of SAFE is its ability to handle the complex geometry of layered composites in a computationally efficient manner. The method was used in cases of notch-like defects in aluminum plates and delamination-like defects in layered composites. Both reflected and transmitted spectra of propagating modes were predicted. It should be noted that two different discretization are done in the solution of the problem. These affect the accuracy of the solution in different limiting regimes. For example, the thickness profile of the out of plane displacement component of the S_0 mode in an Aluminum plate varies from being approximately linear at an fd value of 0.5 to a half wavelength sinusoid at $fd = 3.0$. This indicates that the thickness discretization of the Global part in Global-Local should be increased to adequately model the increasing nonlinear thickness variation of the modeshape as the frequency is increased. Higher order modes exhibit a more nonlinear modeshape compared to lower order modes. The mode A_2, for instance, has more wavelengths in its displacement thickness profile at $fd = 5$ than A_1 has at the same fd value. Therefore, in general, a higher order mode needs a finer thickness discretization at the same frequency than a lower order mode in order to better approximate the true modeshape.

The local discretization for the Finite Element part of Global-Local should also vary with frequency and the modes under consideration. At any given frequency, modes with shorter wavelengths require a finer FE discretization for good approximation. Modes with low phase velocities in the dispersion curve, therefore, require more finite elements per unit propagation distance for an accurate representation in the summation solution. For isotropic structures like an aluminum plate, since all the modes asymptotically approach a constant phase velocity (S_0 and A_0 converge to the Rayleigh surface wave velocity; higher order modes converge to shear wave velocity), the FE discretization should be made finer as higher frequencies are considered. It was also shown that the wave time histories may be extracted from these models for an arbitrary excitation. The results shown are limited to a 2-D study. The extension of the work to 3-D cases and to full, complete adhesive bond assessment should be the subject of future work.

The third part of the project developed a data-driven approach for in-situ bond state characterization to complement the physics-based modeling and characterization of the first two parts. Of particular interest was robustness of the algorithm to the widely-varying operational temperature changes noted previously that aircraft experience during flight and ground operations. Attention was focused on a combined unsupervised and supervised learning scheme, where the difference between the two is that examples of delaminated bonds or bonds with improper cure were obtained to support the supervised step. Chaotically-modulated guided waves were created and optimized (in a detection sense) and used as probes to perform the assessment by building both time- and state-space domain models and using statistical modeling for performing damage classification under Type I/II error control. The use of chaotic modulation is motivated by the extreme sensitivity to its subsequent filtering from scattering of bond defect changes; rather than focusing on specific mode energy or mode conversion using single-tone bursts, the rich phase structure of chaos was shown to be a sensitive probe in this application. Multiple chaotic ultrasonic excitation formats were explored, including short-time chaotic wave packets and long-time chaotic bulk insonification, in which the diffuse, reverberant wave field was examined to identify structural changes. This method of insonification, in addition to enhanced pattern recognition techniques, allows this damage detection scheme to be employed on complex structural geometries (such as joints or bonds) with which standard ultrasonic-based NDE/SHM methods cannot be used.

In this approach, auto-regressive (AR) predictive models (linear time series predictors) are used to generate expected input/output relationships among transducer pairs in an ultrasonic array. Both the model coefficients and the baseline model's predictive power (characterized through some measure of prediction error) are used simultaneously to accomplish both detection and characterization of the defects. The primary feature is a vector consistency criterion (VCC) that essentially looks at the relative orthogonality of any two vectors constructed from a list of AR coefficients. The use of the VCC metric, with appropriate extreme value statistics models as described in detail below, allowed for detection/classification rates approaching 95% for various delamination sizes tested on the CFRP testbed described above. Robustness to temperature variability was accomplished by parameterizing the AR coefficients as a function of temperature and using minimum-distance fitting to choose the appropriate temperature normalization in-situ so that such effects are wrapped into the assessment procedure. This approach resulted in detection/classification rates being maintained at 90% across the operating temperature range.

1. INTRODUCTION

Many Air Force platforms, e.g., C/KC-135, B-52H, C-5A, and C-130, are being asked to provide service past their originally intended design lives. Condition-based monitoring (CBM) strategies can allow maintaining such assets in readiness while reducing life cycle costs and preserving life safety. Adhesively-bonded structural joint assemblies, including lap-shear, tear strap-to-skin joints, and composite-to-metal joints such as boron epoxy repair patches for aluminum panels, are among the most critical components of these and other aircraft structures. Wear, fatigue, and corrosion (all often exacerbated by widely fluctuating operating environments), and even poor manufacturing practice make such joint assemblies a common failure point. Assessing the structural state of adhesive bonds is critical to ensuring the safe performance of the aircraft.

Ultrasonic testing remains the most widely used technique for bond testing in the aerospace industry (Guyott et al. 1986). The popular Fokker bond tester, for example, is based on ultrasonic principles. Conventional ultrasonic bond inspection uses normally-incident bulk wave spectroscopy done in pre-flight or post-flight tests (Figure 1a). This method consists of measuring the frequency-dependent reflection coefficients of ultrasonic waves propagating through the bonded structure in the Megahertz frequency range (Guyott and Cawley 1986). The main drawback of this technique is the limited inspection range that makes the method too "local" to be practical for continuous monitoring. At the same time, "global" structural monitoring techniques, such as those based on vibration data, work at frequencies often too low for the scale of typical bond defects, particularly when the target flaws are at early growth stages.

As an alternative, Guided Ultrasonic Waves (GUWs) operating in the tens to hundreds of kilohertz range are being increasingly used for in-situ monitoring purposes. By exploiting the waveguide geometry of the structure, GUWs provide the large area coverage of the "global" methods while retaining the defect detection sensitivity of the "local" methods (Figure 1b). GUWs provide a number of features that are naturally sensitive to bond state, including wave velocity, amplitude, frequency content, and dynamic state representation (the latter of which will be a major component of this project). GUWs also offer the unique possibility of maximizing the sensitivity to different types of bond conditions by exciting the appropriate cross-sectional mode shapes through the selection of the corresponding frequency-velocity (dispersive) combinations or by exploiting novel features from user-tailored GUWs (such as chaotic GUWs).

Work has been performed in the past on the effects of temperature on guided-wave measurements in composite components, although no previous study has examined the case of adhesive joints. The general conclusion is that temperature variations induce changes in amplitude and phase of guided-wave signals. This was found as applied to the cases of sandwich panels at the low temperature of -90 °C (Blaise and Chang 2001), aluminum plates at the moderately high temperatures of 35 °C to 85 °C (Lee et al. 2003, Chambers et al. 2006), and aluminum plates at extremely high temperatures up to 230 °C (Schulz et al. 2003). Other studies on temperature effects have been conducted in the context of reverberating guided-wave signals (acousto-ultrasonics). These included ranges of 35 °C to 85 °C (Konstantinidis et al. 2006), and 5 °C to 40 °C (Lu and Michaels 2005, Michaels and Michaels 2005). Very recently, theoretical models incorporating temperature effects were developed to predict guided-wave pitch-catch signals recorded by either monolithic Pb(Zr-Ti)O3-PZT patches (Raghavan and Cesnik 2007, Lanza di Scalea and Salamone 2008) or Macro-Fiber Composite-MFC patches (Lanza di Scalea and Salamone 2008). The application of these theoretical models was limited to isotropic aluminum plates.

The present work examined guided-wave monitoring of composite panels subjected to temperature fluctuations of normal aircraft operations (-40 °C to +60 °C). The flexible MFC-type P1 patches (Wilkie et al. 2000, Sodano et al. 2004) are considered as wave transducers. A model is first proposed to predict pitch-catch wave signals in composite plates under changing temperature. The results of the model are then used to guide experiments on a CFRP skin-to-spar joint with simulated bond defects (poorly-cured adhesive and two sizes of disbonds). It is shown that a multivariate statistical Outlier Analysis, performed on the amplitude of the pitch-catch waves propagating through the joint, is able to detect the bond defects despite the temperature excursion once the statistical baseline distribution is partitioned in as few as two portions, namely below ambient temperature (-40 °C to +20 °C) and above ambient temperature (+20 °C to +60 °C).

Beyond just detection is the goal of quantification and classification. By studying the characteristics of the reflected and transmitted waves, quantitative information on the defects can be obtained. A hybrid formulation was used in this work wherein the finite element method is employed to model small regions near the defect whereas regions away from the defect are modeled using a suitable set of wave functions. Goetschel et al. (1982) developed a global-local finite element formulation for modeling axisymmetric scattering of a steady, compressive, incident elastic wave in a homogeneous, isotropic host medium with an axisymmetric inclusion. The hybrid method was also used in to model defects in a plate and a cylinder, respectively (Al-Nassar et al. 1991, Rattanawangcharoen et al. 1997). In the area of SHM of aircraft components, the method has been applied to model wave interaction with defected lap-shear joints (Chang and Mal 1995), as well as notches and rivet-hole cracks in plates (Mal and Chang 1999, 2000).

Many aircraft components are complex in either their geometry (e.g. multilayers, tapered thickness, etc.) or their material properties (e.g. anisotropic). In this case theoretical wave solutions for the global portion are either nonexistent or hard to determine. The Semi Analytical Finite Element (SAFE) method can help handle these cases because of its ability to extract modal solutions of complex structures in a computationally efficient manner (Hayashi et al. 2003, Bartoli et al. 2006). Sabra et al. (2008) demonstrated the application of the SAFE-aided hybrid formulation to the detection of holes in aluminum plates. The present work extends the global-local approach to model notches in aluminum plates and delamination-like defects in composite panels and suggests how this could apply to delaminations.

This previous active approach inherently relies upon characteristics of specific GUW modes and their properties, and the GUWs' interaction with the structure. When coupled with SAFE models, very specific features may be identified that can indicate specific flaws. However, structural geometries such as highly curved regions, bolted interfaces, etc., pose significant modeling and testing challenges for GUWs, resulting in difficulty in classifying size or type of damage due to the inherent simplicity of the actively imparted excitation signal, which is usually a modulated, narrow-band, short-wave pulse. Instead, some researchers have attempted to employ bulk insonification, where an ultrasonic source is excited, and the resultant long-time, or diffuse, wave field is examined to identify structural changes (Michaels and Michaels, 2005). This method was investigated as well to augment the standard guided wavc method for structures with complex boundary conditions or geometries that make tracking and analysis of a single propagating mode difficult or impossible. This approach relies on data-driven (typically, time series) models and change detection approaches rooted in statistical pattern recognition.

Given these varied approaches, one might envision a possible general taxonomy for damage detection strategies in the ultrasonic domain as shown in Figure 2. Global-Local, including SAFE, modeling (physics-based) is critical for the middle column, and data-based modeling is critical for the right-hand column.

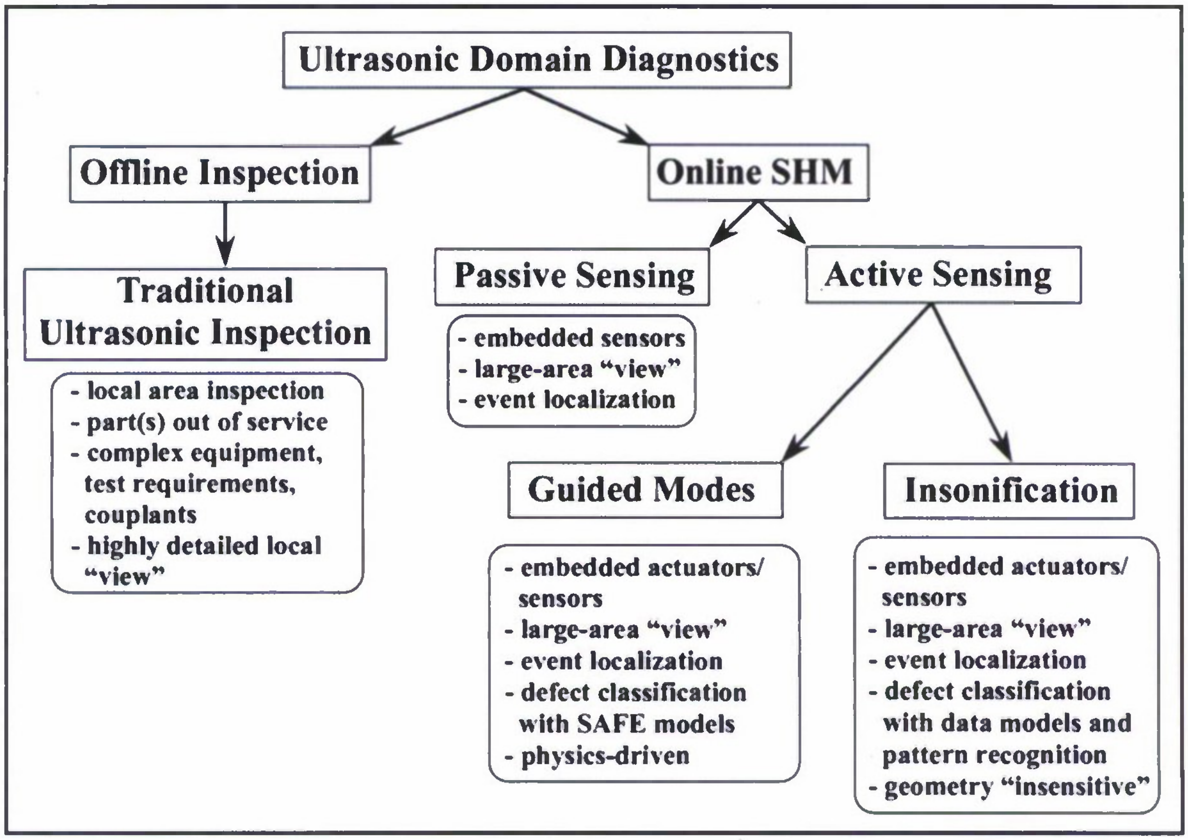

Figure 2. Ultrasonic domain diagnostic taxonomy.

The primary challenges facing GUW-based CBM data interrogation methods are twofold: (i) extracting, in an appropriately efficient time frame, features from the detected GUWs that are sensitive to the defects of interest, and (ii) ensuring that these features are reasonably insensitive to operational, testing, and environmental variability observed in platform service, or using appropriate statistical modeling to decouple (or at least minimize correlation of) the feature sensitivities to damage and to this variability. This project proposed three research areas (summarized in the Executive Summary Section above) that addressed these challenges. The following three sections will now describe the research findings addressing these challenges in greater detail, followed by a full listing of publications resulting from this project, and concluding with cited references.

2. HEALTH MONITORING OF COMPOSITE PANELS UNDER CHANGING TEMPERATURE

2.1 Pitch-Catch Guided Wave Model With Shear-Lag

The problem examined, Figure 3a, is that of an MFC actuator on a T700/5208 CFRP composite plate with a lay-up of $[0/\pm45/0]_S$, exciting ultrasonic guided waves which are detected by a similar piezoelectric patch sensor (pitch-catch). The problem is studied in 2-D, and assuming plane waves.

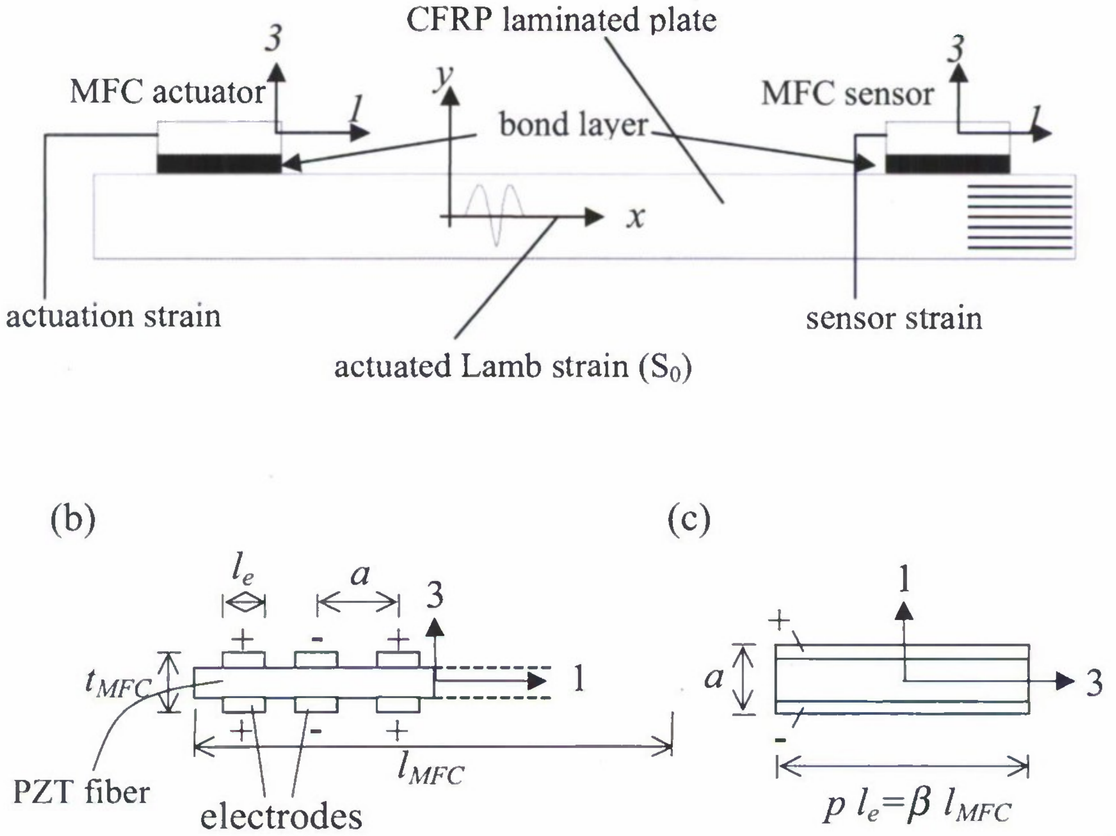

Figure 3. (a) Pitch-catch Lamb wave monitoring by MFC patches; (b) composite MFC type-P1 patch; (c) equivalent model for MFC type-P1 sensor patch.

In a previous work (Lanza di Scalea and Salamone 2008), a pitch-catch model was developed for PZT and MFC pitch-catch systems applied to isotropic plates. This formulation explicitly accounted for the effects of temperature on the transducer piezo-mechanical constants, the transducer/plate interaction (through shear-lag), and the plate dispersive properties. The model is here revised and applied to the case of the composite laminate at hand. This is done by considering an "equivalent" isotropic plate whose s_0 dispersion properties match those of the composite laminate (determined by a Semi-Analytical Finite Element – SAFE analysis) in the frequency range of interest. The focus is on the s_0 mode since this was previously determined to be preferentially excited by the MFC transducers with a setup similar to that of Figure 1 (Lanza di Scalea et al. 2007).

2.1.1. Shear Stress at Actuator-Plate Interface

Shown in Figure 3b, the MFC-type P1 transducer is composed by PZT fibers that are unidirectionally aligned, embedded into an epoxy matrix, and sandwiched between two sets of inter-digitated electrodes. The strain generated by an MFC actuator poled along the in-plane (fiber) direction 1 (electric field components $E_2 = E_3 = 0$) and excited by a voltage V_{appl} is:

$$\varepsilon_{act} = \varepsilon_{11} = -d_{11}\frac{V_{appl}}{a} \tag{1}$$

where a is the MFC inter-electrode spacing and d_{11} is the relevant piezoelectric coefficient.

Assuming the surface-bonded actuator system of Figure 4a, the non-dimensional shear-lag parameter, Γ, from Crawley and de Luis (1987) is given by:

$$\Gamma^2 = \frac{G_{bond}}{Y_{act}^E}\frac{l_{act}^2}{t_{bond}t_{act}}\frac{\Psi+\alpha}{\Psi} \tag{2}$$

where G_{bond}, t_{bond} are the shear modulus and thickness of the adhesive layer; Y_{act}^E, l_{act}, t_{act} are the in-plane Young's modulus (fiber direction), length and thickness of the MFC actuator; the factor α is 1 or 3 for extensional or bending actuation, respectively; and Ψ is the plate-actuator stiffness ratio given by:

$$\Psi = \frac{E_{plate}\, t_{plate}}{Y_{act}^{E}\, t_{act}} \tag{3}$$

It is well known that the shear-lag effect increases with increasing compliance and thickness of the bond layer. Perfect bonding (no shear-lag) is achieved for a thin and stiff bond layer where $\Gamma \to \infty$.

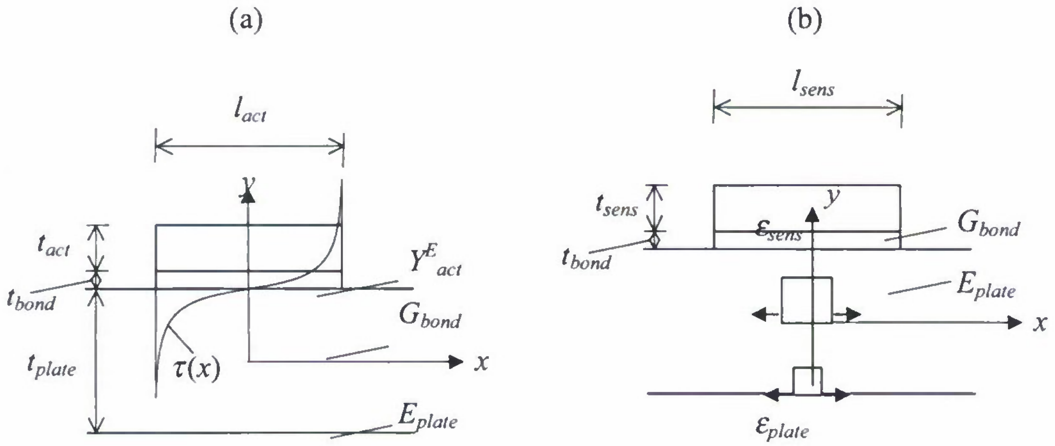

Figure 4. . (a) Shear-lag actuator model; (b) shear-lag sensor model.

The spatial distribution of the in-plane shear stress applied by the actuator into the plate proposed by Crawley and de Luis (1987), $\tau(x)$, can be transformed into the spatial frequency (wavenumber) domain, $\tilde{\tau}(k)$, once the finite length of the actuator, l_{act}, is taken into account (Lanza di Scalea and Salamone 2008). The spatial Fourier transform of the actuated shear stress under shear-lag is:

$$\tilde{\tau}(k) = -2\, i \frac{G_{bond}\, l_{act}^{2}}{t_{bond}\left(4\Gamma^{2} + k^{2} l_{act}^{2}\right)} \varepsilon_{act} \left[k\, l_{act} \frac{\tanh(\Gamma)}{\Gamma} \cos\left(\frac{k\, l_{act}}{2}\right) - 2\sin\left(\frac{k\, l_{act}}{2}\right) \right] \tag{4}$$

where i is the imaginary unit and k the wavenumber. For the perfect-bond case ($\Gamma \to \infty$), Equation (4) retrieves the "wavelength tuning" conditions identified by Giurgiutiu (2005), i.e. zero actuation when $k\, l_{act}/2 = n\pi$ for $n = 0,1,2..$ (i.e. actuator length equals an integer multiple of the wavelength λ), and local maximum actuation for $k\, l_{act}/2 = \pi(2n-1)/2$ (i.e. actuator length equals an odd multiple of the half wavelength $\lambda/2$). The zero and maximum actuation points are only slightly shifted from these ideal conditions for practical shear-lag cases.

The magnitude of the Fourier transform $\left|\tilde{\tau}(k)\right|$ from Equation (4) is plotted versus the non-dimensional wavenumber in Figure 5. This figure considers a baseline MFC type P1 actuator (Y^E_{act}=30 GPa, $t_{act} = 0.2$ mm, $d_{11} = 404 \times 10^{-12}$ m/V), excited by a unity voltage ($V_{appl} = 1$ V), bonded by an adhesive layer ($t_{bond} = 0.01$ mm) on an equivalent isotropic plate ($E_{plate} = 30$ GPa, $t_{plate} = 1.067$ mm), under extensional actuation for s_0 (α= 1). In the figure the "wavelength tuning" behavior is evident.

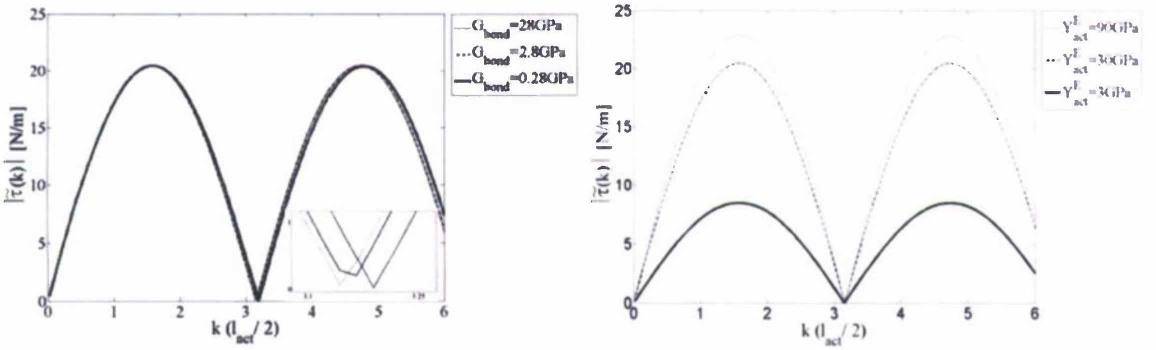

Figure 5. Magnitude of spatial Fourier Transform of in-plane shear stress at the actuator/plate interface under shear-lag conditions: (a) changing bond layer stiffness, (b) changing actuator stiffness.

Figure 5a examines the effect of changing the bond layer stiffness. $\left|\tilde{\tau}(k)\right|$ is plotted for a nominal bond stiffness of G_{bond}= 2.8 GPa (corresponding to a shear lag parameter $\Gamma = 209.8$), and for two extreme cases of a very stiff adhesive (G_{bond}= 28 GPa or $\Gamma = 658.7$) and a very compliant adhesive (G_{bond}= 0.28 GPa or $\Gamma = 66.3$). The plots indicate that the predominant effect of a changing adhesive stiffness is a slight shift in zeroes and maxima of the $\left|\tilde{\tau}(k)\right|$ curve (see inset in Figure 5a), i.e. the wavelength tuning points, with virtually no effect on the magnitude of $\left|\tilde{\tau}(k)\right|$, i.e. the net force transferred to the plate.

Figure 5b examines the effect of changing the actuator stiffness. $\left|\tilde{\tau}(k)\right|$ is plotted for a constant $G_{bond} = 2.8\ \mathrm{GPa}$, and with changing actuator stiffness from a nominal $Y^E_{act} = 30\,\mathrm{GPa}$ ($E_{plate}/Y^E_{act} = 1$), to a very stiff actuator ($Y^E_{act} = 90\,\mathrm{GPa}$ or $E_{plate}/Y^E_{act} = 0.33$) and a very compliant actuator ($Y^E_{act} = 3\,\mathrm{GPa}$ or $E_{plate}/Y^E_{act} = 10$). It is shown that the actuator stiffness influences highly the magnitude of the stress transfer, with $\left|\tilde{\tau}(k)\right|$ substantially decreasing with lower actuator stiffness.

Under temperature variations both G_{bond} and Y^E_{act} will vary. Shown later, the temperature range of interest in this study (-40 °C to +60 °C) will have a substantial influence on the actuation magnitude, with little change in the wavelength tuning points.

2.1.2. Actuated Lamb Strain in Plate

The Lamb wave strain field generated by the actuator is found from the mode expansion formulation by Giurgiutiu (2005) coupled with the shear stress Fourier Transform of Equation (4). The actuated Lamb strain at the surface of the plate in the wave propagation direction, *x*, is:

$$\varepsilon_x(x,t)\Big|_{y=\frac{t_{plate}}{2}} = i\,\varepsilon_x\,e^{i(kx-\omega t)} \tag{5}$$

where the actuated wave amplitude is:

$$\varepsilon_x = \frac{\tau_1}{2G_{plate}}\left[\underbrace{\sum_{k^S}\tau_2(k^S)\frac{N_S(k^S)}{\partial D_S(k^S)/\partial k}}_{\text{Symm. modes}} + \underbrace{\sum_{k^A}\tau_2(k^A)\frac{N_A(k^A)}{\partial D_A(k^A)/\partial k}}_{\text{Antisymm. modes}}\right] \tag{6}$$

where $k^S_i(\omega)$ are the eigenvalues (wavenumbers) for the Lamb symmetric modes (solutions of $D_S = 0$), $k^A_i(\omega)$ are the eigenvalues for the Lamb anti-symmetric modes (solutions of $D_A = 0$), and the remaining terms are well-known expressions of Rayleigh-Lamb theory (e.g. Rose 1999).

In Equation (6) the shear stress expression is decomposed into the following constant term, τ_1, and k-dependent term, $\tau_2(k)$:

$$\begin{cases} \tau_1 = \dfrac{-2\, G_{bond}\, l_{act}^2\, \varepsilon_{act}}{t_{bond}} \\[2ex] \tau_2(k) = \dfrac{k\, l_{act} \dfrac{\tanh(\Gamma)}{\Gamma} \cos\left(\dfrac{k\, l_{act}}{2}\right) - 2\sin\left(\dfrac{k\, l_{act}}{2}\right)}{4\,\Gamma^2 + k^2\, l_{act}^2} \end{cases} \tag{7}$$

T700/5208 CFRP Composite Lamina						
E_1=134 GPa	E_2=9 GPa	G_{12}=4.2 GPa	ν_{12}=0.26	G_{23}=3.2 GPa	ρ=1530 Kg/m^3	t = 0.13 mm
Equivalent Isotropic Plate						
E_{plate}=23.7 GPa				G_{plate}=13 GPa		

Table 1. Ambient-temperature properties of CFRP lamina and equivalent isotropic plate.

Equation (6) requires the elastic properties of the substrate plate, including its $k(\omega)$ dispersion curves. The plate of interest in this study is a $[0/\pm45/0]_S$, T700/5208 CFRP composite laminate, with wave propagation direction in the 90 degree direction of the top ply (see Figure 6). The laminate can be studied by considering an "equivalent" homogeneous isotropic plate whose s_0 dispersion properties match those of the composite plate in the frequency range of interest. Similar equivalent isotropic models of composite plates were considered in the past for guided wave studies (Sohn et al. 2003, Kim et al. 2007). Phase velocity dispersion curves, shown in Figure 4, were first obtained for the subject composite plate using a Semi-Analytical Finite Element approach (Bartoli et al. 2006). The elastic constants assumed in the model for T700/5208 are reported in Table 1. The same curves were also obtained for the "equivalent" isotropic plate using conventional Rayleigh-Lamb characteristic equations. The two independent engineering constants E_{plate} and ν_{plate} assumed for the "equivalent" plate were iteratively changed until a satisfactory match was obtained for the s_0 mode of interest (see Figure 6). Density and thickness of the "equivalent" isotropic and the composite plates were kept identical. The figure shows that a good s_0 match does not translate into a match of the antisymmetric a_0 mode, and increasingly so with increasing frequency. This is because the phase velocity of the antisymmetric mode, in the non-dispersive branch, depends upon the out-of-plane shear modulus that is typically small in composite plates because mainly influenced by the matrix properties. Hence, an equivalent isotropic model cannot, in general, capture the dispersion properties of both symmetric and antisymmetric modes of an anisotropic composite laminate.

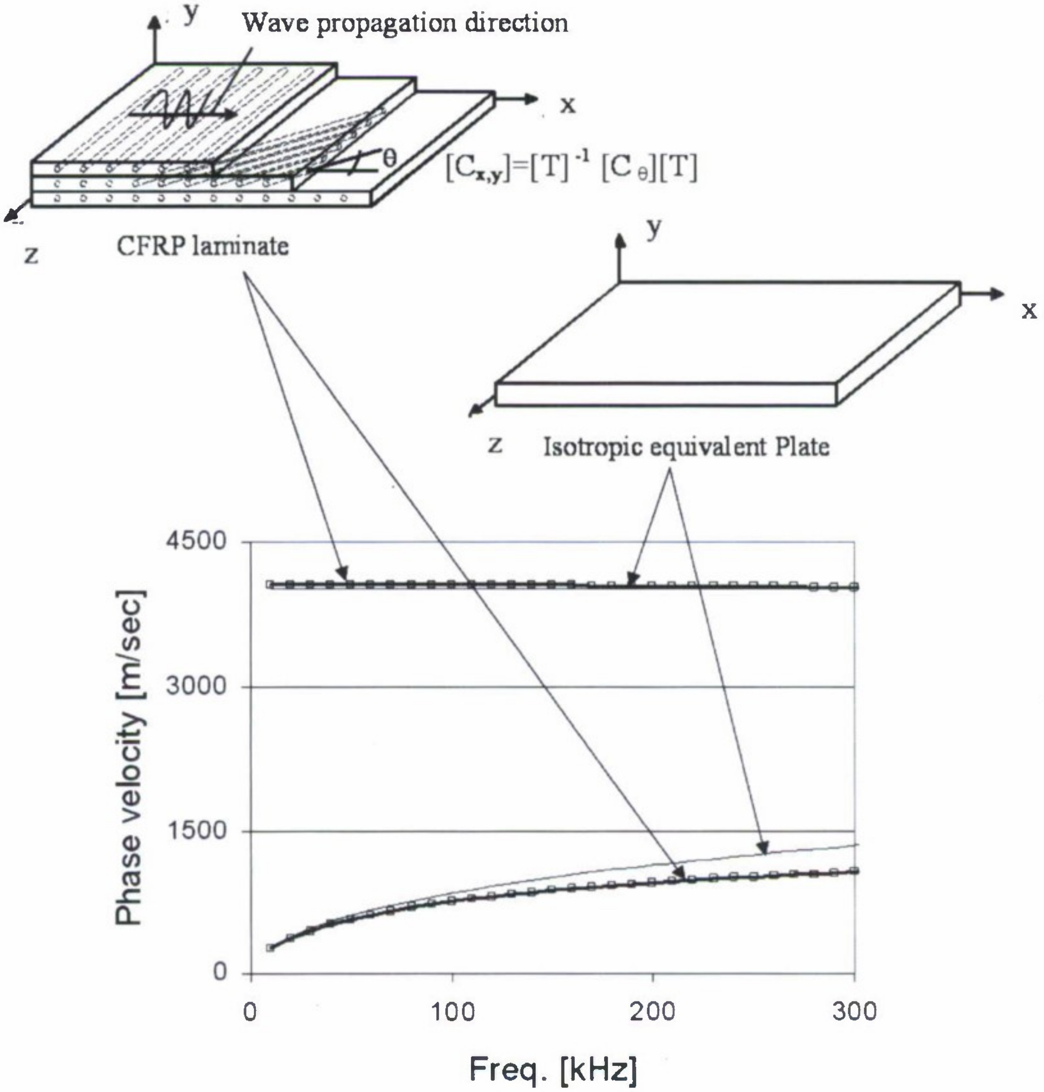

Figure 6. Dispersion curves of $[0/\pm45/0]_S$ T700/5208 CFRP composite laminate along propagation direction *x* (SAFE solution) and equivalent isotropic plate (Rayleigh-Lamb solution).

2.1.3. Sensor Response

The shear-lag model for the plate - MFC sensor system is shown in Figure 4b. The strain transferred from the plate, ε_{plate}, into the sensor, ε_{sens}, can be found by using the study by Crawley and de Luis (1987) for a piezoelectric *actuator*-plate case, and modifying the boundary conditions to reflect the plate-*sensor* case. The following boundary conditions are applied at the ends of the sensor:

$$\varepsilon_{plate} = \varepsilon_x \text{ (Lamb strain)} \qquad \text{and} \qquad \varepsilon_{sens} = 0 \qquad \text{at } x = \pm\, l_{sens}/2 \tag{8}$$

These lead to the following solution for the sensor strain, ε_{sens}, as a function of the incoming Lamb strain in the plate, ε_x, and the shear-lag parameters Ψ, Γ and α.

$$\varepsilon_{sens} = \varepsilon_x \left(\frac{\Psi}{\alpha + \Psi} \right) \left[1 - \frac{\cosh\left(\Gamma \frac{2x}{l_{sens}} \right)}{\cosh \Gamma} \right] \tag{9}$$

The voltage response of the P1-type MFC sensor can be derived by considering the equivalent circuit of Figure 1c. Here the MFC is reduced to an equivalent PZT with thickness equal to the MFC electrode spacing, *a*, and length equal to the MFC net electrode length, ($p\, l_e$), where *p* is the number of electrodes on a single face of the MFC. The net electrode length is thus a fraction of the full MFC length, $p\, l_e = \beta\, l_{MFC}$, (here $l_{MFC} = l_{sens}$) where β is a reduction factor depending on the design of the MFC. The equivalent model also requires a rotation of the sensor axes (*1*, *3*) as shown in the figure. This model yields the following voltage response of the P1-type MFC sensor as a function of the in-plane strain in the sensor, ε_{sens}:

$$V_{MFC} = S_{MFC} \int_{-\frac{l_{MFC}}{2}}^{\frac{l_{MFC}}{2}} \varepsilon_{sens}\, dx \tag{10}$$

with sensitivity term:

$$S_{MFC} = \frac{a}{\beta\, l_{MFC}} \frac{\left(d_{11}\, Y_1^E + d_{12} \nu_{12} Y_2^E\right)}{\left[e_{11}(1-\nu_{12}\nu_{21}) - (d_{11}^2 Y_1^E + 2 d_{11} d_{12} \nu_{12} Y_2^E + d_{12}^2 Y_2^E)\right]} \qquad (11)$$

where (Y_i^E , ν_{ij}) are the in-plane elastic constants of the MFC sensor and (d_{11} , d_{12} , e_{11}) are the nonzero piezoelectric coefficients and dielectric permittivity term of the MFC sensor.

2.1.4. Complete Pitch-Catch Actuator-Sensor Response

The pitch-catch solution for a pair of MFC transducer patches under shear-lag conditions, Figure 3, can now be found by substituting the strain expression of Equation (9) into the sensor response of Equation (10). After algebra, the voltage generated by an MFC actuator-sensor pair is:

$$V_{MFC \rightarrow MFC} = i\, S_{MFC}\, \varepsilon_x \left(\frac{\Psi}{\alpha + \Psi}\right)\left(R_{perf\_bond} - R_{shear\_lag}\right) e^{-i\omega t} \qquad (12)$$

where it was possible to isolate the two terms responsible for the perfect-bond response, R_{perf_bond}, and for the shear-lag response, R_{shear_lag}, respectively given by:

$$R_{perf\_bond} = \frac{2 \sin\left(k\, l_{sens}/2\right)}{k} \qquad (13)$$

$$R_{shear-lag} = \frac{4\, l_{sens}\, \Gamma}{(k^2 l_{sens}^2 + 4\,\Gamma^2)}\left[\tanh(\Gamma)\cos\left(k\, l_{sens}/2\right) + \left(k\, l_{sens}/2\Gamma\right)\sin\left(k\, l_{sens}/2\right)\right] \qquad (14)$$

From Equation (12) the pitch-catch response emerges as a combination of the perfect bond response and the shear-lag response, whose effect is to decrease the overall signal amplitude (notice minus sign for R_{shear_lag}).

2.2. Temperature Effects

The expression in Equation (12) allows isolating the temperature-dependence of the properties of actuator, sensor, transducer/plate bond layers, and plate substrate. These properties are examined in the following sections in the range of normal aircraft operations, -40 °C to +60 °C. Unless otherwise specified, a linear dependence of each property on temperature is assumed:

$$P(T) = P(T_0) + \frac{\partial P(T)}{\partial T}\Delta T \qquad (15)$$

where P represents one of the properties, T is the generic temperature, T_0 is the ambient temperature (20 °C), and $\partial P/\partial T$ is the sensitivity to temperature. The values considered are summarized in Table 2 and discussed in detail below.

MFC transducer properties			
$E_m(T_0)$=4.7 GPa $\partial E_m/\partial T$=-0.028 GPa/°C	$\nu_m(T_0)$=0.45 $\partial \nu_m/\partial T$=0.009/ °C	$E_f(T_0)$=70 GPa $\partial E_f/\partial T$=0.16GPa/°C	$\nu_f(T_0)$=0.31 $\partial \nu_f/\partial T$=–0.013 /°C
$d_{11}(T_0)$=404×10^{-12} m/Volt $\partial d_{11}/\partial T$=1 m/(Volt °C)	$d_{12}(T_0)$=-167×10^{-12} m/Volt $\partial d_{12}/\partial T$=-0.5 m/(Volt °C)	$e_{11}(T_0)$=15×10^{-9} Farad/m $\partial e_{11}/\partial T$=0.043×$10^{-9}$ Farad/(m °C) – below 20 °C $\partial e_{11}/\partial T$=0.14×$10^{-9}$ Farad/(m °C) – above 20 °C	

Transducer/plate bond layer properties	
$G_{bond}(T_0)$=3.4 GPa	$\partial G_{bond}/\partial T$=-0.013 GPa/°C

"Equivalent" substrate plate properties	
$E_{plate}(T_0)$=23.7 GPa	$G_{plate}(T_0)$=13 GPa

$\partial E_{plate}/\partial T$ =-0.014 GPa/°C	$\partial G_{plate}/\partial T$ =-0.008 GPa/°C

Table 2. Temperature-dependence of the properties of MFC transducers, transducer/plate bond layer, and substrate plate.

2.2.1. Temperature Effects on Actuator and Sensor Properties

The temperature-dependent properties of the MFC actuator and sensor patches influencing the response in Equation (12) are: Young's moduli Y_1^E, Y_2^E from Equations (2), (3), and (11); Poisson's ratios ν_{12}, ν_{21} from Equation (11); piezoelectric coefficients d_{11}, d_{12} from Equations (1) and (11); dielectric permittivity terms e_{11} from Equation (11); length and thickness dimensions. All of these terms are considered in the following.

Conventional rules of mixture were used to calculate the effective Young's moduli and Poisson's ratios of the MFC patches from the constituent properties of fibers (E_f, ν_f) and matrix (E_m, ν_m) through the fiber volume fraction, V_f (Jones 1975):

$$Y_1^E = E_f V_f + E_m(1-V_f)\,,\; Y_2^E = \frac{E_f E_m}{(1-V_f)\,E_f + V_f E_m}\,,\; \nu_{12} = V_f\,\nu_f + (1-V_f)\,\nu_m\,,\; \nu_{21} = \nu_{12}\frac{Y_2^E}{Y_1^E} \tag{16}$$

The temperature dependence of Young's modulus and Poisson's ratios for PZT-5A fibers were modeled according to Equation (15) using $E_f(T_0)$ = 70 GPa, $\nu_f(T_0)$ = 0.31, and temperature sensitivities of $\partial E_f / \partial T$ = 0.16 GPa/°C and $\partial \nu_f / \partial T$ =-0.013/°C (Sherrit et al. 1999). The matrix properties were obtained experimentally from longitudinal and shear ultrasonic time-of-flight measurements conducted on epoxy coupons in an environmental chamber with temperature control. The measurements were averaged over two separate coupons and three temperature cycles. The following matrix properties were obtained: $E_m(T_0)$ = 4.7 GPa/°C, $\nu_m(T_0)$ = 0.45 with sensitivities of $\partial E_m / \partial T$ =-0.028 GPa/°C and $\partial \nu_m / \partial T$ = 0.009/°C. A constant volume fraction $V_f = 0.4$ was assumed. The temperature sensitivity of the MFC properties Y_1^E, Y_2^E, ν_{12}, and ν_{21} was then calculated from Equation (16).

Regarding the piezoelectric coefficients, the following values were used: $d_{11}(T_0) =$ 404×10^{-12} m/Volt, $d_{12}(T_0) = -167\times10^{-12}$ m/Volt, as obtained from manufacturer's data; sensitivities $\partial d_{11} / \partial T = 1$ m/(Volt °C) from Hooker (1998) and $\partial d_{12} / \partial T = -0.5$ m/(Volt °C) from Lee and Saravanos (1998) (notice that d_{12} of the MFC patch is equivalent to d_{31} of the monolithic PZT reported in this reference).

The dielectric permittivity term was considered bilinear to best fit the data by Lee and Saravanos (1998) (e_{11} of the MFC patch is equivalent to e_{33} of the monolithic PZT in this reference). The ambient value was $e_{11}(T_0) = 15\times10^{-9}$ Farad/m, with sensitivities $\partial e_{11} / \partial T$ $= 0.043\times10^{-9}$ Farad/(m °C) below ambient temperature, and $\partial e_{11} / \partial T = 0.14\times10^{-9}$ Farad/(m °C) above ambient temperature.

Patch length and thickness changes were modeled assuming a coefficient of thermal expansion of 5×10^{-6} m/(m °C) along the fibers and 15×10^{-6} m/(m °C) across the fibers (Williams et al. 2004).

2.2.2. Temperature Effects on Transducer/Plate Bond Layer Properties

Shear modulus G_{bond} and thickness t_{bond}, both present in Equations (2) and (7), influence the voltage expression in Equation (12). Ambient-cure epoxy adhesive (Loctite from Henkel Corporation, Rocky Hill, CT) was used in this study. The temperature dependence of G_{bond} was measured by ultrasonic shear-wave velocity measurements on epoxy coupons tested in the autoclave between -40 °C and +60 °C. By averaging the measurements over two separate coupons and three temperature cycles, the following regression line was obtained with a 0.96 regression coefficient:

$$G_{bond}(T)[GPa] = 3.2 - 0.013T[°C] \qquad (17)$$

Changes in thickness of the bond due to thermal expansion were considered negligible and ignored.

2.2.3. Temperature Effects on Substrate Plate

Properties of the substrate plate affecting the pitch-catch response include Young's modulus E_{plate}, thickness t_{plate}, and shear modulus G_{plate} from Equations (3) and (6). In addition, these properties affect the dispersion relations $k(\omega)$.

In the subject CFRP laminate, the temperature range of -40 °C to +60 °C affects primarily the properties of the polymeric matrix. The following temperature degradation factor proposed by Chamis (1984) for the stiffness of resin matrices is used:

$$F_m = \left(\frac{T_{g0} - T}{T_{g0} - T_R} \right)^{1/2} \tag{18}$$

where T_{g0} is the glass transition temperature at the reference temperature T_R. The elastic properties of the composite plies were then calculated as (Chamis, 1984):

$$\begin{gathered} E_1 = E_f V_f + F_m E_m V_m \,,\; E_2 = \frac{F_m E_m}{1 - \sqrt{V_f}\left[1 - \left(F_m E_m / E_f\right)\right]}\,, \\ G_{12} = \frac{F_m G_m}{1 - \sqrt{V_f}\left[1 - \left(F_m G_m / G_f\right)\right]}\,,\; \nu_{12} = V_m \nu_m + V_f \nu_f \end{gathered} \tag{19}$$

These temperature-dependent values were inserted into the SAFE model to predict the s_0 dispersion curves for the subject $[0/\pm45/0]_S$ laminate. Finally, the properties E_{plate} and G_{plate} of the "equivalent" isotropic plate were found by matching the s_0 dispersion curves at 10deg temperature steps from -40 °C to +60 °C. This procedure led to the following properties of the "equivalent" plate: $E_{plate}(T_0)$=23.7 GPa, $G_{plate}(T_0)$=13 GPa, and temperature sensitivities of $\partial E_{plate} / \partial T$= -0.014 GPa/°C and $\partial G_{plate} / \partial T$=-0.008 GPa/°C. The density of the plate was set to ρ_{plate}=1530 kg/m^3. The ambient-temperature elastic properties for the composite and the equivalent isotropic plate are summarized in Table 1. Figure 7 shows the dispersion curves $k(\omega)$

computed by SAFE for s_0 and a_0 in the 1.067 mm-thick, $[0/\pm45/0]_S$ T700/5208 CFRP laminate at the temperatures of -40 °C, +20 °C, and +60 °C, and for waves propagating at 90 deg from the top ply. As expected, a temperature increase causes a decrease in phase velocity ω/k for both modes. It can also be seen that, for the temperature range of interest, the shifts in $k(\omega)$ values are quite small. Hence little change should be expected on the wavelength tuning points of the pitch-catch response spectrum.

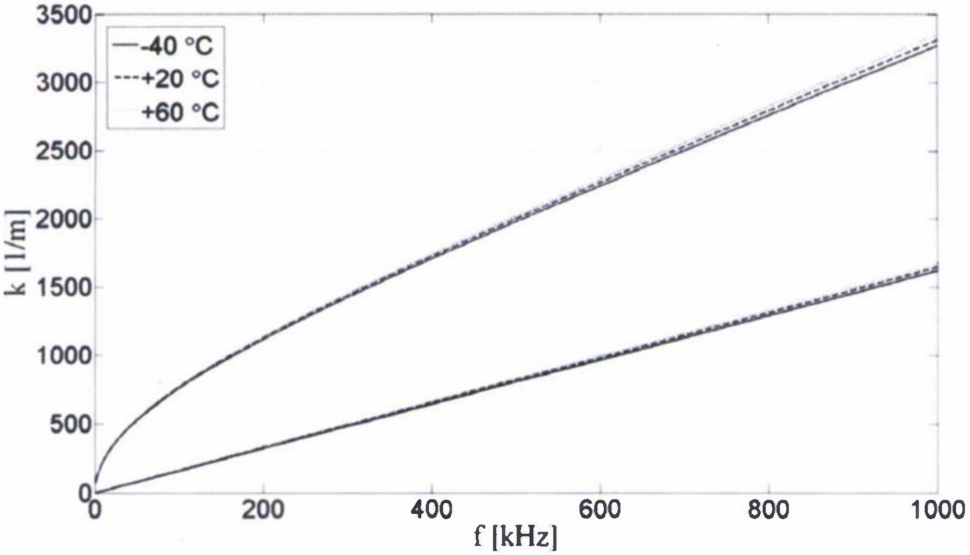

Figure 7. Dispersion curves of $[0/\pm45/0]_S$ T700/5208 CFRP composite laminate at the temperatures of -40°C, +20°C and +60°C.

2.3. Experiments

The model of Equation (12) was compared to pitch-catch measurements taken on the 1.067 mm-thick, $[0/\pm45/0]_S$ CFRP laminate (Figure 8a). The MFC patches were type P1 rectangular transducers (Smart Materials Corporation, Saratoga, FL) with an active length of 28 mm, other properties listed in Table 3, and installed at a distance of 75 mm from one another. The transducers were bonded to the plate using the ambient-cure Loctite epoxy adhesive. The measurements were taken in an environmental chamber (Figure 6b) between -40 °C and +60 °C at 10 °C intervals. Thermocouples were attached to the plates to verify that thermal equilibrium was achieved at each temperature step. A 3.5-cycle, Hanning-modulated toneburst was used as the actuating signal. The excitation was swept between 100 kHz and 300 kHz. The Root-Mean

Square of the measured s_0 mode was computed at each excitation frequency to quantify signal strength.

<table>
<tr><td colspan="5">Composite MFC–P1 patch</td></tr>
<tr><td>Y_1^E =30 GPa</td><td>Y_2^E =7.65 GPa</td><td>ν_{12}=0.31</td><td>$d_{11} = 404\times10^{-12}$ m/V</td><td>$d_{12} = -168\times10^{-12}$ m/V</td></tr>
<tr><td>e_{11}=15×10^{-9} Farad/m</td><td>β= 0.5</td><td>a = 0.1 mm</td><td>l_{act}=28 mm</td><td>t_{act} = 0.2 mm</td></tr>
<tr><td colspan="5">Transducer-plate adhesive layer</td></tr>
<tr><td colspan="2">G_{bond}= 2.8 GPa</td><td colspan="3">t_{bond}= 0.01 mm</td></tr>
</table>

Table 3. Ambient-temperature properties of composite MFC patch and of patch-plate adhesive layer.

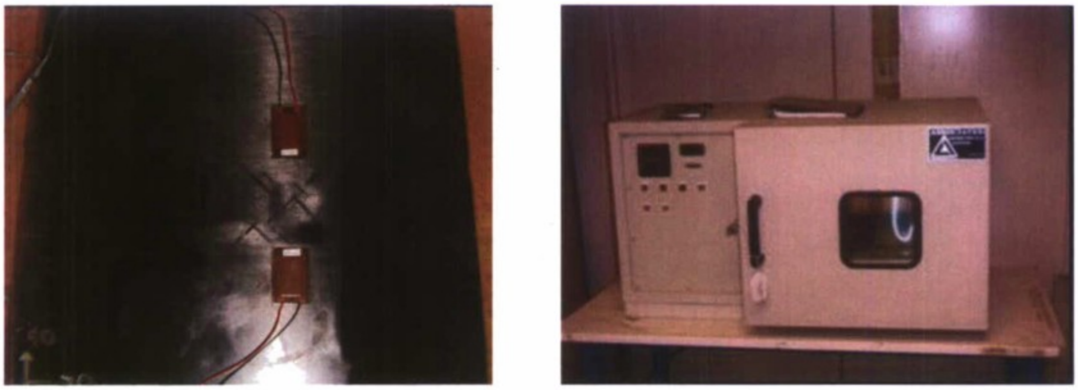

Figure 8. Experimental tests: (a) CFRP laminate with MFC actuator-sensor pair; (b) environmental chamber with temperature control.

Experimental and theoretical results are plotted in Figure 9. The curves are plotted separately for the above-ambient temperatures ($+20\,^{\circ}\mathrm{C} \le T \le +60\,^{\circ}\mathrm{C}$), and the below-ambient temperatures ($-40\,^{\circ}\mathrm{C} \le T \le +20\,^{\circ}\mathrm{C}$). The plots are normalized to the relative maxima; since the model neglected wave damping in the plate, measured and predicted absolute amplitudes cannot be compared. The general trend is consistent between theory and experiment. The wavelength tuning points match well. The mismatch in response magnitude could be caused by the damping effects in the plate and the plane wave assumption of the model. The results show that the main role of temperature is a change in the pitch-catch response amplitude. The changes in the 220 kHz response peak height, relative to the ambient temperature value, are on the order of 30% at +60 °C and on the order of 40% at -40 °C.

In addition, both theory and experiment show the response amplitude following two opposite trends above and below the ambient temperature: decreasing response with increasing temperature between $+20\,^{\circ}\mathrm{C} \le T \le +60\,^{\circ}\mathrm{C}$, and increasing response with increasing temperature between $-40\,^{\circ}\mathrm{C} \le T \le +20\,^{\circ}\mathrm{C}$. The reason for the opposite trends resides on the competing roles of the piezoelectric coefficients and the dielectric permittivity terms, as noted in the earlier work on isotropic plates by Lanza di Scalea and Salamone (2008).

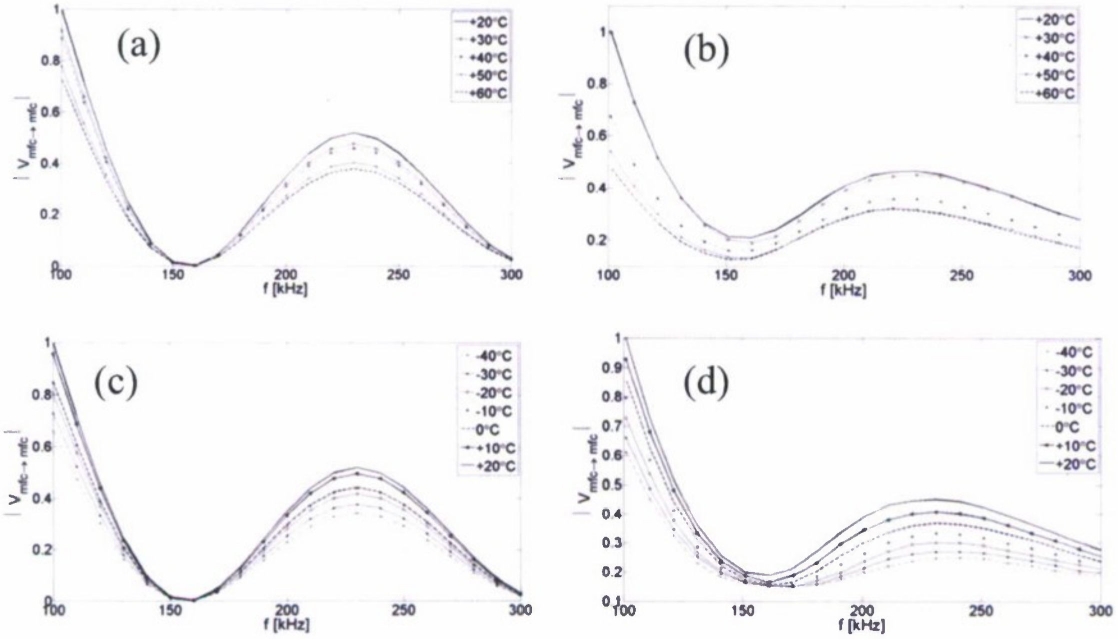

Figure 9. MFC pitch-catch response to s_0 Lamb mode in a $[0/\pm45/0]_S$ T700/5208 CFRP composite laminate under changing temperature in the ranges (a)-(b) above ambient (+20°C to +60°C), and (c)-(d) below ambient (-40°C to +20°C). Comparison is between (a)-(c) model and (b)-(d) experiment.

2.4. Detection Of Bond Condition In CFRP Skin-To-Spar Joint Under Changing Temperature

This section discusses the detection of adhesive bond defects in a specimen simulating the CFRP skin-to-spar joint of a UAV. The test joint was fabricated by bonding a $[0/\pm 45/0]_S$ T700/5208 CFRP laminate (dimensions 330 mm × 330 mm × 1.067 mm) on a woven T800/924 CFRP square tube (outer dimensions 50.8 mm × 50.8 mm, wall thickness 5.23 mm). A two-part Hysol 9394 epoxy adhesive was used as the bonding agent. Bonding was done such that the 0-deg fiber direction of the laminate ran along the lengthwise direction of the spar. The test joint, showing the MFC actuator/sensor pairs, is shown in Figure 10.

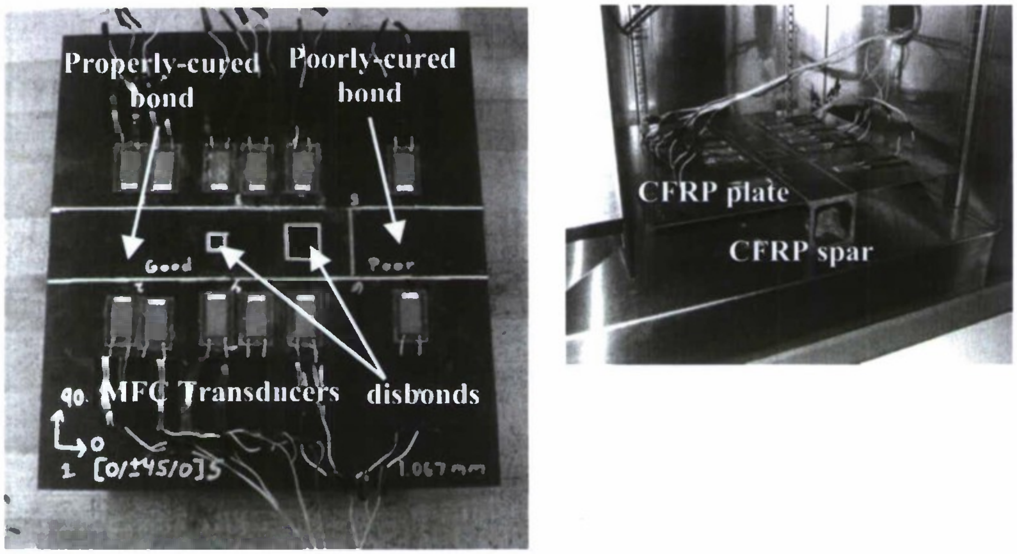

Figure 10. CFRP skin-to-spar joint specimen: (a) simulated bond defects and attached MFC transducers; (b) in environmental chamber for temperature tests.

Defects were engineered at the skin-spar bondline prior to joining. The majority of the bond was comprised of a properly-mixed epoxy, representing the well-bonded region. A poorly-cured region was created by improperly mixing the resin and hardener resulting in an approximate 50% degradation in longitudinal and shear stiffness compared to the properly-cured case. The degradation in stiffness was verified by ultrasonic pulse-echo measurements of longitudinal and shear waves conducted on epoxy samples. In addition, two sizes of Teflon release film inserts (12.7 mm × 12.7 mm and 25.4 mm × 25.4 mm) were added representing disbonded regions. The release film was expected to severly degrade the shear stiffness of the bond at those locations.

It was previously shown (Lanza di Scalea et al. 2007) that the strength of transmission of the s_0 mode through the joint is sensitive to the presence of these bond defects at room temperature. That study also showed that maximum sensitivity to bond state was achieved at "mode coupling" conditions (corresponding to a large transfer of ultrasonic energy through the thickness layers of the joints). Mode coupling occurred for s_0 at frequencies around 200 kHz for the subject joint. This frequency value also corresponded to an efficient wave transduction through wavelength tuning for the given MFC transducer patches on the $[0/\pm 45/0]_S$ CFRP plate according to the model presented earlier.

The present work adds the temperature variation to the study by Lanza di Scalea et al. (2007). It was discussed in the previous sections that temperature excursions can produce significant changes in guided-wave amplitude. Hence an effective on-board monitoring system must be able to discriminate changes due to bond defects from those due to temperature variations. This problem was here addressed as statistical pattern recognition by a multivariate Outlier Analysis.

2.4.1. Experimental Procedure

A total of six MFC pairs were installed to perform pitch-catch test through the bonded region of the test joint (Figure 10a). Three pairs monitored three different areas of the properly-cured bond for statistical significance. The other pairs monitored each of the three defected regions, namely the poorly-cured region and the two (large and small) disbonded regions. The joint was tested in the environmental chamber (Figure 10b) between -40 °C and +60 °C in 10 °C steps.

Ultrasonic signals were acquired by all six pairs at 205 kHz and time gated to isolate the predominant s_0 mode. Eight features related to the strength of transmission of the wave were computed from the measurements. These features were the Root-Mean-Square, the Variance, the Kurtosis, the Peak-to-Peak and the Peak of the time-domain signal; the Peak and the Area of the signal's Fourier transform spectrum; and the Area of the signal's Hilbert transform spectrum.

These features were assembled into an 8-dimensional Feature Vector for each measurement point.

A multivariate Outlier Analysis was conducted by computing the known Mahalanobis Squared Distance (MSD) as the discordancy metrics (Worden et al. 2002):

$$MSD = \left(\underline{\mathbf{x}} - \underline{\overline{\mathbf{x}}}\right)^{T} \underline{\mathbf{S}}^{-1} \left(\underline{\mathbf{x}} - \underline{\overline{\mathbf{x}}}\right) \tag{20}$$

where $\underline{\mathbf{x}}$ is the current Feature Vector, $\underline{\overline{\mathbf{x}}}$ is the mean vector of the baseline, $\underline{\mathbf{S}}$ is the covariance matrix of the baseline, and T represents a transposed matrix. If the MSD value exceeds a predetermined threshold, $\underline{\mathbf{x}}$ is an outlier i.e. statistically different from the baseline distribution. The threshold was here computed by a Monte Carlo simulation corresponding to a 99.9% confidence interval, i.e. 1 of every 1000 observations would result in a false-positive classification.

Regarding the baseline distribution, two different cases were considered. In one baseline, the set incorporated the measurements taken for the three MFC pairs probing the properly-cured bond over the entire temperature range (-40 °C to 60 °C). This is an "ideal" baseline, because it would simply require storing one set of measurements to perform statistical defect detection during the entire range of aircraft operations. However, this is also an "ambitious" baseline because it limits the ability of the pattern recognition to properly flag the defects. Hence a second baseline choice was also considered, whereas the full temperature range was partitioned into two ranges, -40 °C to 20 °C ("below ambient") and 20 °C to 60 °C ("above ambient"). In this second case the baseline distribution will have to be changed depending on whether the aircraft is flying or it is stored. This particular choice of baseline partition was consistent with the two different trends observed for the pitch-catch response in the composite plate

2.4.2. Results

Figure 11 shows the results of the univariate discordancy test based on only one signal feature. Root Mean Square is shown in Figure 11a and Peak-to-Peak is shown in Figure 11b. The baseline set incorporates measurements taken for the three properly-cured regions over the entire temperature range (-40 °C to 60 °C). The 99.9% threshold is shown as a horizontal straight line.

Each point corresponds to a measurement at a specific temperature and joint condition. It can be seen that the univariate analysis is not able to properly detect the bond defects as outliers, with the exception of a few measurements of the poorly-cured bond. Hence in this analysis temperature effects mask the effects of the defects.

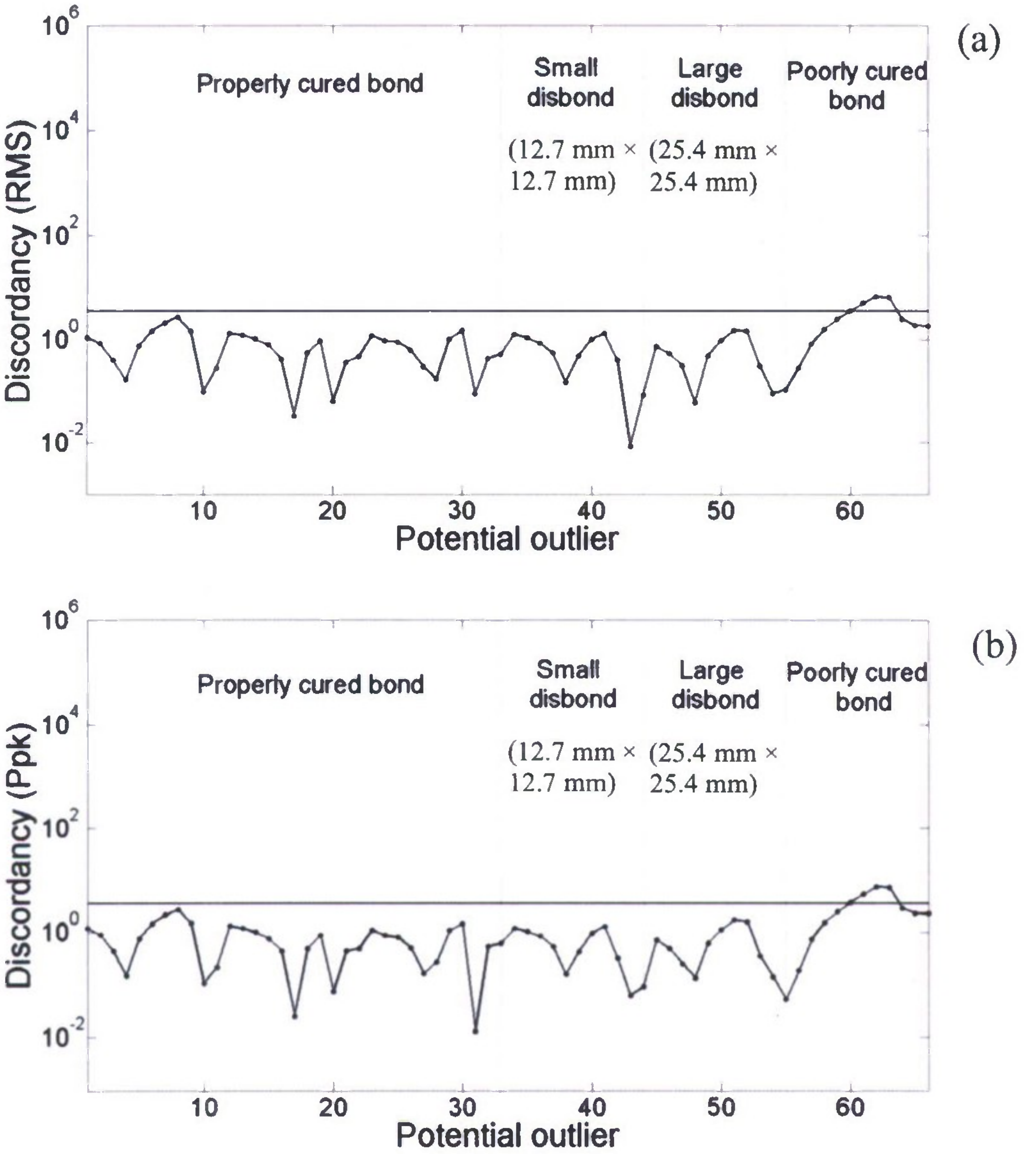

Figure 11. Univariate Outlier Analysis: results of discordancy test for (a) Root Mean Square signal feature; (b) Peak-to-Peak signal feature

The results of the multivariate analysis which uses the 8-dimensional Feature Vector are shown in Figure 12. The full baseline distribution (-40 ºC to 60 ºC) is again used in this figure. It is observed that the discriminatory power of the multivariate case is greatly improved relative to the univariate case, with many of the measurements taken at the defected regions being properly classified as outliers (MSD above threshold). However, some data points of the damage cases, particularly the "small" disbond case, are improperly flagged as inliers i.e. they represent false negatives.

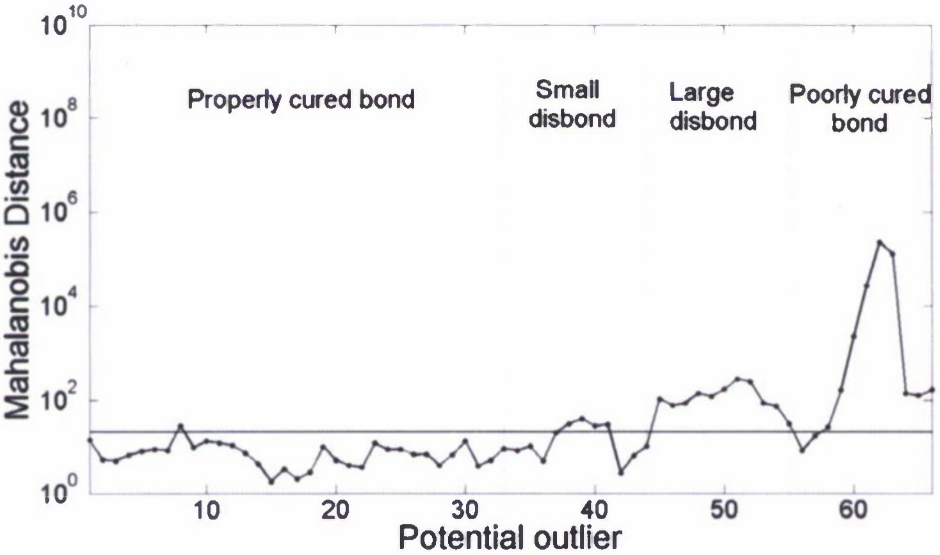

Figure 12. Multivariate Outlier Analysis: results of discordancy test with baseline distribution from full temperature range (-40 ºC to 60 ºC)

A further improved defect detection performance is obtained when the baseline is partitioned between the "below ambient" temperatures (Figure 13a) and "above ambient" temperatures (Figure 13b). In these analyses all measurements at defected regions are properly flagged as anomalies (no false negatives). Furthermore, all measurements at properly-cured regions are correctly flagged as inliers (no false positives).

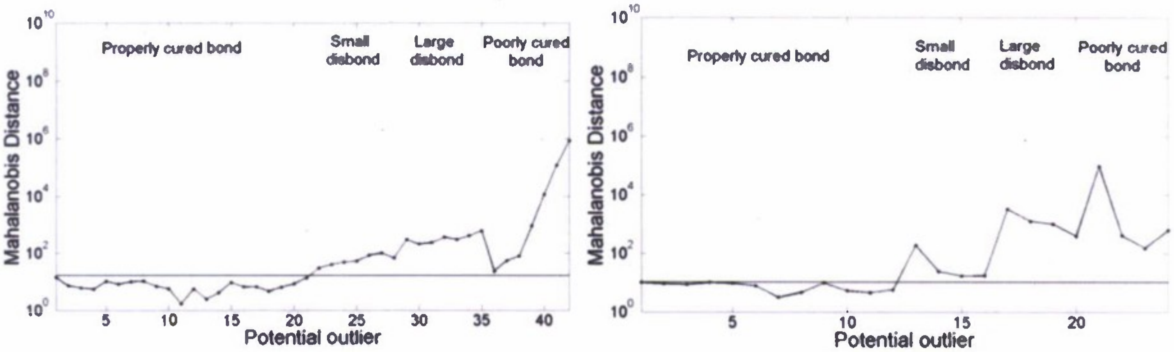

Figure 13. Multivariate Outlier Analysis: results of discordancy test with baseline distribution partitioned between (a) below ambient temperature (-40 °C to 20 °C), and (b) above ambient temperature (20 °C to 60 °C).

These results suggest that it is possible to detect the bond defects considered in this study within the temperature excursion of normal aircraft operations and in a statistically robust manner once (1) guided-wave measurements are taken at mode-frequency points that are particularly sensitive to the bond layer (s_0 at ~200 kHz for the subject joint), (2) several features, rather than any single feature, are extracted from the guided-wave measurements to perform a multivariate Outlier Analysis, and (3) a partition of the baseline distribution is performed to improve the discriminatory power of the statistical algorithm.

2.5 Discussion and Conclusions

The first part of the section discussed a model to predict the amplitude spectrum of pitch-catch guided-wave signals in composite plates probed by MFC piezocomposite transducers. The model accounts for the transducer piezo-mechanical properties, the transducer-plate interaction through shear-lag effects, and the substrate plate properties, all of which can be parametrized with temperature. Theoretical and experimental results obtained on a $[0/\pm45/0]_S$ CFRP laminate between -40 °C and 60 °C show substantial changes in the predominant s_0-mode amplitude (as high as 40% change from the ambient-temperature value). Little change, instead, is seen in the wavelength tuning points (maxima and zeros in the response). It was also observed that the signal amplitude follows two opposite trends below and above ambient temperature.

The second part of the section has applied these findings to the detection of bond defects in a CFRP skin-to-spar adhesive joint. The defects considered were a region of poorly-cured adhesive (50% degradation in stiffnesses) and two different sizes of disbonds. The study used an s_0 ultrasonic frequency (~200 kHz) which corresponded to a wavelength tuning peak for the MFC transducers, as well as to a mode-coupling condition for the multilayered joint structure. The strength of transmission of this frequency was used to monitor bond state in the (-40 °C to 60 °C) temperature range. It was found that a multivariate Outlier Analysis using 8 representative signal features can be successful in detecting the bond defects within the temperature excursions. Correct defect classification was obtained when the baseline distribution for the analysis was partitioned in two regions, below ambient temperature (-40 °C to 20 °C) and above ambient temperature (20 °C to 60 °C). In an on-board system, this suggests that the defects examined can be successfully detected by toggling the baseline between only two operational conditions: in-flight and storage.

There are several assumptions in the present work. The model assumes plane waves, thin transducers and neglects damping in the substrate plate. Also, the results on the bond defect detection only apply to the specific CFRP skin-to-spar joint tested. Different choices of wave frequency, Feature Vector dimension, and baseline distribution will likely be required for different applications.

3 GLOBAL-LOCAL MODELING/SIMULATION APPROACH FOR QUANTITATIVE DEFECT ASSESSMENT USING GUIDED WAVES

3.1. Theory

The geometry of the problem at hand is depicted in Figure 14 where the material inside the bounded surface has properties different from the outside due to the presence of local irregularities as a defect. In order to best illustrate the hybrid method, assume that a plane time-harmonic wave is incident on the FEM boundary in Figure 14. The region inside the boundary is meshed and analyzed using standard finite element analysis; the region outside the boundary is represented by the linear combination of a set of global wave functions, here calculated from the SAFE method. The continuity of displacements and tractions on the mesh boundary must be satisfied through proper choice of the amplitudes of the wave functions.

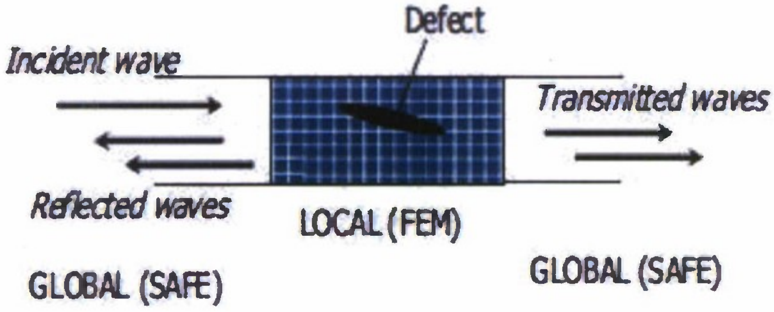

Figure 14. Geometry of a general wave scattering problem by Global-Local method.

3.1.1. Semi-Analytical Finite Element Method

The SAFE method is employed to calculate the guided wave modeshapes Φ and eigenvalues ξ for any infinitely-uniform cross-section. These modeshapes and eigenvalues are used to calculate the forces and displacements on the boundary separating the Global from the Local region. In the SAFE method, at each frequency ω a discrete number of guided modes is obtained. For the given frequency, each mode is characterized by a wavenumber, ξ, and by a displacement distribution over the cross-section. For a Cartesian reference system, the waveguide cross-section is set in the '*y-z*' plane while the *x*-axis is parallel to the waveguide length (see Figure 15).

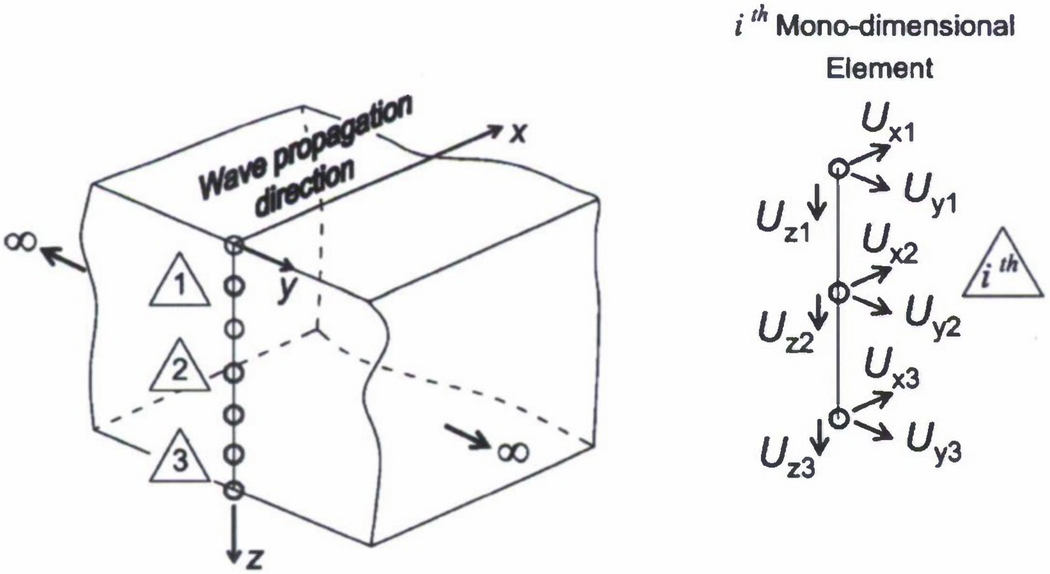

Figure 15. Plate waveguide cross-section in Cartesian coordinates for SAFE.

Subdividing the cross-section via finite elements, the approximated displacement at a point, u, is given as:

$$u = N\left(y,z\right)U^{e}e^{i\left(\xi x-\omega t\right)} \tag{21}$$

where $N(y,z)$ is the matrix of the shape functions, U^{e} is the nodal displacement vector for the e^{th} element, t is the time variable and i the imaginary unit. It can be noted that the displacement is described by the product of an approximated finite element field over the waveguide cross-section with exact time harmonic functions, $e^{i\left(\xi x-\omega t\right)}$, in the propagation direction, 'x'. The compatibility and constitutive equations can be written in synthetic matrix forms as:

$$\varepsilon = Du, \qquad \sigma = C^{*}\varepsilon \tag{22}$$

where ε and σ are the strain and stress vectors respectively, D is the compatibility operator, and C'' is the stiffness tensor. More details on the compatibility operator can be found in Hayashi et al. [8] and Bartoli et al. [9]. The principle of virtual work with the compatibility and constitutive laws, Equations (21) and (22), leads to the following energy balance equation

$$\int \delta u^{T} t\, d\Gamma = \int \delta u^{T}\left(\rho \ddot{u}\right) dV + \int \delta\left(uD\right)^{T} C^{*} Du dV \tag{23}$$

where Γ is the waveguide cross-section area, V is the waveguide volume, t is the external traction vector and the overdot implies time derivative. The finite element procedure reduces Equation (23) to the set of algebraic equations:

$$\left[A-\xi B\right]_{2M} Q = p \tag{24}$$

where the subscript $2M$ indicates the dimension of the problem with M, the number of total degrees of freedom of the cross-sectional mesh. Details on the complex matrices *[A]* and *[B]* can be found in Bartoli et al. (2006). By setting $p=0$ in Equation (24), the associated eigenvalue problem can be solved as $\xi(\omega)$. For each frequency ω, *2M* complex eigenvalues ξ_m and *2M* complex eigenvectors Φ_m are obtained. The solution is symmetric, i.e. for each pair (ξ_m - Φ_m), representing a forward guided mode, a pair exists representing the corresponding backforward mode (Hayashi et al. [8]). The first *M* components of Φ_m describe the cross-sectional mode shapes of the *m*-th mode. Once ξ_m is known, the dispersion curves can be easily computed. The phase velocity can be evaluated by the expression $c_{ph}=\omega/k_{real}$, where k_{real} is the real part of the wavenumber. The imaginary part of the wavenumber is the attenuation, att= k_{imag}, in Nepers per meter.

3.1.2 Global-Local Method

The global functions, represented by Φ_n, are the displacements that satisfy the governing equations in the absence of the discontinuity. The displacements at the mesh boundary are written as a sum of the contribution due to the incident wave and that due to the scattered waves. This displacement is then further used to satisfy the continuity conditions at the boundary. The displacements at the left boundary are written as:

$$u_l = u_{incident} + u_{scattered} = A_{in}\Phi_{in}^{+}e^{i\left(-\xi_{in}^{+}x^{-}\right)} + \sum_{j=1}^{N} A_j^{-}\Phi_j^{-}e^{i\left(-\xi_j^{-}x^{-}\right)} \qquad (25a)$$

$$u_l = A_{in}\Phi_{in}^{+}e^{i\left(-\xi_{in}^{+}x^{-}\right)} + \left[G^{-}\right]\left[D^{-}\right] \qquad (25b)$$

where the time-harmonic dependence is implicit.

Rattanawangcharoen et al. [4] give a detailed description of matrices [G$^-$] and [D$^-$]. In Equation (25), Φ^+ represents the modeshape of the incident waves travelling to the right, Φ^- represents the modeshapes of the reflected waves travelling to the left; A_{in}, Φ_{in}^{+}, and ξ_{in}^{+} represent the amplitude, modeshape and wavenumber of the incident wave respectively; A_j^- represents the unknown amplitude of the reflected waves; superscript '+' represents a wave travelling in the right and a superscript '-' represents a wave travelling in the left direction; x^- represents the absolute value of the distance of the left boundary from the center of the meshed region; *N* is the total number of modes considered. In the same way, the displacements at the right boundary are written as:

$$u_l = u_{incident} + u_{scattered} = A_{in}\Phi^+_{in}e^{i\left(\xi^+_{in}x^+\right)} + \sum_{j=1}^{N} A^+_j \Phi^+_j e^{i\left(\xi^+_j x^+\right)} \tag{26a}$$

$$u_r = A_{in}\Phi^+_{in}e^{i\left(\xi^+_{in}x^+\right)} + \left[G^+\right]\left[D^+\right] \tag{26b}$$

In Equation (26), $\mathbf{A}^+_\mathbf{j}$ represents the unknown amplitude of the transmitted waves and x^+ represents the absolute value of the distance of the right boundary from the center of the meshed region.

The forces at the boundaries can be calculated by computing the consistent nodal force vectors due to displacements (5b) and (6b). The nodal forces at the left boundary are:

$$f_l = -A_{in}F^+_{in}e^{i\left(-\xi^+_{in}x^-\right)} + \left[F^-\right]\left[D^-\right] \tag{27}$$

F_j is the consistent nodal force vector calculated from the displacement vector Φ_j. The nodal forces at the right boundary are:

$$f_r = A_{in}F^+_{in}e^{i\left(\xi^+_{in}x^+\right)} + \left[F^+\right]\left[D^+\right] \tag{28}$$

3.1.3 Finite Element Model for Local Region

The conventional discretization process in the finite element method yields:

$$\delta\left\{q^*\right\}\left[S\right]\left\{q\right\} - \delta\left\{q^*_B\right\}\left\{P_B\right\} = 0 \tag{29a}$$

$$\left[S\right] = \left[K_I\right] - \omega^2\left[M_I\right] = \begin{bmatrix} S_{II} & S_{IB} \\ S_{BI} & S_{BB} \end{bmatrix} \tag{29b}$$

$$\left\{q\right\}^T = \left\langle \left\{q_I\right\}^T \left\{q_B\right\}^T \right\rangle \tag{29c}$$

Here, $[K_I]$, and $[M_I]$ are global stiffness and mass matrices respectively; ω is the circular frequency; $\{q_I\}$ and $\{q_B\}$ are the nodal displacement vectors corresponding to interior and boundary nodes respectively; $\{P_B\}$ is the interaction force vector at the boundary nodes; and q^* denotes complex conjugate of q.

Forces on the boundary nodes due to the entire FE region, when displacement is imposed only on the boundaries, can be calculated by performing static condensation on $[S]$ such that:

$$\left[S^*_{BB}\right]=\left[S_{BB}\right]-\left[S_{BI}\right]\left[S_{II}\right]^{-1}\left[S_{IB}\right] \tag{30}$$

3.1.4 Global Solution

The nodal forces on the boundary due to displacements (5b) and (5b), as contributed from the FE portion, are:

$$f^{FEM}_{boundary}=\left[S^*_{BB}\right]\left\{\begin{matrix}\{u_l\}\\ \{u_r\}\end{matrix}\right\} \tag{31}$$

For traction continuity, from Equations (25), (26), and (21):

$$\left\{\begin{matrix}\{f_l\}\\ \{f_r\}\end{matrix}\right\}=f^{FEM}_{boundary}=\left[S^*_{BB}\right]\left\{\begin{matrix}\{u_l\}\\ \{u_r\}\end{matrix}\right\} \tag{32}$$

Rearranging the terms, the following final equation is obtained:

$$\left(\left[S^*_{BB}\right]\left[G\right]-\left[F\right]\right)\left\{D\right\}=\left\{P^B_{in}\right\}-\left[S^*_{BB}\right]\left\{q^B_{in}\right\} \tag{33a}$$

$$\left\{P^B_{in}\right\}=\left\{\begin{matrix}A_{in}F^+_{in}e^{i\left(-\xi_{in}x^-\right)}\\ A_{in}F^+_{in}e^{i\left(\xi_{in}x^+\right)}\end{matrix}\right\} \tag{33b}$$

$$\left\{q^B_{in}\right\}=\left\{\begin{matrix}A_{in}\Phi^+_{in}e^{i\left(-\xi_{in}x^-\right)}\\ A_{in}\Phi^+_{in}e^{i\left(\xi_{in}x^+\right)}\end{matrix}\right\} \tag{33c}$$

$$\{D\}^T = \left\langle \{D^-\}^T \quad \{D^+\}^T \right\rangle \tag{33d}$$

$$[F] = \begin{bmatrix} [F^-] & 0 \\ 0 & [F^+] \end{bmatrix} \tag{33e}$$

$$[G] = \begin{bmatrix} [G^-] & 0 \\ 0 & [G^+] \end{bmatrix} \tag{33f}$$

Equation (33a) is solved using least squares to calculate the coefficients A_j^-, and A_j^+. Reflection coefficients R_{ij} and transmission coefficients T_{ij} (due to the i^{th} incident mode) can be found by:

$$R_{ij} = {A_j^-}/{A_i} \tag{34}$$

$$T_{ij} = {A_j^+}/{A_i}\ ; j \neq i \tag{35}$$

$$T_{ij} = 1 + {A_j^+}/{A_i}\ ; j = i$$

3.1.5 Energy Conservation

Energies are carried only by the propagating modes, which include incident, reflected and transmitted modes. The time averaged values of energy flux associated with the j^{th} reflected and transmitted modes through the cross-section is given by:

$$I_{ij}^- = \omega |A_i|^2 |R_{ij}|^2 \alpha_j \tag{36}$$

$$I_{ij}^+ = \omega |A_i|^2 |T_{ij}|^2 \alpha_j$$

where

$$\alpha_j = \int_0^h F_j^{+} \overline{q}_j z dz \tag{37}$$

is the participation factor for the jth propagating mode.

3.1.6. Forced Solution from SAFE and Global-Local

SAFE can be used to compute the displacement time history at any point due to an arbitrary loading over a cross-section. The displacement field is written as a linear combination of the wave-modes present in the structure (Hayashi et al. [8]). Mathematically,

$$U = \sum_{m=1}^{M} \alpha_m \Phi_m^{Rup} \exp\left\{ i\xi_m \left(x - x_s \right) \right\} \tag{38}$$

where, Φ_m^{Rup} is the upper half of the right propagating m^{th} eigenvector, ξ_m is the corresponding eigenvalue, x is the coordinate location of the point in consideration and x_s is the coordinate location of the applied force; α_m represents the individual contribution of the m^{th} mode.

The displacement vector, U, is calculated from Equation (38) for discrete frequencies and an inverse Fourier Transform is used to invert the frequency domain to the time domain. For calculating time histories from the Global-Local method, the time domain forcing function is first converted to its corresponding frequency domain representation. For each frequency component, Equation (38) is used to express the displacement field due to the force as a linear combination of the displacement eigenvectors, Φ_m. For each such eigenmode contribution, Global-Local is then used to calculate the scattered field. This scattered field contributes to the total displacement at the point of interest. The final time history is found by inverting the sum of all such contributions for all the different excitation frequencies under consideration.

3.2. Results

3.2.1. Reflection for Notched Aluminum Plate

The first case examined is a semi-infinite isotropic plate with a notch defect. The plate modeled was aluminum, 1.58 mm (1/16 in) in thickness. The first notch considered was 0.16 mm in width and 0.32 mm in depth (Figure 16a). A finite region surrounding the notch (local domain) and extending into the thickness of the plate, was discretized by rectangular, four-node finite elements. A total of ten elements were used in the thickness of the plate, and the mesh was kept uniform throughout the local domain. SAFE was used for the global domain. The zero-order symmetric mode, S_0, was considered as the incident mode.

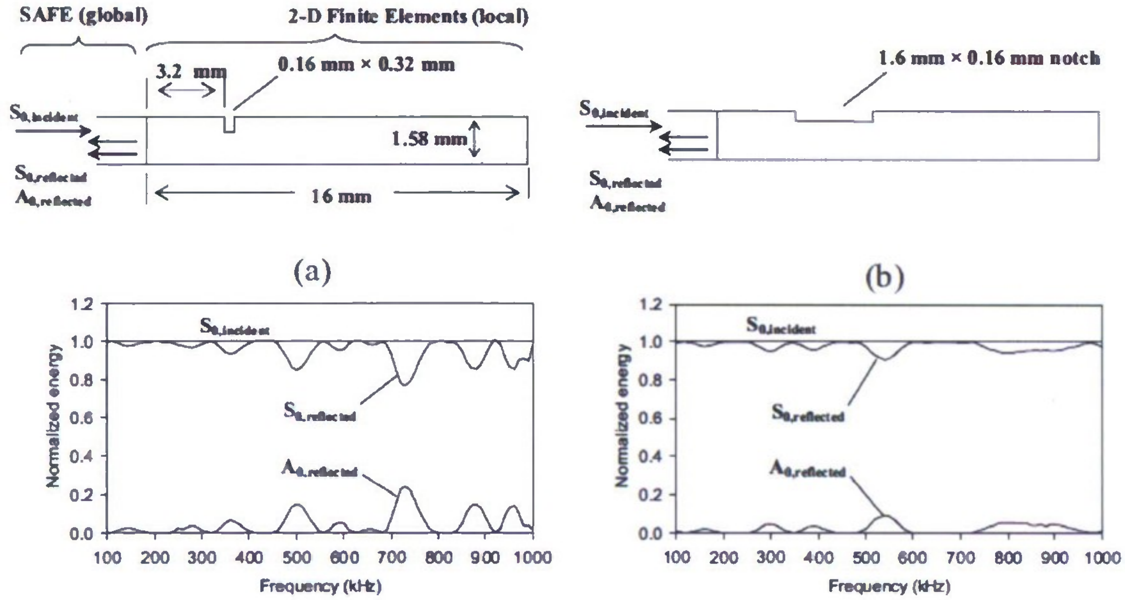

Figure 16. Results of S_0 wave scattering from defects in a plate from Global-Local models in reflection. (a) Energy spectra of reflected S_0 and A_0 (mode conversion) from sharp notch; (b) Energy spectra of reflected S_0 and A_0 (mode conversion) from shallow notch.

The results are shown in the plot of Figure 16a in terms of reflected energy relative to the incident, unit S_0 energy. As expected, the notch causes S_0 - A_0 mode conversion since it breaks the symmetry of the waveguide. As a check for the accuracy of the analysis, energy conservation is preserved as the reflected S_0 and A_0 energies sum to the incident S_0 energy. Mode conversion is found more pronounced at particular frequency values, namely 500 kHz, 730 kHz, 880 kHz and 950 kHz.

A more shallow discontinuity was examined next. This was a notch extending 1.6 mm in width and 0.16 mm in depth, which more closely represented corrosion damage (Figure 16b). It can be seen that the resulting reflection spectra are different for the two defect cases. For example, the strong S_0 - A_0 reflection at 730 KHz in the sharp defect is now completely absent in the shallow defect. Maximum S_0 - A_0 reflection for the shallow defect is, instead, found at 550 KHz where zero reflection is seen in the sharp defect. This suggests the potential for quantitative, rather than qualitative defect detection.

3.2.2. Reflection and Transmission for Notched Aluminum Plate

In this case the global-local method was used to predict the scattered field in both reflection and transmission. The plate modeled was aluminum, 1.6 mm in thickness with a half thickness notch in the middle. Transmitted and reflected S_0 and A_0 modes were computed for an incident S_0 mode. Energy conservation was again checked to test the validity of the method (Figure 17).

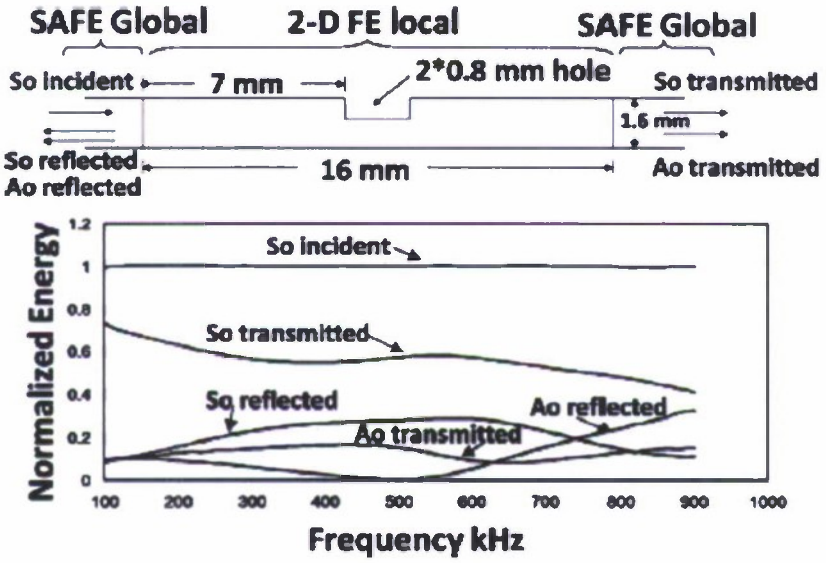

Figure 17. Results of S_0 wave scattering in a plate from Global-Local model in reflection and transmission.

3.2.3. Reflection and Transmission for Layered Composite

This example examined reflection and transmission in the more complex case of a layered composite plate. The plate modeled was 1mm thick and consisted of 8 layers of unidirectional carbon-epoxy laminae in a stacking sequence of $[0/+45/-45/0]_S$. Material damping was ignored in the present study. A defect of length 3mm, consisting of the removal of certain layers, was introduced at various locations across the cross-section of the laminate (Figure 18). The material density of each lamina was $\rho=1530\ \text{kg/m}^3$ and the elastic properties in the principal direction of material symmetry are given in Table 4, where 1 is the fiber direction, 2 is the direction perpendicular to the fibers in the laminate plane, and 3 is the through-thickness direction. For waves propagating along a direction x oriented at any angle θ with respect to the fiber direction, 1, the SAFE model simply requires the rotation of the stiffness matrix of each lamina through

$$C_\theta = R_1 C R_2^{-} \tag{39}$$

where $\boldsymbol{C}$ is the stiffness matrix in the lamina's principal direction, and R_1 and R_2 are the following rotation matrices:

$$R_1 = \begin{bmatrix} m^2 & n^2 & 0 & 0 & 0 & 2mn \\ n^2 & m^2 & 0 & 0 & 0 & -2mn \\ 0 & 0 & 1 & 0 & 0 & 0 \\ 0 & 0 & 0 & m & -n & 0 \\ 0 & 0 & 0 & -n & m & 0 \\ mn & -mn & 0 & 0 & 0 & m^2-n^2 \end{bmatrix} \tag{40}$$

$$R_2 = \begin{bmatrix} m^2 & n^2 & 0 & 0 & 0 & mn \\ n^2 & m^2 & 0 & 0 & 0 & -mn \\ 0 & 0 & 1 & 0 & 0 & 0 \\ 0 & 0 & 0 & m & -n & 0 \\ 0 & 0 & 0 & -n & m & 0 \\ -2mn & 2mn & 0 & 0 & 0 & m^2-n^2 \end{bmatrix}$$

with $m = \cos(\theta)$ and $n = \sin(\theta)$. The governing eigenvalue problem of SAFE in Equation (24) is then solved by using the rotated stiffness matrix in the constitutive relations.

C_{11}	135
C_{12}	5.7
C_{13}	5.7
C_{22}	14.2
C_{23}	8.51
C_{33}	14.2
C_{44}	2.87
C_{55}	4.55
C_{66}	4.55

Table 4: Elastic properties (GPa) for the CFRP lamina.

Figure 18 shows the scattered fields for an S_0 incidence over the defected layered composites. Three different defects are considered. Scattered fields from the removal of the top 2 layers (Figure 18a) are compared to the removal of the middle two layers (Figure 18b), and the removal of the top four layers (Figure 18c).

It can be seen that the reflection strength increases as the defect is moved from the top of the plate (Figure 18a) to the center of the plate (Figure 18b). This can be explained by the energy distribution in the fundamental symmetric mode over the cross-section of the plate. Figure 19 plots the Poynting vector for the S_0 mode at the frequency of ~400kHz across the cross-section of the composite plate, where the Poynting vector is:

$$P = -\frac{1}{2}\mathrm{Re}\left(\sigma \dot{u}^{*}\right) \tag{41}$$

where $\boldsymbol{\sigma}$ is the classical stress tensor, and $\dot{\boldsymbol{u}}^{*}$ is the complex conjugate of the particle velocity vector.

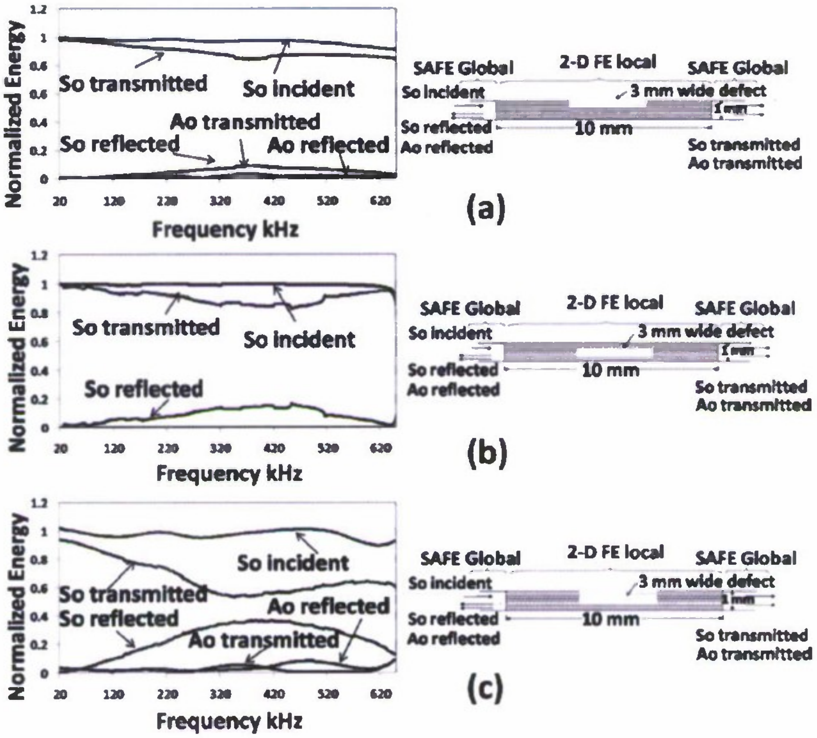

Figure 18. Results of S_0 wave scattering from defects in a $[0/+45/-45/0]_S$ CFRP laminate in reflection and transmission. (a) removal of top two layers; (b) removal of central two layers; (c) removal of top four layers.

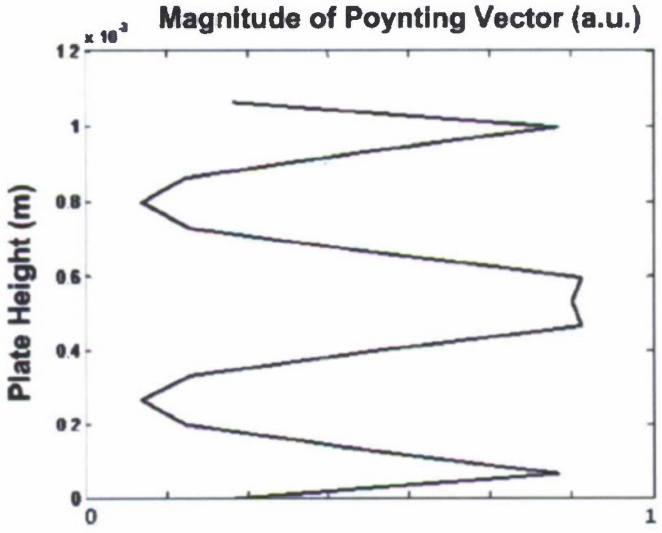

Figure 19. Poynting vector for S_0 at 400 KHz in the $[0/+45/-45/0]_S$ CFRP laminate.

Figure 19 shows that the energy carried by the S_0 mode in the direction of propagation is concentrated more around the center of the cross-section of the laminate than at its surface. Therefore, it is expected that this mode would be more sensitive to a central defect compared to a defect at the top or the bottom of the laminate. Figure 18a and 18b accordingly show an increased reflection of the S_0 mode when the middle 2 layers are removed as compared to the case when the top 2 layers are removed. In addition, mode conversion is completely absent in Figure 18b given the symmetry of the defect with respect to the cross-section; alternatively, considerable mode conversion of S_0 into A_0 is seen in Figure 18c because the defect breaks the symmetry of the cross-section. As expected, Global-Local predicts a significant increase in scattering as the defect size increases from 2 layer thicknesses to 4 layer thicknesses (Figure 18c).

A_0 incidence was studied next for the same composite plate. Figure 20 shows the scattered fields for the same. As in the previous problem, three different defects are considered (Figure 18 a-c).

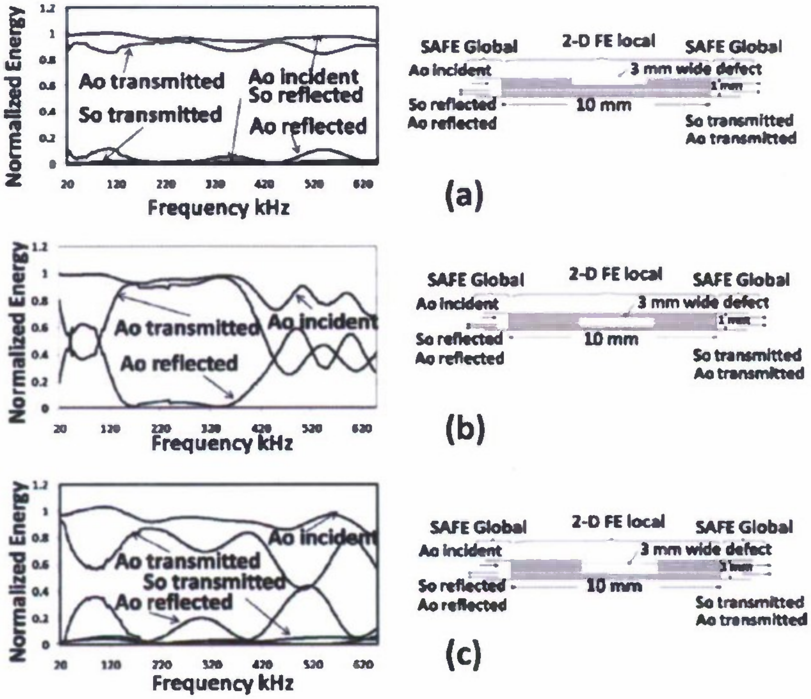

Figure 20. Results of A_0 wave scattering from defects in a $[0/+45/-45/0]_S$ CFRP laminate in reflection and transmission. (a) removal of top two layers; (b) removal of central two layers; (c) removal of top four layers.

Figure 21 shows the magnitude of the Poynting vector for the A_0 mode at 540 kHz. Similar to the case of S_0, a very large part of the energy is concentrated in the central portion of the laminate's cross-section. This explains the strong scattering from the central defect (Figure 20b) compared to the top defect of the same size (Figure 20a).

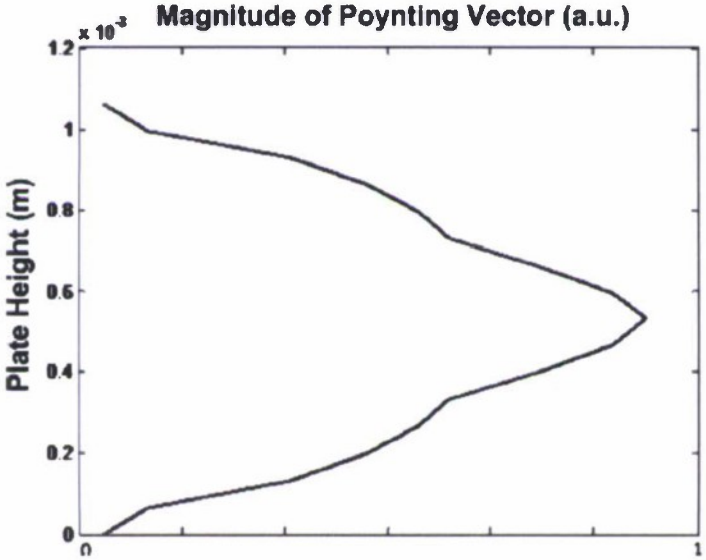

Figure 21. Poynting vector for A_0 at 540 KHz in the $[0/+45/-45/0]_S$ CFRP laminate.

It is likely that the finite element discretization was not adequate for solving the Global-Local problem at higher frequencies. This might explain why energy conservation for both S_0 and A_0 incidences (Figs. 18 and 10) is not completely satisfied at these frequencies. Since A_0 in general has a shorter wavelength compared to S_0, it is more affected by the finite element discretization. Moreover, the laminate being anisotropic, there is a coupling of the shear horizontal mode with both the S_0 and A_0 mode. This allows energy from the latter two modes to escape into the SH modes. Despite these limitations, the underlying physical behavior of the system is captured well.

3.2.4. Experimental Verification

The Global-Local method was also used to predict the time-domain waveforms in the CFRP $[0/+45/-45/0]_S$ composite plate subjected to broadband, pulsed laser excitation (ND:YAG, 10 nsec.

pulse duration). The response was experimentally measured for the case of a plate 1.0 mm in thickness with a sensor-excitation distance of 20 cm. The defect modeled was a delamination type defect extending in the thickness direction, in the middle of the 8-layered composite laminate. Figs. 22(a) and 22(b) show the comparison of the theoretical predictions with experimental results. The signals are normalized to their respective maximum values. It can be noticed that both the experimental and the numerical results match well in the time of arrival and phase characteristics of the signals. Moreover, a decrease in the damaged signal compared to the undamaged case, as predicted by the numerical model, is confirmed in the experimental results. Another interesting result is that both predictions and experiment show a velocity change between the undamaged and damaged cases. This is likely due to mode conversions.

3.3. Discussion And Conclusions

This section demonstrates the use of SAFE in a Global-Local framework that allows extracting information on guided waves scattered by defects in isotropic and layered anisotropic plates for quantitative structural health monitoring. The advantage of SAFE is its ability to handle the complex geometry of layered composites in a computationally efficient manner. The method was used in cases of notch-like defects in aluminum plates and delamination-like defects in layered composites. Both reflected and transmitted spectra of propagating modes were predicted. It should be noted that two different discretization are done in the solution of the problem. These affect the accuracy of the solution in different limiting regimes. For example, the thickness profile of the out of plane displacement component of the S_0 mode in an Aluminum plate varies from being approximately linear at an $f\,d$ value of 0.5 to a half wavelength sinusoid at $f\,d$= 3.0 (Rose 1999). This indicates that the thickness discretization of the Global part in Global-Local should be increased to adequately model the increasing nonlinear thickness variation of the modeshape as the frequency is increased. Higher order modes exhibit a more nonlinear modeshape compared to lower order modes. A_2 , for instance, has more wavelengths in its displacement thickness profile at $f\,d$= 5 than A_1 has at the same $f\,d$ value. Therefore, in general, a higher order mode needs a finer thickness discretization at the same frequency than a lower order mode in order to better approximate the true modeshape.

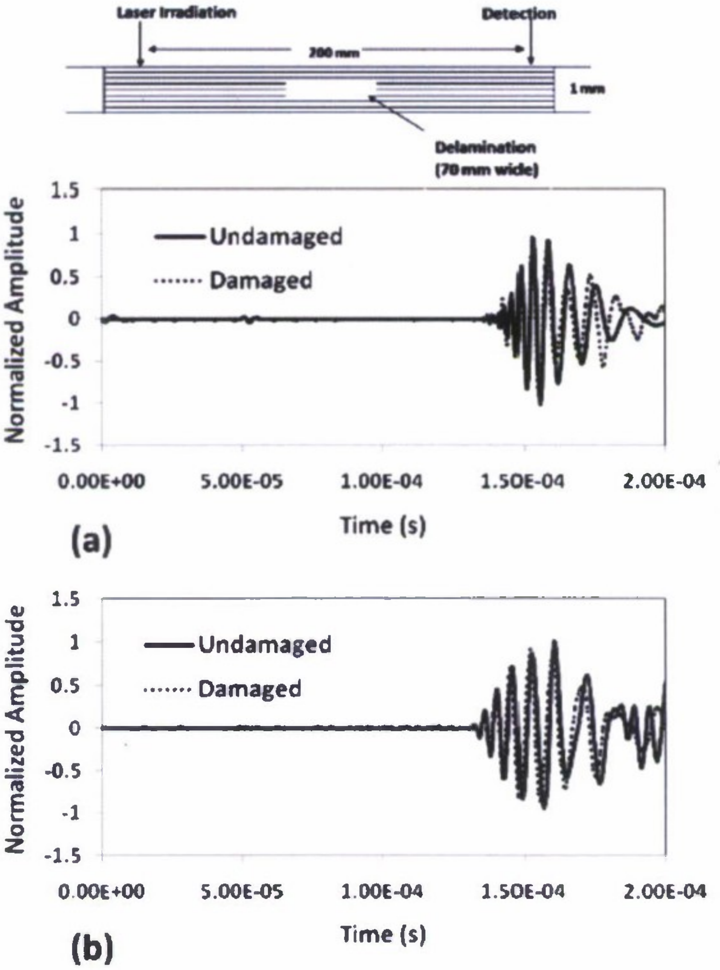

Figure 22. Time histories (normalized to max.) of response of damaged and undamaged $[0/+45/-45/0]_S$ CFRP laminate subjected to broadband laser excitation. (a) Global-Local predictions; (b) Experimental measurements.

The local discretization for the Finite Element part of Global local should also vary with frequency and the modes under consideration. At any given frequency, modes with shorter wavelengths require a finer FE discretization for good approximation. Modes with low phase velocities in the dispersion curve, therefore, require more finite elements per unit propagation distance for an accurate representation in the summation solution. For isotropic structures like an aluminum plate, since all the modes asymptotically approach a constant phase velocity (S_0 and A_0

converge to the Rayleigh surface wave velocity; higher order modes converge to shear wave velocity), the FE discretization should be made finer as higher frequencies are considered.

It was also shown that the wave time histories can be extracted from these models for an arbitrary excitation. The results shown are limited to a 2-D study. The extension of the work to 3-D cases and to adhesive bond assessment should be the subject of future work.

4. A TWO-STEP DATA-DRIVEN BOND DEFECT DETECTION AND CLASSIFICATION APPROACH

The research completed in the previous sections employed fundamental physics-based modeling to drive algorithm development. One of the limitations of the subsequent approach is the reliance on fairly simple structural waveguide geometries except through the cross-section. In order to fully augment this physics-based approach, this section employed a class of statistical pattern recognition algorithms originally developed in the vibration (lower-frequency acoustic) domain that are based on state space analyses using auto- or cross-prediction methods. These methods used chaotic excitations and attractor-based prediction error algorithms and have demonstrated the capacity to detect damage in various test bed structures with enhanced sensitivity over traditional vibration-domain analyses (Nichols et al. 2003; Todd, Erickson et al. 2004). Unfortunately, these chaotic excitations are also low frequency in nature and are therefore unable to localize damage within a structure. The work in this section uses the benefits of combining ultrasonic guided waves (small length and time scales) with chaotic excitations (which enable and enhance pattern recognition techniques) for damage detection of bolted and adhesively-bonded connections via bulk insonification. This synthesis of techniques is accomplished by shifting the energy of a low-frequency chaotic process, such as the common Lorenz signal, into the ultrasonic frequency range (>20 kHz) and launching it into the structure as a guided wave. The chaotic ultrasonic signals used here are fundamentally created via amplitude modulation, i.e., by multiplying a single ultrasonic frequency tone by an amplitude envelope that is created by a chaotic process. The waveform appears as a narrowband, chaotically-modulated signal centered at the same central frequency as the original ultrasonic tone. A chaotic waveform is able to enhance prediction error based damage detection features because the signal is deterministic, and because of the phase space diversity associated with the chaos. The deterministic aspect of chaotic inputs was used in the context of SHM by Todd et al. when they showed that an attractor-based detection feature had superior performance to modal-based features at detecting loss of stiffness in a computational spring-mass system when excited by a chaotic waveform (Todd et al. 2001). A number of studies involving chaotic excitation were then completed in the following years (Trickey et al. 2002; Nichols et al. 2003; Nichols, Todd, and Wait 2003; Moniz et al. 2004; Nichols et al. 2004).

4.1 Chaotic Ultrasonic Signal Creation

A chaotic ultrasonic waveform y_n is created by simple amplitude modulation of an ultrasonic carrier as detailed in the following Equation (41):

$$y_n = \sin(2\pi n f_c / f_s) \cdot (1 + d \cdot x_n) \tag{41}$$

where y_n is the modulated waveform, f_s is the sampling frequency (the hardware used in this dissertation samples maximally at 4 MHz for a high-fidelity waveform), f_c is the desired carrier frequency (typically, in the hundreds of kHz in the applications in this dissertation), d is the modulation depth, and x_n is a chaotic waveform produced by a separate chaotic process. Thus, the waveform x_n appears as a narrowband, chaotically-modulated signal centered at the desired central carrier frequency, f_c, or a chaotic ultrasonic wave (CUW). In this work, the chaotic process was obtained as the x_1 output of the well-known Lorenz system

$$\begin{aligned} \dot{x}_1 &= 10(x_2 - x_1) \\ \dot{x}_2 &= (-x_1 x_3 + 28x_1 - x_2) \\ \dot{x}_3 &= (x_1 x_2 - 8x_3 / 3) \end{aligned} \tag{42}$$

There is nothing unique about the Lorenz system for generating chaotic output; any system capable of producing a chaotic output is suitable, but the Lorenz system shown in Eq. (42) has a robust parameter region for producing chaotic output and was selected for this study. The Lorenz system is integrated using a time-step R/f_s, where R is a frequency ratio that can be modified to change the fundamental time scales of the chaotic signal. This dissertation uses several values of R that affect the frequency regime in which the power of the chaotic signal lies. This chaotic signal is normalized through division by the maximum of the absolute value of the signal so that the values range from -1 to 1. The modulation depth *d* controls signal bandwidth, and if it is greater than one, the resulting signal will be over-modulated and will result in a phase inversion at the points where $|d^*x_n|>1$. These phase inversions would be detrimental to any prediction algorithm, and *d* is therefore restricted to the range $0<d\leq 1$. Figure 23 shows the effect of changing the frequency ratio *R* and the modulation depth *d* on the time series and power spectral density of the interrogating wave.

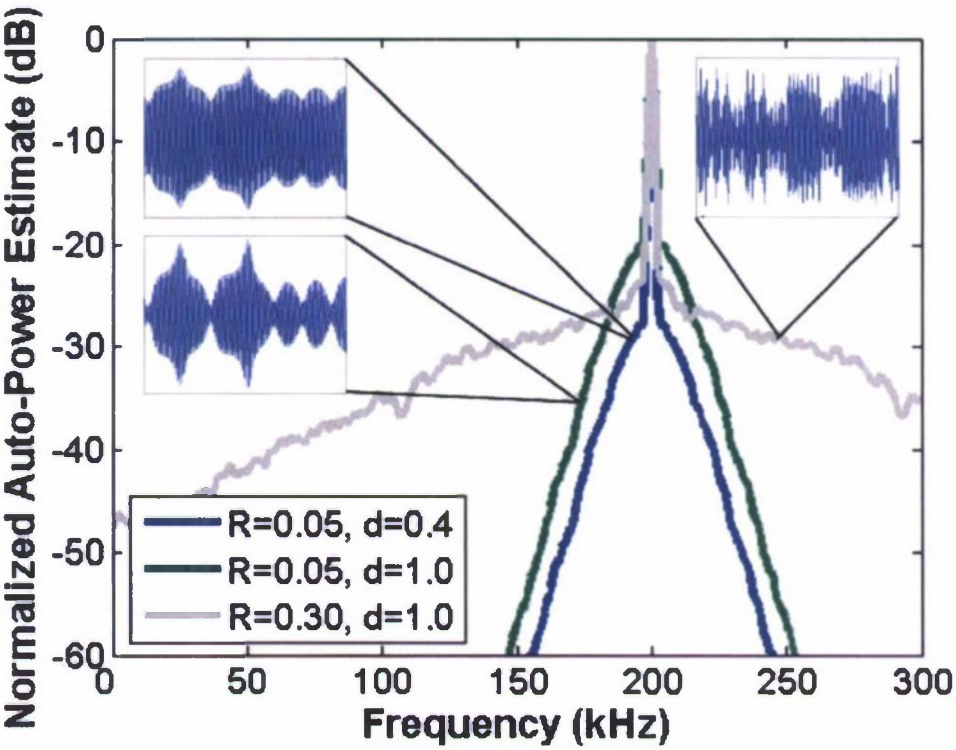

Figure 23. Modulated chaotic signal power spectral density and time series using $R = 0.05$ and $d = 0.4$ (upper left), $R = 0.05$ and $d = 1.0$ (mid left) and $R = 0.30$ and $d = 1.0$ (upper right).

4.1.1 Dimensionality of Chaotic Ultrasonic Signals

Recently, methods based on state-space analysis (of reconstructed dynamic responses) have been used as a means of change detection in SHM applications. In short, geometric objects that are akin to the true state-space attractors of the chaotic waveform are reconstructed by embedding timedelayed copies of the original time series into higher dimensions to create a pseudo-attractor in state-space from which various correlation or prediction metrics may be computed to facilitate the feature extraction part of the pattern recognition paradigm. Features that have been developed for state-space analysis in general include correlation dimension (Grassberger and Procaccia 1983; Logan and Mathew 1996), dynamic continuity (Pecora et al. 1997), nonlinear prediction error (Schreiber 1997), generalized interdependence (Arnhold et al. 1999), time scale separation (Cusumano and Chatterjee 2000), Lyapunov exponents (Trendafilova and Van Brussel 2001), local attractor variance ratio (Todd et al. 2001), parameter drift (Chaterjee et al. 2002), attractor dimension (Nichols et al. 2003) and phase space warping (Chelidze and Cusumano 2004). The idea is that these features may be compared between baseline and test cases to determine how the system response has evolved due to damage.

A critical issue when employing such state-space embedology methods is the embedding dimension choice that will be used in the pseudo-attractor reconstruction (Sauer et al. 1991). Every orbit in a multivariate space has a characteristic fractional dimension that describes the way in which the number of points within a sphere of radius *r* scales as the radius shrinks to zero. There are various methods for determining the fractional dimension of a signal (Abarbanel 1996). The reconstruction theorem states that at a minimum the embedding dimension must be at least twice the fractional dimension of a signal to ensure that the signal is completely unfolded in state-space and will behave dynamically similar to the true system. However, this is an upper bound to the choice of embedding dimension, and it is usually possible to embed in a smaller dimension than this sufficient criterion dictates.

In SHM applications, it is desirable to keep the embedding dimension as low as possible to maintain damage detection resolution (statistically, many observations of low-dimensional features are superior to fewer observations of high-dimension features for classification problems) and to reduce computational demands, where appropriate. A low embedding dimension is especially necessary if these attractor-based methods are to be employed in real-time monitoring systems, given the processing efforts required to execute them, e.g. nearest neighbors searching. In active sensing, where the interrogating ultrasonic waveform is prescribed with a certain dimension associated with the chaotic process used to create it, the signal is processed and received through various data acquisition and filtering components that themselves can be considered dynamic systems. It is known that these actions can affect the dimension of a process (Pecora and Carroll

1996). Therefore, a dimensionality study is undertaken to examine the possible effects that a standard DAQ process has on signal dimension through the launching process. The expected filtering due to waveform interaction with the structure itself may very well cause dimension increase as well, but undesired additional dimensional increase due to the DAQ, conditioning, or signal generation steps must be minimized for optimal efficacy of the overall approach.

A standard data acquisition (DAQ) process can be represented using the block diagram in Figure 24. The input analog signal is often first routed through an analog low pass anti-aliasing filter. This filtering process limits the power spectrum of the input signal to half of the sampling frequency (Nyquist frequency). The low pass filter is carefully applied so as not to mirror aliased spectral components into the frequency bandwidth that is to be examined. If this anti-aliasing filter is not applied correctly, there is no way in which to distinguish which part of the spectrum comes from the original input signal and which part of the spectrum is a result of the mirrored spectral components. An anti-aliasing filter with a sharp-cutoff frequency is required and can often be the most expensive part of a DAQ system. Therefore, on many less expensive DAQ cards, the sharp-cutoff filter is simply left off or converted to a more simplified anti-aliasing filter with a gradual cutoff and used in conjunction with oversampling to ensure that aliasing is not a problem.

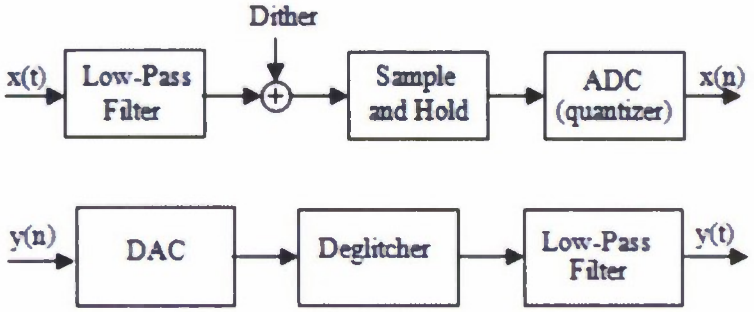

Figure 24. DAQ process block diagrams for analog-digital conversion (top) and digital-analog conversion (bottom).

The discrete time signal may then be subject to dithering, which adds Gaussian noise to the signal with magnitude on the order 0.5 LSB_{RMS}. This is used beneficially for applications involving averaging, such as calibration and spectral analysis. Oversampling cannot remove the quantization error that is inherent in ADC, but by combining oversampling, dithering, and averaging, the effects of quantization error can be effectively removed and the stepped nature of the signal that results from using a sample and hold circuit is eliminated. In high-speed DAQ processes that do not involve averaging or spectral analysis, it is usually a good idea to disable dithering to reduce unwanted noise.

Sampling of the analog input signal is achieved using a "sample and hold" circuit. This circuit takes the signal value at a particular sampling instant and holds it over the entire sampling period. The result is a stepped signal as is shown in Figure 25. This is a necessary step as the analog-to-digital converter (ADC) requires a constant value for a portion of the sampling period so that it has time to decide on the correct digital value to represent the analog voltage. The most common ADC in high-speed DAQ applications transforms the analog stepped signal from the output of the sample and hold circuit into discretely sampled digital binary values using a technique known as successive approximation. This process involves stepping through each value in the binary word from the most significant bit (MSB) to the least significant bit (LSB) to find the binary word value that most closely approximates the numerical analog value. Because only a certain number of digital values are available, depending on the length of the binary word used to describe a particular value (e.g. 12-bit or 16-bit), there is necessarily a quantization error during ADC. The effect of quantization error on dimension has been studied before, although not using this method, such as in Kumaraswamy et al. in which a mathematical relation between the performance of a vector quantizer and the intrinsic "fractal" dimension of a data set is established (Kumaraswamy et al. 2004).

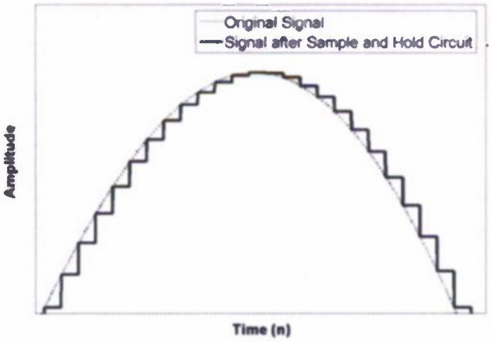

Figure 25. Example (idealized) output of a sample and hold circuit.

In many DAQ applications a digital signal must be converted into an analog signal, e.g. to drive an electromechanical shaker for vibration analysis of structures. This, for example, is a key component of modulated chaotic waves for use in ultrasonic active sensing for SHM. The first step is a digital-to-analog conversion (DAC), which generates a sequence of electrical pulses at each sampling time step whose amplitude is proportional to the value of the corresponding digital samples. The most common manner in which the amplitude of these pulses is determined is to sum the currents of switched current sources with respect to an analog reference voltage and is known as a multiplying DAC. If the conversion process involves digital samples with N-bit resolution, the converter provides N current sources. For instance, if the LSB of the digital word is represented by a current I, then each succeeding source has current values of 2*I, 4*I, all the way up to a value of 2^{N-1}*I for the MSB. Current sources are then switched on or off depending on the value of the corresponding bit of the digital word. Current sources are preferred over voltage sources for this method because they have a higher achievable conversion speed.

Unfortunately, in practical implementations when a DAC switches from one voltage level to another it produces glitches in the output analog signal due to released charges. The largest glitches occur when the MSB switches values. The result is a period in which the analog output value is uncertain. To combat this problem, a circuit known as a "de-glitcher" is used to sample the output of the DAC when it has reached a stable voltage and to provide an impulse at this voltage with a well-defined length, usually the sampling period. This process is known as a zero-order hold and results in a stepped signal. It is somewhat analogous to the sample and hold circuit used in ADC.

If the stepped analog signal received from the output of the de-glitcher circuit is input into an ideal low-pass reconstruction filter, the high frequency content (steps) of the signal is removed. The low-pass filter interpolates the digital samples to reproduce the intended analog output signal. In reality, an ideal low-pass filter cannot be achieved, and the amount of effort spent trying to closely replicate the ideal filter performance depends upon the application. In applications where the best possible reconstruction of the signal is desired, oversampling techniques which allow linear-phase filtering in the digital domain (FIR filters) are often used. Again, the use of an FIR filter will not increase the dimension of the signal.

4.1.2. Data Acquisition Simulation

The simulated DAQ system used in this work is designed to emulate the DAQ card that is being used in subsequent physical experiments, the National Instruments PCI-6036E. It does not incorporate an anti-aliasing low pass filter. Therefore, in this study, the effects of a low pass filter will not be examined. The card uses standard sample and hold circuitry and performs ADC using successive approximation and 16-bit resolution. Dithering is automatically enabled and cannot be turned off. DAC is performed using the multiplying method that is described above. No analog low pass filters are available so these effects will also not be considered.

A Lorenz chaotic signal is created using the system of equations shown in Eq. (42). This signal has significant frequency information from 0-10 Hz. In this study, the simulated "analog" version of the signal is discretely sampled at 50 kHz. The effect of dithering is then added to the signal by adding noise that ranges from ±0.5*LSB. The sample and hold circuit is implemented by sampling the simulated analog signal at 500 Hz. The ADC is simulated using a simple b-bit digitize function that transforms all the actual values of the signal to integers between $-2^{b-1}+1$ and 2^{b-1}. Signals are digitized using 4, 8, 12, 16, 20, and 24-bit ADC. After each step in the DAQ processes the dimension of the signal is verified using a false nearest neighbors (FNN) approach (Kennel and Abarbanel 1992).

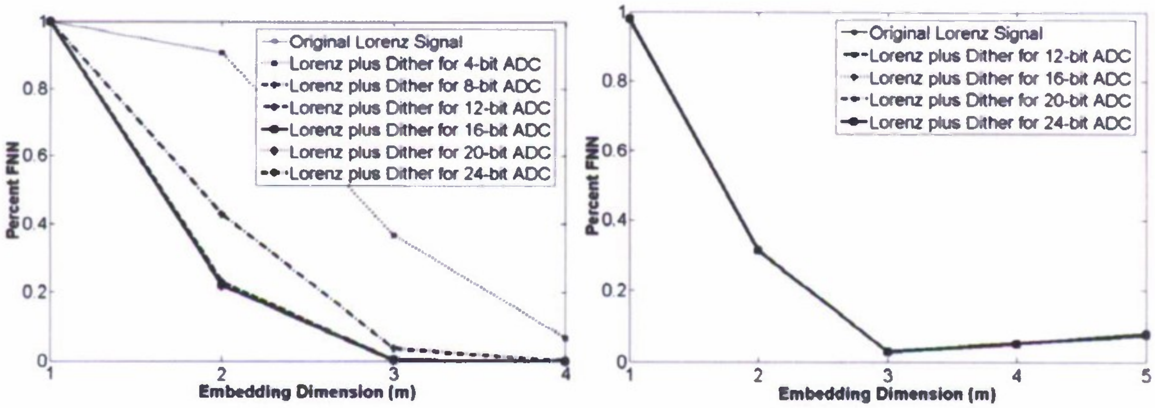

Figure 26. Embedding dimension after dithering for various levels of ADC resolution (left) and after sample-and-hold for various levels of dither (right).

Figure 26 (left) shows results of the FNN algorithm for the original "analog" signal as well as the "analog" signal plus dither for varying levels of ADC resolution. The signals corresponding to

4-bit and 8-bit ADC resolution are clearly higher dimensional than the remaining signals. This is because the amplitude of the dither added to the signal is large and, because white noise is infinite dimensional, the decreased signal-to-noise ratio (SNR) results in a higher dimensional signal. Therefore, using dither in ADC systems with low resolution without averaging is not suggested and will not be used for the remainder of this study. However, for ADC resolutions of 12-bits and above, the FNN approach cannot distinguish between the dithered and original signals. The proper embedding dimension for the original Lorenz signal is known to be *m*=3 which is the same result as is seen in Figure 26 (left).

The sample and hold circuit introduces a stepped nature to the signal which can be interpreted as high frequency content at each of the discontinuities. This high frequency content has an effect similar to noise contamination and will cause the percentage of FNN to level off or even begin to increase for higher embedding dimensions. This effect can be seen in Figure 26 (right). The original Lorenz signal and the dithered signals are indistinguishable after the sample and hold is performed, as one should expect since this was also the case after dither was added. For this case it is concluded that the proper embedding dimension is *m*=3 for all the signals, despite the rise in percent FNN for higher embedding dimensions. This decision is made knowing that there is some high frequency content that cannot be characterized for any embedding dimension, and so the lowest dimension that satisfactorily unfolds the original signal content is used.

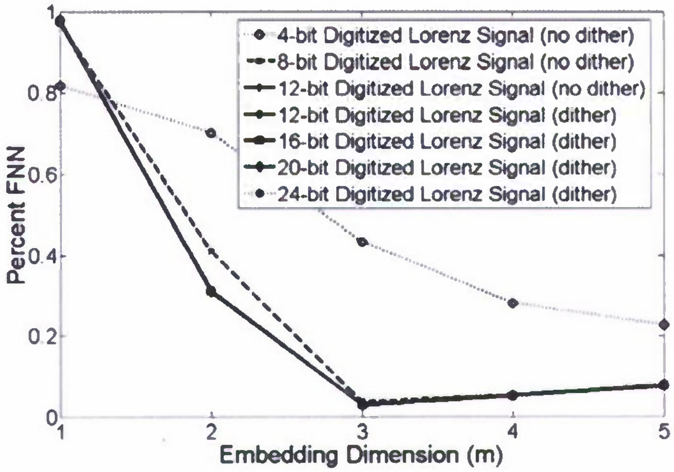

Figure 27. Embedding dimension after ADC for different ADC resolutions.

Figure 27 shows the signals after they have been put through the ADC. Clearly, using an ADC with low resolution (4-bit, 8-bit) results in increased embedding dimension. This is a direct result of the large quantization error for these low-resolution ADC systems. The discrete time signal of quantization errors is often uncorrelated in complex signals and can therefore be characterized as a white noise process. This addition of white noise to the signal reduces the SNR in much the same way as adding dither and can therefore increase the dimension of the signal. The SNR decreases by approximately 6 dB for each bit subtracted from the digital word length of the quantized samples. Thus, the SNR for a 12-bit quantizer is 24 dB higher than for an 8-bit quantizer. For ADC with a resolution of 12-bits and above, the embedding dimension remains unchanged.

As can be seen below in Figure 28, the embedding dimension increases as the frequency ratio *R* increases and the modulation depth *d* increases for a chaotic ultrasonic signal centered at 200 kHz. This result is expected because signal bandwidth rises as each of the two parameters increase, as is seen in Figure 23. As the bandwidth of the signal grows it differs more from a two-dimensional sine wave and becomes increasingly multi-dimensional. For chaotically amplitude-modulated signals the embedding dimension is unaffected during the DAQ process as long as the card has 12-bit precision or higher.

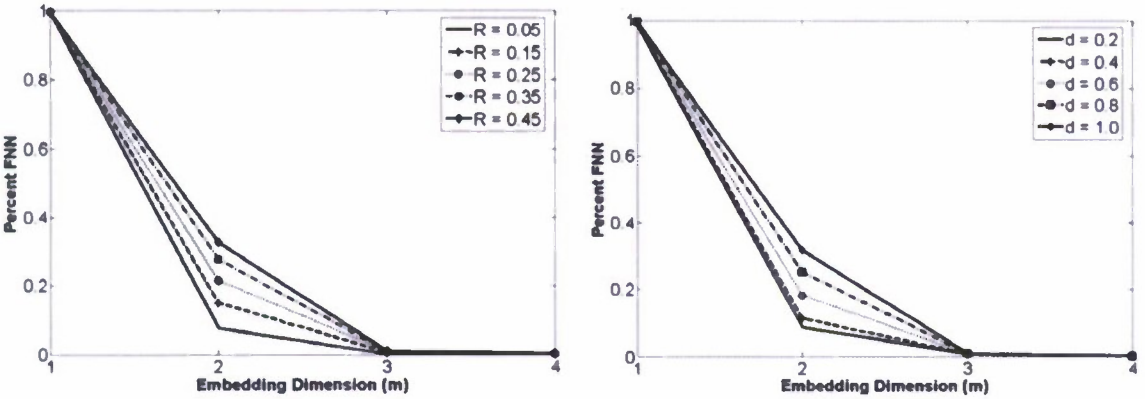

Figure 28. Embedding dimension of modulated signals using (left) $d = 1.0$ and (right) $R = 0.25$.

In order to verify simulation results that showed that there is no dimension increase using a DAQ card as the signal goes through a DAC or ADC process, a chaotic ultrasonic signal centered at 200 kHz is created and applied to the DAC on a 16-bit NI PCI-6036E DAQ card. That signal is then converted back to digital data using the DAQ card's ADC. The estimated embedding dimension of the signal that had been routed through the DAC and ADC was identical to the original signal as computed by FNN.

4.1.3. Effect of Signal-to-Noise Ratio

Signal-to-noise ratio (SNR) can be defined in decibel form using the following Eq. (43):

$$SNR(dB) = 20\log_{10}\left(\frac{A_{signal}}{A_{noise}}\right) \tag{43}$$

where A is the root-mean-square (RMS) value of the signal or noise amplitude. Therefore an order of magnitude increase in signal amplitude will result in the SNR rising by 20 dB. To identify the effect of SNR on signal dimension white noise is added to the standard Lorenz signal and then to a chaotic ultrasonic signal centered at 200 kHz. As can be seen in Figure 29, embedding dimension decreases as SNR increases. This agrees with prior observations made about the effect of SNR on embedding dimension.

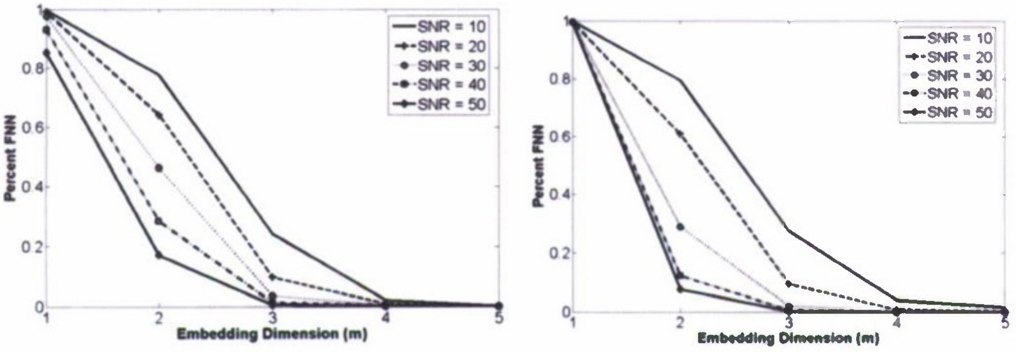

Figure 29. Embedding dimension of (left) standard Lorenz signal and (right) a 200 kHz chaotic amplitude-modulated signal for various levels of SNR.

This section outlined a method for creating chaotic amplitude-modulated ultrasonic signals. Several signal creation parameters are introduced and their effects on signal characteristics such as power spectral density are detailed. A study of the embedding dimension of chaotic ultrasonic signals (through the creation and data acquisition processes) is also presented. The concepts of state-space embedding and attractor reconstruction are introduced as a means to estimate embedding dimension. A low signal dimension is necessary to provide reduced processing and storage requirements and increase the ability of the system to resolve damage via statistically robust computation of features. It is shown that the DAQ process does not substantially alter the embedded dimension of a chaotic signal as long as the ADC/DAC resolution is at least 12-bits.

4.2. Damage Detection/Classification Scheme

Fundamental time series modeling where prediction power is required is often tackled via auto-regressive (AR) models, which have previously been shown to be useful as a damage classifier (Sohn and Farrar 2001; Sohn et al. 2001). The discretely observed output time series **x**(n) is modeled with an AR model (e.g., a finite impulse response filter) of the form:

$$\mathbf{x}(n)=\sum_{i=1}^{p}\alpha_i\mathbf{x}(n-i)+\mathbf{e}(n) \tag{44}$$

where p is the order of the AR model with associated coefficients α_i and residual error **e**(n). This dissertation examines various model orders p to determine the most suitable model order for each particular damage detection scheme. The AR coefficients are estimated through minimization of the sum-of-squared forward prediction errors (Brockwell and Davis 1991). All signals are normalized through division of the standard deviation of the signal before use of the AR model.

The calculated AR coefficients themselves can be used a damage-sensitive feature. This dissertation examines the ability of a two-part classification scheme to determine the existence and size of damage in a structure using a *supervised learning* paradigm. This classification scheme can also be employed with an *unsupervised learning* technique to classify whether a structural connection for which there is no baseline data is damaged or undamaged. The classification approach uses features derived from an autoregressive (AR) model coefficient vector cross-assurance criterion as well a group classification scheme with its basis in information theory. Throughout this section, data from a physical experiment on several composite adhesively-bonded wing-to-spar test structures, that will be discussed in detail later in this report, is used to illustrate the effectiveness and necessity of the two-part damage classification scheme. Two of these structures have various disbonds built into the bond line through the use of Teflon inserts and one of the structures has no damage built in. The experiment outlined later uses the two-part supervised learning classification scheme outlined in this section to not only to classify disbond size but also to classify whether a bond for which there is no baseline data is undamaged or has some form of disbond.

4.2.1. Vector consistency criterion

The first step in the damage classification algorithm is based on a comparison of AR coefficient vectors. Figure 30 shows averaged AR coefficients that are acquired using an AR model order of p=10 for three different bond conditions, including an undamaged bond as well as two different disbond sizes on a single adhesively-bonded composite test structure. Figure 30 (right) shows averaged AR coefficients that are acquired using an AR model order of p=10 for three different undamaged bond conditions on a similarly configured test structure. The figures show a clear difference in the shape of the AR coefficient vectors for different bond conditions whereas all undamaged bond conditions result in similarly shaped AR coefficient vectors. This result suggests that a metric which compares the shape of two AR coefficient vectors will be a damage-sensitive feature.

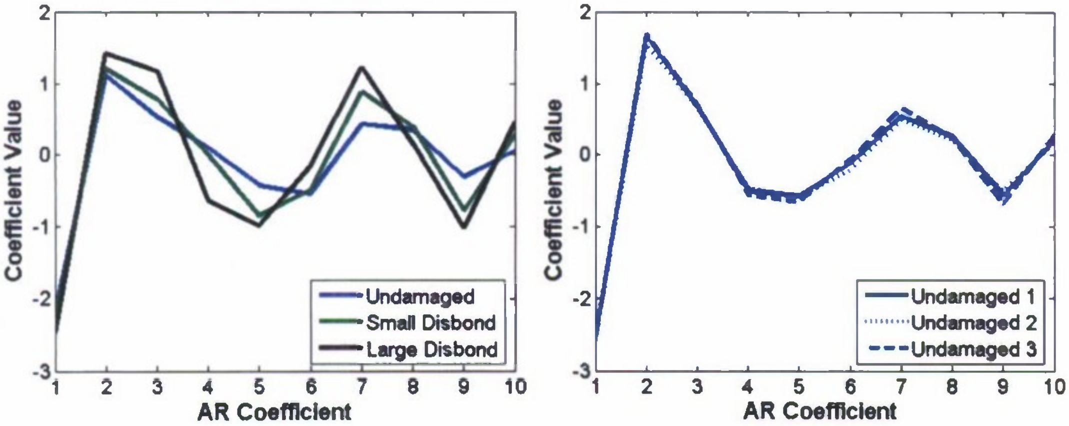

Figure 30. Averaged AR coefficient vector comparison for (left) different bond conditions and (right) three undamaged bond conditions.

A feature based on the modal assurance criterion (MAC) that is commonly used in modal analysis to provide a measure of consistency between estimates of a modal vector was proposed (Allemang 2003) . The MAC is a scalar value detailing the linear relationship between a test modal vector and a reference modal vector as follows:

$$MAC_{tr} = \frac{\left|\{\psi_t\}^H \{\psi_r\}\right|^2}{\{\psi_t\}^H \{\psi_t\}\{\psi_r\}^H \{\psi_r\}} \tag{45}$$

where ψ_t is the test modal vector, ψ_r is the reference modal vector, and H indicates the Hermitian operator or complex conjugate. The modal assurance criterion can have values ranging from zero, representing no consistent correspondence, to unity, representing complete consistent correspondence. Therefore if the two vectors are consistently related, then the MAC value should approach unity. This study uses a vector consistency criterion (VCC) similar to the MAC in order to measure the orthogonality of AR coefficient vectors. In this case the Hermitian operator simplifies to a vector transpose because the values of the AR coefficient vector are always real. The fact that the VCC feature can only have a value between zero and unity makes it useful as an extracted feature because scaling effects of the original signal will not affect any decision that needs to be made regarding the bond condition assessment. The hypothesis being tested is that two AR coefficient vectors should be very consistent (nearly orthogonal) if they are derived from modeled responses of structural connections with the same level (or lack of) damage.

4.2.2. Step one: damage existence classification

The determination of whether a connection of unknown condition is undamaged or damaged is accomplished using the following method. First, a set of distinct 250-microsecond-long input signals are created from the data-generating process that has been previously described. For each of these input signals a structural response is recorded once under each of the known undamaged and damaged conditions on a particular specimen, using a different actuator/sensor pair for each bond, as well as a second time for the undamaged condition. AR coefficients are then estimated for each of these structural responses. These sets of AR coefficients form a database of structural responses for known structural conditions with each input signal that will be used to determine the condition of an unknown connection in a *supervised learning* fashion.

For the first step of the bond condition assessment algorithm, which will identify only whether an unknown connection is damaged or undamaged, a distribution of VCC values is then calculated. This is accomplished by comparing, using Eq. (45), each of the AR coefficient vectors from the first set of waveforms to probe the undamaged connection with each of the AR coefficient vectors from the second set of waveforms to probe the undamaged connection. This calculation results in a large distribution of VCC values that describe the auto-correlation between the two sets of AR coefficient vectors that are both derived from the undamaged connection condition. A new set of input signals (created from the same underlying process as the supervised learning database input signals) are then applied to the structure for a structural connection whose damage state needs to be determined. AR coefficient vectors are again calculated for each of these new structural responses. The AR coefficient vectors from the original undamaged connection condition are then compared with the new set of AR coefficient vectors from the unknown connection condition by calculating VCC values. This computation results in a second distribution of VCC values that describe the correlation between the AR coefficient vectors of the undamaged connection condition and the AR coefficient vectors of the unknown connection condition.

A statistical measure must now be devised that can properly classify a damaged structural connection and at the same time properly classify an undamaged connection in a different geometric location using a different MFC sensor/actuator pair than the baseline undamaged connection. Figure 31 (left) shows empirical probability density functions (pdfs) of VCC values for three different bond conditions, including an undamaged bond as well as two different disbond sizes from a single adhesively-bonded composite test structure. Figure 31 (right) shows empirical pdfs of VCC values for three different undamaged bond conditions in different geometric locations on a different, but similarly configured, test structure. It is clear that while there are differences in the pdfs of the undamaged bonds in Figure 31 (left), the difference between the pdfs of the undamaged bond and two disbond sizes in Figure 31 (right) are much greater. A statistical decision boundary that can account for the small differences in the pdfs due to geometric conditions as well as MFC bonding characteristics while still correctly classifying the damaged bonds would be beneficial. The pdfs are not normally distributed as can be seen from the elongated left tail. Therefore standard statistical tests that assume normality such as the Student's t-test cannot be used in this case. There are several non-parametric tests that can be employed for non-Gaussian distributions such as the Kolmogorov-Smirnov test or the Mann-Whitney U test, but for this application these tests decidedly classify the various undamaged pdfs as being from different parent distributions. A solution to this problem is to set a lower confidence limit on an undamaged pdf so that the other undamaged pdfs would not result in a significant number of outliers (VCC values less than the lower bound) but still produce a significant number of outliers for the damaged pdfs.

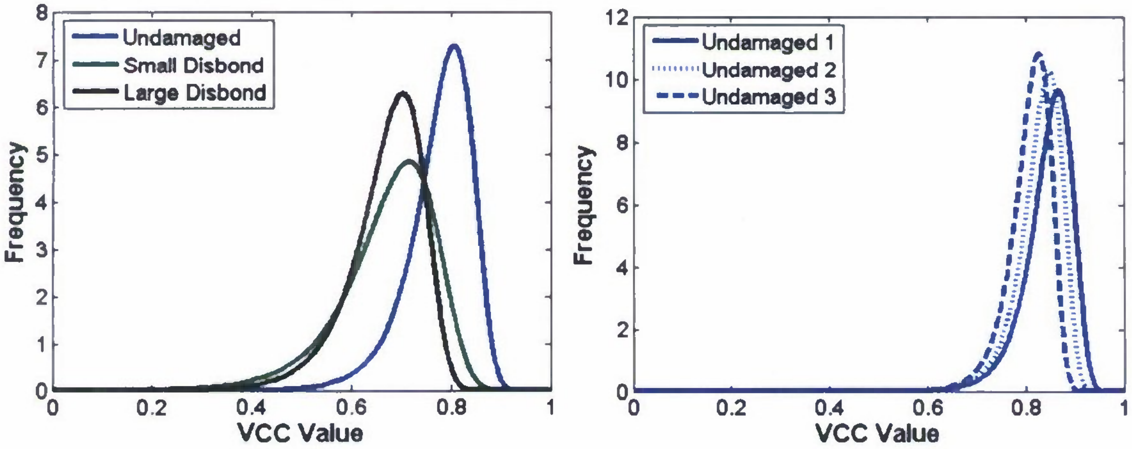

Figure 31. VCC value empirical pdf comparison for (left) different bond conditions and (right) three undamaged bond conditions.

Extreme value statistics (EVS) are used to set the lower confidence limit on the non-normal distributions that are produced using the above outlined method. EVS is used in this analysis to accurately model the behavior of the feature distribution's tails. The basis of this branch of statistics stems from the following situation. If a moving window is taken along a vector of samples and an extremum value (minimum or maximum) is selected from each of these windows, the induced cumulative density function of the extrema of the samples, as the number of vector samples tends to infinity, asymptotically converges to one of three possible distributions: Gumbel, Weibull or Frechet (Castillo 1988). The following equations detail the Gumbel, Weibull and Frechet distributions for minima because that is what this study uses.

Gumbel: $$F(x) = 1 - \exp\left[-\exp\left(\frac{x-\lambda}{\delta}\right)\right] \quad -\infty < x < \infty \ \text{and} \ \delta > 0 \tag{46}$$

Weibull: $$\mathrm{F(x)} = \begin{cases} 0 & \text{If x} \leq \blacklozenge \\ 1 - \exp\left[-\left(\frac{x-\lambda}{\delta}\right)^{\blacklozenge}\right] & \text{otherwise} \end{cases} \tag{47}$$

Frechet: $$F(x) = \begin{cases} 1 - \exp\left[-\left(\frac{\delta}{\lambda - x}\right)^{\beta}\right] & \text{If } x \leq \lambda \\ 1 & \text{otherwise} \end{cases} \tag{48}$$

where λ, δ, and β are the model parameters that are estimated from the data. There are similar functions that apply to the converged distributions for the maxima of the sample sets.

The appropriate distribution is chosen by plotting the cumulative distribution function (cdf) of the extracted vector of minima on the probability paper for a Gumbel distribution (Castillo 1988). Probability paper is designed so that the cdf for a particular cumulative distribution will plot in a linear fashion by transforming the vertical scale of the plot. In this case, if the vector of minima has a Gumbel minimum distribution, the cdf will be a straight line when plotted on Gumbel probability paper. Otherwise, the cdf will have an associated curvature. If this curvature is concave, the feature vector has a Weibull minimum distribution. Similarly, if the curvature is convex the feature vector has a Frechet minimum distribution. In this study the distribution of minima taken from the parent undamaged VCC distributions has a Gumbel minimum distribution. Model parameters are then estimated by fitting the chosen distribution to the data as outlined in Castillo (Castillo 1988).

Once the model parameters are chosen, it is possible to generate confidence limits that can be applied to the distribution. These limits are far more accurate than those obtained when assuming a Gaussian distribution. The threshold corresponding to a specific confidence level for the Gumbel minimum distribution is given by the following equation (Worden et al. 2002):

Gumbel: $$x_{\min} = \lambda + \delta \ln\left[-\ln\left(1 - \frac{n\alpha}{2}\right)\right] \tag{49}$$

where n is the window size used to extract the maxima, and α is the associated Type I error of the confidence limit. Type I error is simply the percentage of false positives that are expected to appear. For example, when using a 95% confidence interval the Type I error is expected to be 5% ($\alpha = 0.05$). By using the confidence limit calculated through EVS the damage state classification algorithm is able to differentiate between undamaged and damaged connections. To further differentiate between different sizes, levels or types of damage a second classification scheme is used.

4.2.3. Step two: damage size/type classification

This part of the project developed a novel statistical classification technique with its basis in information theory to classify different sizes, levels or types of damage in bonds. The classification method is based on a fundamental theorem of Shannon's information theory that states that "the best compression for any given data set comes from a codebook designed exactly for the statistics of that source; any other codebook will give worse results" (Shannon 1949). Recently, information theory has been applied to continuous time signals, where compression performance is related to prediction error, and a codebook is the model for a source that produces time series data. In this study the source is a chaotic guided wave propagating through a structural connection. These time series can then be classified using prediction error as a means of virtual data compression (via the AR coefficient vectors). The model for the response time series is the same auto-regressive model used for the undamaged/damaged discrimination that has already taken place. This idea leads to a procedure for classifying time series using cross-prediction error, as literal "data compression" in the sense of maximal information recovery on decompression is not actually necessary, just its "virtual" performance as a representative data model. Of course, the better the underlying statistical model is the more the classification performance will improve.

The entire damage state classification technique can be summarized as follows. The same database of AR coefficients that was created using a set of chaotic ultrasonic guided waves is again used to decide the state of the damaged connection. In this case only AR coefficients from the damaged paths are used because it is now known that the test path has some form of damage after using the first classification technique. A new input signal (created from the same underlying process as the training database input signals) is then applied to the structure along the known damaged bond condition path. One of the sets of AR coefficients in the training database for each of the paths with disbond damage is then used to estimate the structural response to the new input signal. One set of coefficients from the training database will minimize the sum of the squared residual errors and these coefficients are associated with a known size, level or type of damage in the training database. This damage state is then classified as the state of the unknown connection that is being probed. This comparison takes place for each of the remaining input signals in the training database. This entire process is then repeated using a large set of input signals that are imparted to the structure in its unknown damage state (the same data as was used in the first classification step). The votes for each damage state are then summed and the plurality of votes is the estimated condition of the bond. The entire two-part statistical damage state classification paradigm is depicted visually Figure 32.

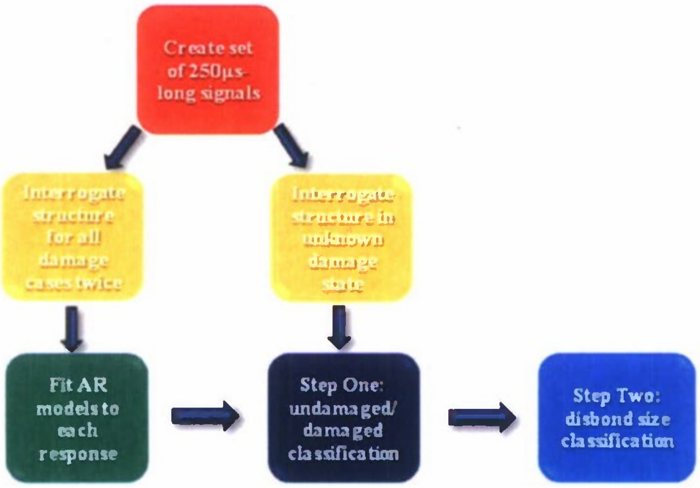

Figure 32. Ultrasonic statistical classification paradigm.

4.3. Experimental Validation on Adhesively-Bonded Composite Joints

4.3.1. Single Composite Plate Tests

This study applies the method outlined above to classify different bond state damage conditions of an adhesively-bonded composite joint, including various disbond sizes and a poorly-cured bond. The test structure is analogous to a wing skin-to-spar bonded joint and consists of a custom made 8-ply $[0/\pm45/0]_s$ carbon fiber-reinforced plastic (CFRP) plate that is bonded to a tubular CFRP spar (see Figure 10). The CFRP plate measures 12 in x 12 in x 0.04 in, and the spar has an outer square diameter of 2 in x 2 in with a wall thickness of 0.25 in. The bonded area contains two different sizes of disbond (0.25 in^2 and 1.0 in^2) created using Teflon inserts as well as a portion of the bond that has been poorly cured by using only 50% of the prescribed level of hardener. An active excitation signal is imparted to the structure through a MFC patch on one side of the bonded joint and sensed using an equivalent MFC patch on the opposite side of the joint and there is an MFC actuator/sensor pair for each bond condition to be identified.

Two MFC actuator/sensors were attached to the structure on each side of the bond for each of the three damaged bond states as well as one pair for the undamaged bond area for a total of eight MFC patches. Each MFC patch is affixed to the structure one inch from the spar bond line. Each input signal is applied to the structure 25 times and then averaged and filtered to reduce experimental noise. The actuation signal is created by the output channel of a National Instruments PCI-6110 DAQ card at a rate of 4 MHz and routed through a Krohn-Hite 7602 wideband power amplifier. This amplified signal is sent to the actuation MFC while the sensing MFC simultaneously samples the structural response at a rate of 4 MHz.

For the following experiments, 30 time response histories are created using a specific set of signal creation parameters. Half of these 30 generated response time histories are selected as database training inputs. The remaining 15 responses are used as test set inputs. All four bond conditions are probed three times with the first two time history responses being used for the training database and the remaining responses used to determine bond condition for the test set inputs. In each case the actual bond condition is determined based solely on knowledge it acquired from the 15 database training inputs.

In order to determine the set of input signal parameters that produce optimal bond state identification, the statistical classification scheme is employed for an array of signal parameters and the overall ability of each set of parameters to correctly identify each bond state is then examined. Previous numerical and experimental work done by Matt, Bartoli and Lanza di Scalea on the same test structure showed that, when using through transmission characteristics of simple toneburst inputs, an excitation frequency of 200 kHz was best able to identify bond state condition due to a coupling of S_0 and A_1 modes at that frequency (Matt et al. 2005; Lanza di Scalea et al. 2007). In this study a number of excitation center frequencies from 100 kHz to 300 kHz are considered, as well as frequency ratios ranging from 0.01 (nearly sinusoidal) to 0.50 (highly chaotic). When considering the feature extraction parameters a number of AR model orders from 3 to 25 are employed. Figure 33 depicts the ability of the statistical classification scheme to correctly identify bond condition by plotting the percentage of correct votes against the various signal input and feature extraction parameters already discussed.

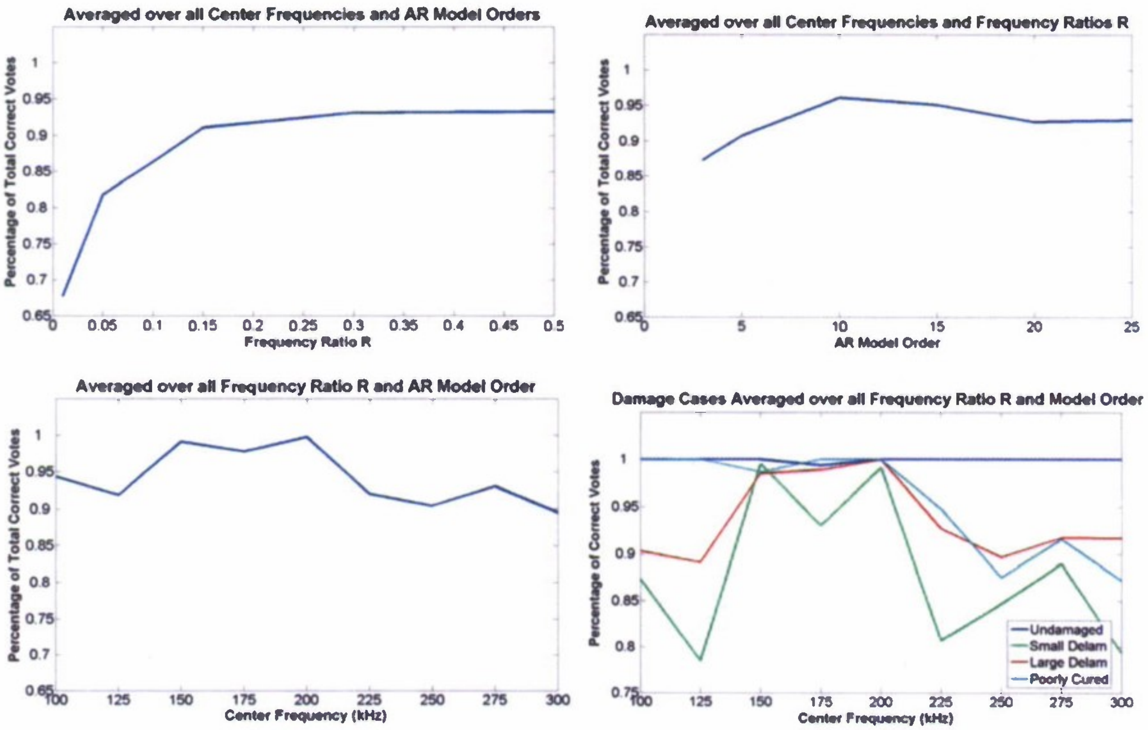

Figure 33. Classification scheme results showing percentage of total correct votes vs. (top left) frequency ratio, (top right) AR model order, (lower left) center frequency and (lower right) center frequency for each individual bond condition.

The top left plot of Figure 33 shows the ability of the statistical classification scheme employed together with chaotic insonification to correctly identify bond condition for various frequency ratios. As previously mentioned, the lower the frequency ratio the more sinusoidal the input signal appears and conversely the higher the frequency ratio the more chaotic the input signal appears. This signal parameter characteristic occurs because as the frequency ratio becomes small, the chaos operates on a longer time scale. If a small enough time window is used to create the signal, a very small *R* value will result in the chaotic time scale being much longer than that of the entire signal. In this case the signal will appear to be almost sinusoidal. The opposite effect holds true if a large frequency ratio is used because the time scale the chaos operates on will be much smaller than the length of the signal and the signal will therefore contain more chaotic information. It is clear that a signal with more chaotic information, when paired with this pattern recognition scheme, is best able to determine true bond state condition. There is negligible difference between a frequency ratio of 0.3 and 0.5 but the overall trend that a more chaotic signal provides greater classification ability is a sufficient conclusion. The upper right plot depicts the effect of AR model order on the damage identification ability of the statistical classification scheme. In general, if too low of an AR model is used (anything less than 10) the percentage of total correct votes has a noticeable decrease. When averaged over all frequency ratios and center frequencies an AR model order of 10 does slightly better than higher AR model orders. However, the effectiveness of a particular model order is clearly dependent on the particular frequencies in which the chaotic information is present. A closer investigation of the data reveal that, depending on the signal input parameters, an AR model order somewhere between 10 and 20 will produce optimal classification of each particular bond state.

The lower left plot in Figure 33 illustrates the effect of various center excitation frequencies on the ability to correctly classify bond condition. The graph shows that center frequency is a highly important parameter as there appears to be "sweet spots" where the algorithm correctly classifies almost 100% of individual test cases (150 kHz and 200 kHz) as well as several frequencies which do not perform as well including 175 kHz which is intermediate to the two sweet spots in the frequency regime. As previously mentioned, numerical simulations (Matt et al. 2005) showed a mode coupling occurring at 200 kHz which could be the reason for the excellent performance of the damage detection algorithm across all frequency ratios and model orders at that frequency. The same study does not indicate a mode coupling effect at 150 kHz. However, these are only numerical results, and the true physical structure may contain modal coupling effects at 150 kHz. Finally, the lower right plot of Figure 33 shows that the undamaged bond condition is correctly identified for almost 100% of the individual input signals for any center frequency. The ability to discern the poorly cured bond state appears to decrease as center frequency increases and the small disbond case is the most often misidentified bond condition, as would be expected due to its size.

4.3.2. Temperature Variability

The experimental apparatus used in this study is meant to simulate a wing skin-to-spar bonded joint that is used in aerospace applications. Therefore, if this statistical classification scheme using chaotic insonification is to be used for *in situ* health monitoring, including in-flight and on the ground, its behavior and effectiveness relative to external temperature must be considered. This study therefore employs the use of a thermal chamber to test the efficacy of the above outlined method for temperatures varying from -40°C to 40°C, a range that covers most flight and ground conditions. For the thermal chamber test a center frequency of 200 kHz, frequency ratio of 0.5 and AR model order of 10 are employed as these parameters produced near 100% correct identification of individual test signals for the room temperature experiments. Figure 34 shows the initial thermal chamber results for cases in which the baseline AR coefficients are determined at various temperatures. It is clear that the damage detection algorithm only performs well at temperatures close to that of the temperature at which the baseline AR coefficients are determined. A temperature change of more than 10 degrees Celsius usually results in significant reduction of classification effectiveness. However, when the proper baseline AR coefficients are used for a particular temperature the statistical classification method still achieves near 100% correct classification of individual test signals.

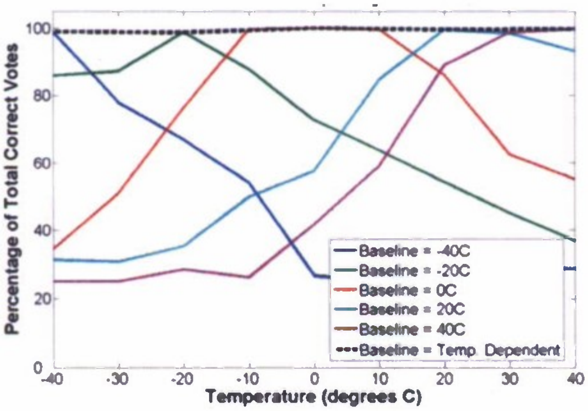

Figure 34. Percentage of total correct votes vs. temperature for cases in which the baseline AR coefficients are determined at various temperatures.

It is therefore possible to correct for temperature variations by storing baseline AR coefficients for the range of temperatures that the intended apparatus is likely to see during real world applications. It still must be determined how many sets of baseline AR coefficients must be stored and what the proper method for interpolation between these temperatures is. Therefore, this study examines using baseline AR coefficients taken every 20 degrees Celsius (-40°C, -20°C, 0°C, 20°C, 40°C) which is referred to in the following figures as 5tempbase and using baseline AR coefficients taken every 10 degrees Celsius (-40°C, -30°C, -20°C, -10°C, 0°C, 10°C, 20°C, 30°C, 40°C) which is referred to in the following figures as 9tempbase. Testing was carried out at 5 degree Celsius temperature increments. It can be seen in Figure 35 that the value of each AR coefficient tends to shift in a fairly reliable manner, usually in a near linear fashion, as the temperature changes. It is then possible to create a baseline of AR coefficients at all temperatures using polynomial fits from testing carried out at only a few intermediate temperatures.

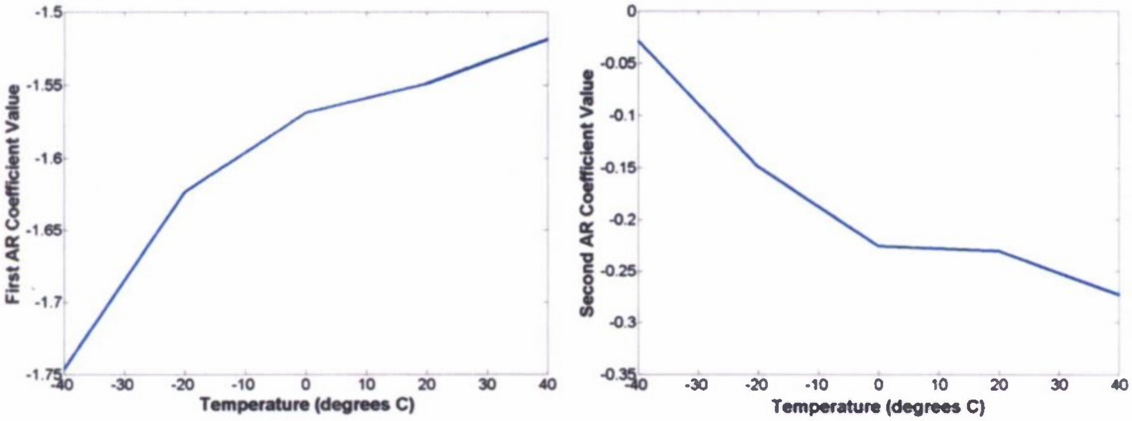

Figure 35. Actual coefficient values vs. temperature for the first (left) and second (right) AR coefficients.

Figure 36 shows the effectiveness of using various order polynomial fits (from linear to fourth order) to determine baseline AR coefficients for intermediate temperatures. It is clear that using baseline AR coefficients determined every 10 degrees Celsius produces better results than using baseline AR coefficients determined every 20 degrees Celsius. In both cases a fourth order polynomial produces the highest percentage of total correct votes over all temperatures with no lower result than 92% for the 5tempbase case and no lower result than 98% for the 9tempbase case. However, because the AR coefficients were being fit to a polynomial the optimal AR coefficients for a particular temperature were not always used, as the polynomial does not necessarily go directly through this known data point.

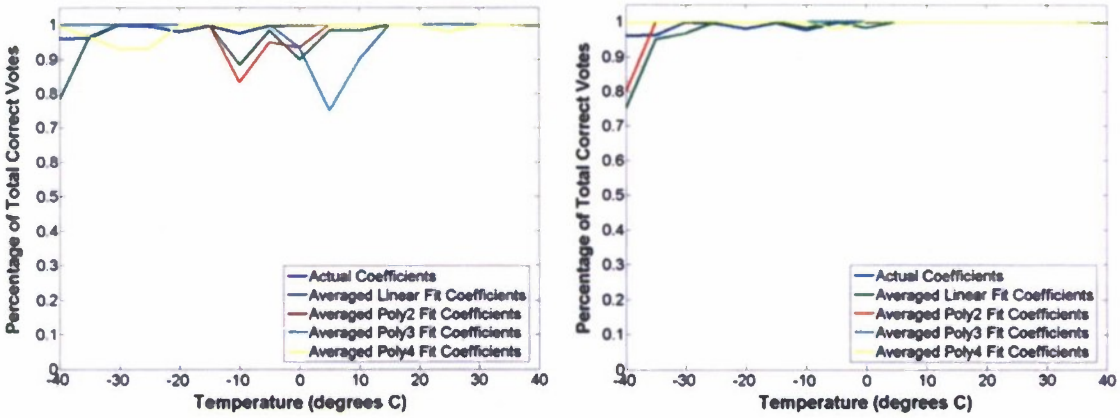

Figure 36. Percentage of total correct votes for various fitting techniques using the 5tempbase (a, left) and 9tempbase (b, right) methods.

Therefore, a lookup table method in which the AR coefficients for temperatures in the baseline database are directly used, and any intermediate temperatures are simply linearly interpolated, is also examined. Figure 37 shows the result of using this method. It is clear that even in the 5tempbase case (baseline AR coefficients determined in 20 degree Celsius increments) that linear interpolation of AR coefficients for intermediate temperatures results in 100% correct classification of individual test cases. This result is not surprising given Figure 35 shows that the AR coefficients trend almost piece-wise linear as temperature changes. This study therefore concludes that the best method for temperature correction is to store baseline coefficients for a small number of temperatures that span the known operational values of the structure and then to linearly interpolate via a lookup table the AR coefficients necessary to correctly classify bond condition for any intermediate temperatures.

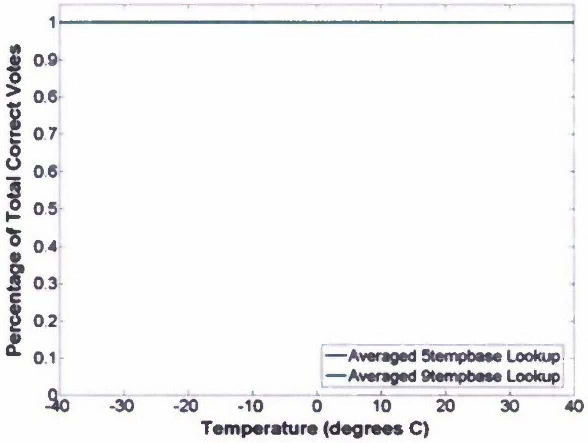

Figure 37. Percentage of total correct votes for direct linear lookup table using the 5tempbase and 9tempbase methods.

4.3.3. Multiple Composite Plates

The previous section showed the ability of the bond state assessment algorithm outlined in this study to compensate for temperature variations (variability due to the environment). Other types of variability that can affect the outcome of this scheme include unintentional inhomogeneities in a single manufactured specimen ("within-unit" variability) and inconsistencies in the manufacturing process itself across specimen lots ("unit-to-unit" variability). Within-unit variability includes the effects of manufacturing variability along the bond line, MFC bond condition inconsistency, and geometric effects that result from different placements of the MFC sensor/actuator pairs. This study examines the ability of the classification scheme to not only to classify disbond size but also to compensate for the different sources of variability discussed above (such as specimen-to-specimen). This classification is performed using data from a similarly configured composite bond for which baseline data are available. The test structures are again analogous to a wing skin-to-spar bonded joint and there is an MFC actuator/sensor pair for each bond condition to be identified on three composite wing-to-spar adhesive bonded joints. The test structures consist of a carbon fiber-reinforced plastic (CFRP) plate (manufactured by McMaster-Carr) that is bonded to a tubular CFRP spar using Loctite® Hysol® 9462 'Two Component Epoxy Adhesive'. The CFRP plate measures 12in x 12in x 0.016in square and the spar again has an outer square diameter of 2in x 2in with a wall thickness of 0.25in. The bonded area for two of the specimens contains two different sizes of disbond (0.25 in^2 and 1.0 in^2) that are created using Teflon inserts. The structures with disbonds are labeled Plate 1 and Plate 2. The third test structure (Plate 3) was manufactured with no disbonds so all paths are undamaged and geometric effects can be studied. The locations of the MFC actuators/sensors for Plate 1 and Plate 2 are pictured in Figure 38. C-scans that depict the bond state of each specimen can be seen in Figure 39.

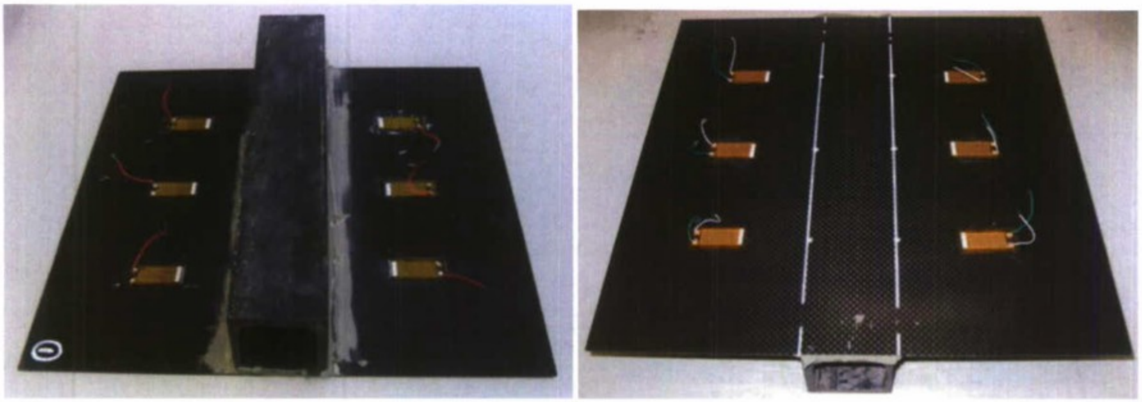

Figure 38. Experimental platform showing location of bottom-mounted MFC actuators on Plate 1 (left) and top-mounted MFC actuators on Plate 2 (right).

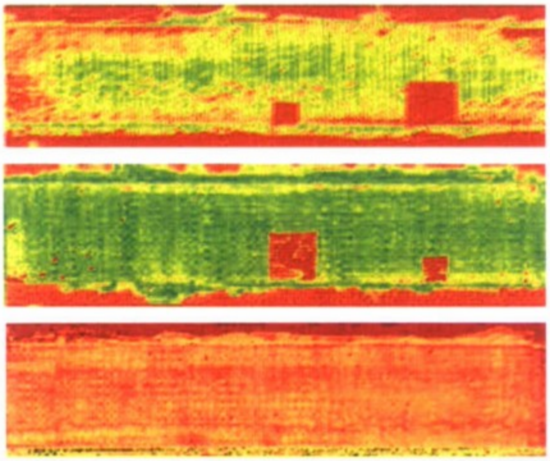

Figure 39. C-scan images showing locations and sizes of disbonds for Plate 1 (top) and Plate 2 (middle) as well as undamaged Plate 3 (bottom).

Plate 1 features two MFC actuator/sensors that are attached to the CFRP plate on each side of the bond for both of the damaged bond states as well as one pair for the undamaged bond area for a total of six MFC patches. The MFC patches are located on the spar side of the bond as seen in Figure 38. The MFC patches on Plate 2 are located on the opposite side of the CFRP plate from the bonded area. Plate 3 also has six MFC patches that are bonded on the spar side of the structure, as in Plate 1. Each of the MFC patches are bonded to the structure using Loctite® Hysol® E120HP™ epoxy adhesive. Each MFC patch is affixed to the structure one inch from the spar bond line. Each input signal is applied to the structure 25 times and then averaged and filtered to reduce experimental noise.

For the following experiments, in order to correctly identify bond condition, 90 time response histories are created using a specific set of signal creation parameters. Half of these 90 generated response time histories are selected as database training inputs. The remaining 45 responses are used as test set inputs. All three bond conditions on each structure are probed three times with the first two time history responses being used for the training database and the remaining responses used to determine bond condition for the test set inputs. In each case the actual bond condition is determined based solely on knowledge it acquired from the 45 database training inputs.

A preliminary study is undertaken to determine the set of input signal parameters and extracted feature parameters (such as AR model order) that produce optimal bond state identification for the new set of test structures. This study uses receiver operating characteristic (ROC) curves as a means of identifying in a rigorous statistical manner the optimal parameters necessary for the classification scheme to operate efficiently, including the choice of alpha (Type-I error) that results in the best trade-off between Type-I and Type-II error.

The classification algorithm can have one of four outcomes for a particular test case. A true positive occurs when the bond being interrogated is damaged and the algorithm also concludes that it is damaged. If the algorithm concludes that this damaged bond is undamaged that is referred to as a false negative. A false positive occurs when the bond being interrogated is undamaged and the algorithm concludes that it is damaged. Similarly, if the algorithm correctly concludes that this undamaged bond is undamaged that is known as a true negative. ROC curves are formed by plotting the rate of true positives found by the classification scheme (true positives divided by true positives plus false negatives) against the false positive rate (false positives divided by false positives plus true negatives). Essentially, the more area under a ROC curve the better job of correctly identifying bond state that particular parameter is doing because there will be a high number of true positives compared to a low number of false positives.

The bond state assessment algorithm is used for an array of signal parameters and the overall ability of each set of parameters to correctly identify each bond state is then examined. In this study a number of excitation center frequencies from 100 kHz to 350 kHz are considered, as well as frequency ratios ranging from 0.15 (slightly chaotic) to 0.50 (highly chaotic). When considering the feature extraction parameters a number of AR model orders from 5 to 30 were employed. Figure 40 depicts the ability of the VCC/EVS-based statistical classification scheme to correctly identify bond condition by plotting the receiver operating characteristic (ROC) curve. This plot depicts the true positive rate against the false positive rate for all possible classifications (both undamaged and damaged). Essentially the more area under a ROC curve the better job of correctly identifying bond state that particular parameter is doing because there will be a high number of true positives compared to a low number of false positives (Type I error).

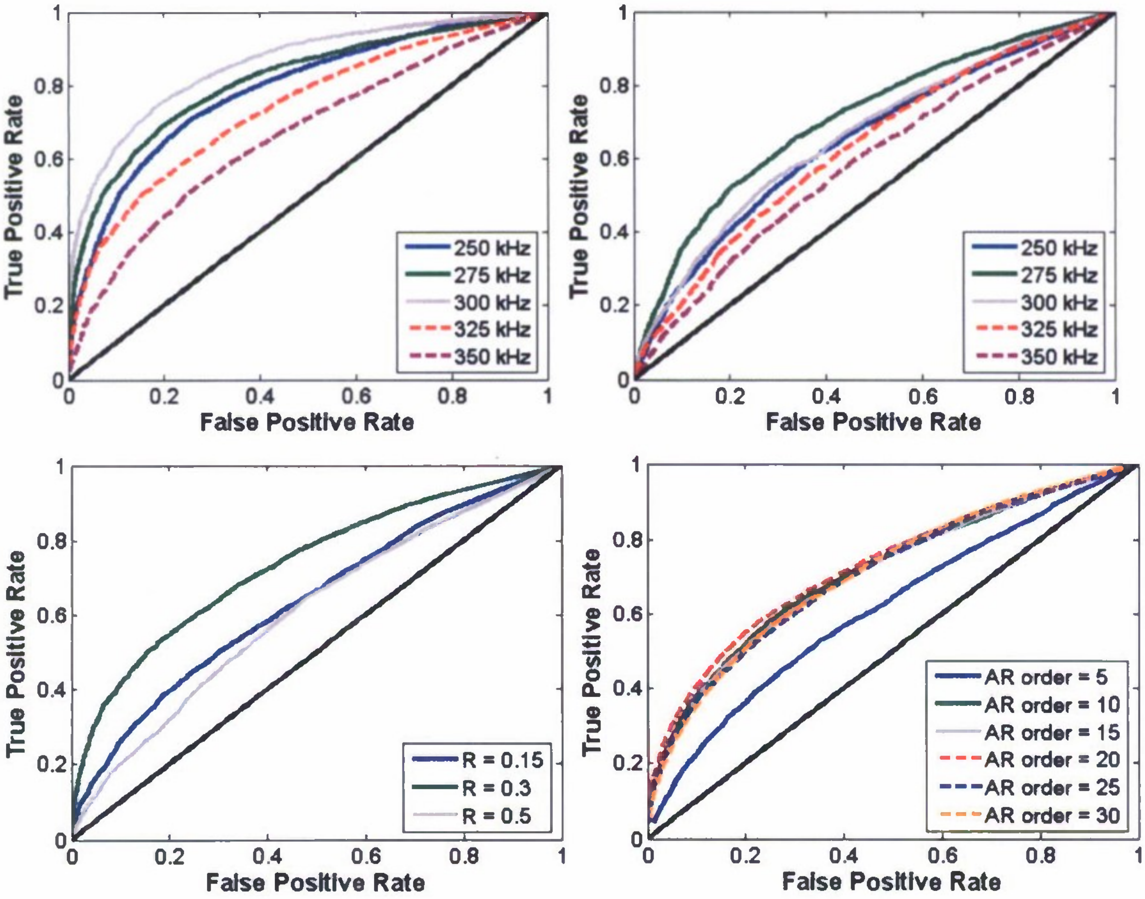

Figure 40. ROC curves for (a, top left) Plate 1 center frequencies, (b, top right) Plate 2 center frequencies, (c, lower left) Plate 1 frequency ratio R and (d, lower right) Plate 1 AR model order.

Figure 40 (top left) shows various ROC curves acquired by changing the center frequency of the excitation signals on Plate 1. Performance of the bond state assessment algorithm increases from a center frequency of 100 kHz up until 300 kHz, at which point the performance degrades as the center frequency continues to increase to 350 kHz (only center frequencies from 250 kHz to 350 kHz are shown here). This means that for the particular geometry of the test specimen and with MFC patches affixed to the same side of the plate as the bond line that a center frequency of 300 kHz is best suited for bond state assessment. Figure 40 (top right) depicts the same change in center frequencies as the top left plot except that the data is from Plate 2 which has the MFC patches bonded on the opposite side of the bonded spar. There is similar behavior to the previous plot in which performance increases from 100 kHz to a particular optimal frequency and then decreases again. However in this case the optimal center frequency is 275 kHz. This change is due to the different way the guided wave propagates through the bond when introduced to the plate on the opposite side of the spar.

Figure 40 (bottom left) shows the ability of the statistical classification scheme employed together with chaotic insonification to correctly identify bond condition for various frequency ratios on Plate 1. A frequency ratio of 0.3 appears to be best suited for bond state assessment. The ROC curves for Plate 2 frequency ratios are very similar and again show that a frequency ratio of 0.3 is optimal. Figure 40 (bottom right) depicts the effect of AR model order on the damage identification ability of the statistical classification scheme. All AR model orders appear to work approximately equally well, except for an order of 5, with an AR model order of 20 performing the best among the group. Again Plate 2 shows similar results for the AR model order. It is not possible to create a ROC curve for Plate 3, as there are no true positive results because there is no damage (and thus, no hypothesis test). Figure 41 shows the optimal ROC curves for Plate 1 and Plate 2.

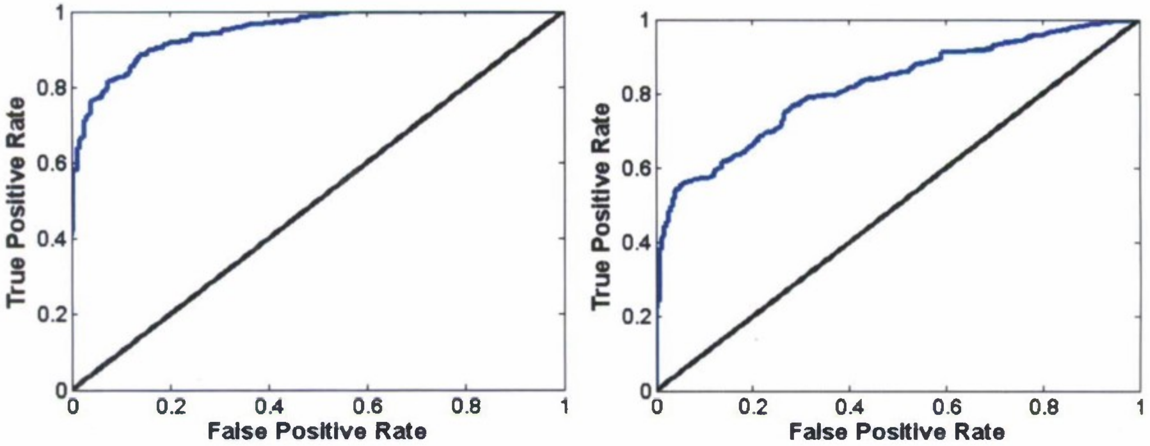

Figure 41. Optimal ROC curves for (a, left) Plate 1 and (b, right) Plate 2.

As with the single plate, this study again employs the use of a thermal chamber to test the efficacy of the above outlined method for multiple plates for temperatures varying from -40°C to 40°C, a range that covers most flight and ground conditions. The optimal set of parameters that will be used in the following experiments is a center frequency of 300 kHz for Plate 1 and Plate 3 (MFC patches on the same side as the bond) and a center frequency of 275 kHz for Plate 2 (MFC patches on the opposite side as the bond). A frequency ratio of 0.3 will be used for all specimens as well as an AR model order of 20. These are the most optimal parameters that were identified using ROC curves in the previous section.

An alpha level of 0.05 (5% type I error) is used to choose the lower confidence limit for the undamaged VCC distribution. Figure 42 shows the percentage of outliers for each bond state being inspected on Plate 1 and Plate 2. This percentage of outliers is plotted against temperature and the "training database" of AR coefficient vectors has been acquired at each temperature. If the percentage of outliers is above the 5% type I error that has been specified, the bond state assessment algorithm has determined that the unknown bond being inspected is damaged.

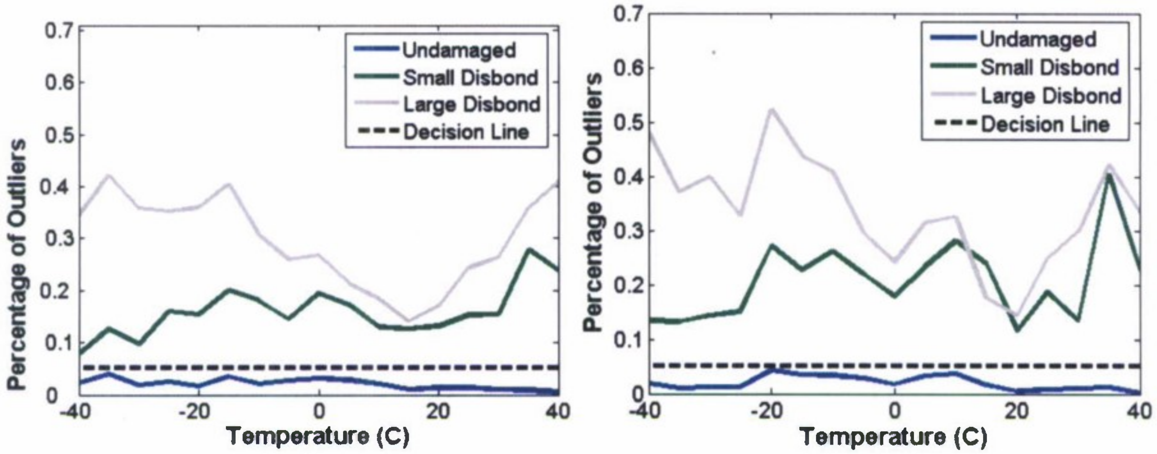

Figure 42. Percentage of outliers vs. temperature for each bond condition on (left) Plate 1, (right) Plate 2.

Figure 42 shows that for every temperature the undamaged path and paths with disbonds are correctly classified because the blue undamaged line is always below the decision boundary and the red and green disbond lines are always above the decision boundary. It is therefore possible to correct for temperature variations by storing baseline AR coefficients for the range of temperatures that the intended apparatus is likely to see during real world applications. However it is not necessary to store AR coefficients for all possible temperatures because only a few temperatures need to be stored and AR coefficients for intermediate temperatures can be linearly interpolated between existing baseline AR coefficients. This study again uses the 5tempbase and 9tempbase methods of AR coefficient interpolation outlined previously. Testing is carried out at 5 degree Celsius temperature increments.

Figure 43 depicts the same results as are seen Figure 42 except that AR coefficient values are linearly interpolated at temperatures for which no baseline data is present. The 5tempbase method depicted in the left-hand plot of Figure 43 works well except for two temperatures at which the number of outliers for the undamaged path rises above the critical threshold. The 9tempbase method shown in the right-hand plot has 100% correct classification at all temperatures. This study reaffirms that the best method for temperature correction is to store baseline coefficients for a small number of temperatures that span the known operational values of the structure and then to linearly interpolate, via a lookup table, the AR coefficients necessary to correctly classify bond condition for any intermediate temperatures.

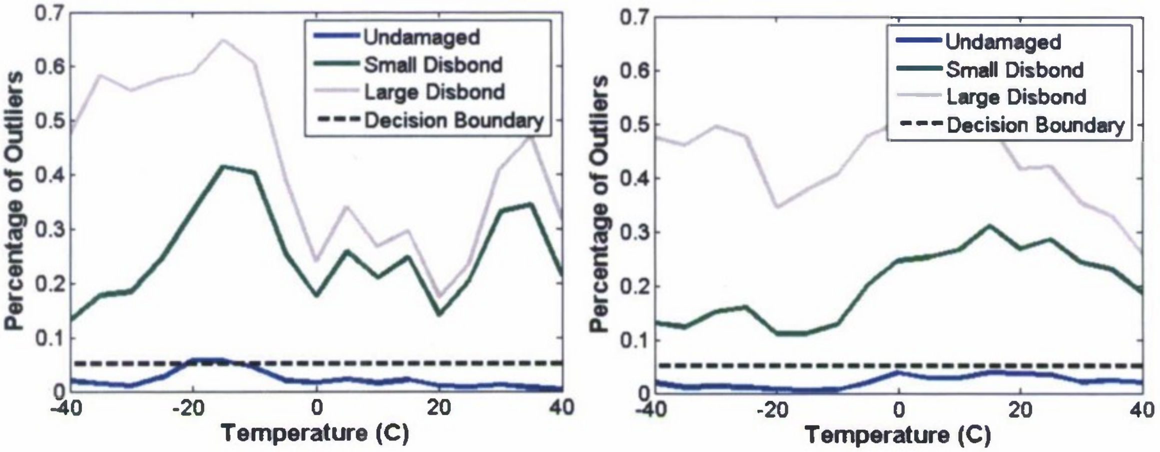

Figure 43. Percentage of outliers for Plate 2 using the 5tempbase (a, left) and 9tempbase (b, right) methods of AR coefficient interpolation.

Having already determined what paths have some form of disbond or damage, the second bond state assessment algorithm employed in this study seeks to classify the size of the disbond. Figure 44 shows the percentage of total correct votes for each disbond size using either the 5tempbase or 9tempbase AR coefficient interpolation method for Plate 1 and Plate 2. The 5tempbase and 9tempbase methods appear to work equally well and the large disbond is correctly identified in almost 100% of individual cases. The small disbond is occasionally misclassified but the lowest result at 15°C on Plate 2 is still greater than 90% correct classification.

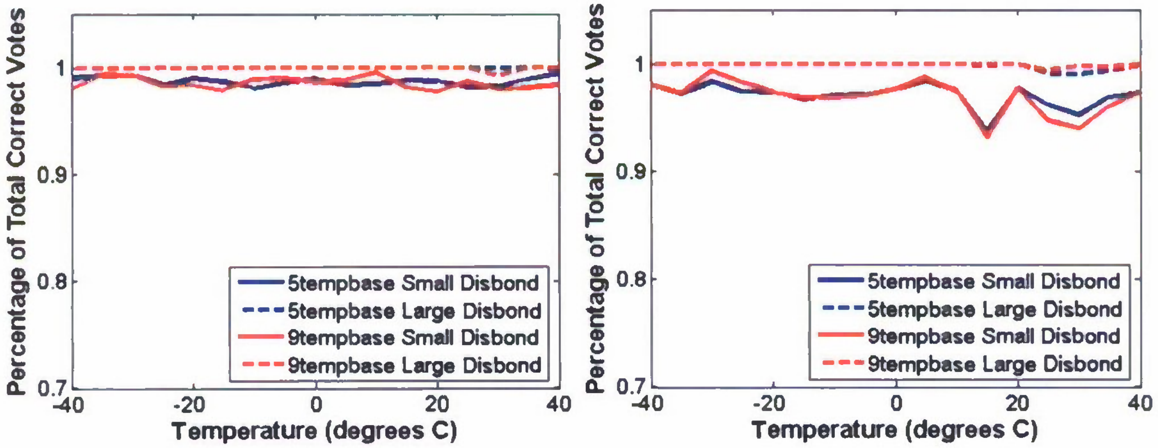

Figure 44. Percentage of total correct votes for each disbond size using the 5tempbase and 9tempbase AR coefficient interpolation methods on Plate 1 (a, left) and on Plate 2 (b, right).

4.3.4. Other Sources of Variability

It is possible to observe the resulting effects of within-unit variability by examining Plate 3, in which all paths were undamaged. Figure 45 shows the number of outliers using the VCC feature for Plate 3. In this figure, one path was chosen to be the baseline undamaged path and the other two paths were used as test cases. The number of outliers for each of the two test undamaged paths is above the 5% threshold but are less than 7.5% and much less than the number of outliers seen in the paths with disbonds on Plate 1 and Plate 2 shown Figure 42. This result only comes from one test structure, but it appears that it may be possible to build a safety factor (in this case 1.5) into the lower confidence limit to account for the various sources of within-unit variability on a particular structure and still be able identify when and where the state of the bond has been changed. This result is important because it means it may not be necessary to store baseline data for every MFC actuator/sensor pair in a structure, as it may be possible to generalize baseline data from elsewhere in the structure as long as the geometries are similar.

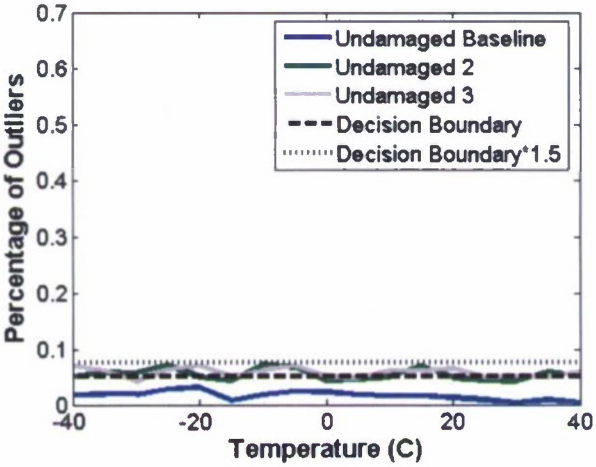

Figure 45. Percentage of outliers vs. temperature for each bond condition on Plate 3.

Unit-to-unit variability arises due to inconsistent manufacturing processes from specimen to specimen, which compound the within-unit sources of variability previously discussed. In well-controlled automated industrial applications with very tight tolerances or requirements, unit-to-unit variability is typically lower than within-unit variability. However, in this study each specimen was manufactured individually by hand, and consequently the unit-to-unit variability is considerably larger than within-unit variability. Figure 46 illustrates the large effect of this manufacturing inconsistency. The left-hand plot shows averaged AR coefficients that are acquired using an AR model order of $p=10$ for the three different bond conditions on Plate 1 and the undamaged bond condition on Plate 3 that is in the same geometric location as the undamaged bond condition on Plate 1. The plot reveals that the AR coefficient vector from the undamaged bond condition on Plate 3 differs as much from the AR coefficient vector from the undamaged bond condition on Plate 1 as the AR coefficient vectors from the two disbond conditions on Plate 1. This large difference between the AR coefficient vectors from the undamaged bond condition in the same geometric location on each plate shows that the unit-to-unit variability is too large to use baseline data gathered on one specimen to discern the damage state of a second specimen. This conclusion is depicted graphically in the right-hand plot of the figure, which shows the percentage of outliers vs. temperature for each bond state on Plate 1 using the undamaged bond condition on Plate 3 as the baseline undamaged condition. The percentage of outliers for the undamaged bond condition on Plate 1 is well above the decision boundary and would therefore be classified as damaged if the undamaged bond condition from Plate 3 were used as a baseline. Thus it is concluded that for the manufacturing techniques used in this study (individual test specimen construction by a non-expert human technician) that unit-to-unit variability is too large to allow for baseline data gathered from one plate to be used to diagnose the bond condition of a second plate. This result does not preclude the possibility that with more controlled manufacturing processes that unit-to-unit variability could be small enough that baseline data from only one specimen would be needed to properly assess the bond condition of a specimen lot.

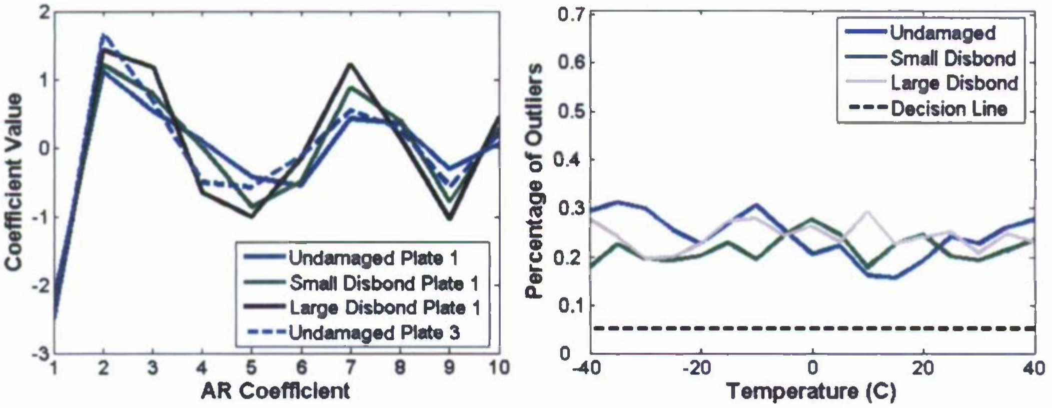

Figure 46. Averaged AR coefficient vector comparison for each bond condition on Plate 1 vs. undamaged bond condition on Plate 3 (left). Percentage of outliers vs. temperature for each bond condition on Plate 1 using baseline data on Plate 3 as the undamaged baseline (right).

4.3.5. Section Summary

This section has shown that the structural health monitoring capability of chaotically modulated ultrasonic waves that are imparted to a composite bonded wing skin-to-spar structure through a piezoelectric patch. The classification damage detection scheme was shown to be effective in identifying bolt preload configuration in experiments on single and multiple joint structures. For the single composite structure experiment in Section 0 the damage size/type classification scheme is shown to be effective in identifying various bond damage states including different disbond sizes as well as poorly cured bonds and has the ability to compensate for temperature variation. This study has also shown the ability of a two-part bond state assessment algorithm to correctly classify the existence and size of a disbond within a composite bonded wing skin-to-spar structure. The use of vector consistency criterion (VCC) values derived from comparison of AR coefficient vectors, in combination with outlier analysis based on extreme value statistics, allows damage existence classification to be possible even without baseline data from every MFC sensor/actuator pair in a structure. Disbond size can then be determined in a supervised learning manner by employing a classification technique derived from information theory. This method also has the ability to compensate for temperature variability provided baseline AR coefficients have been recorded at a suitable number of temperatures that span the operating range of the structure (and that temperature is independently measured *in situ* during operation, which is, in practice, typically done).

5. LIST OF PUBLICATIONS FROM THIS PROJECT

5.1 Archival Journal Articles

[1] T. R. Fasel and M. D. Todd, "Changes in Signal Dimension of Chaotic Ultrasonic Waves During Data Acquisition and Generation," *Structural Health Monitoring: An International Journal*, 2010 (in press)

[2] T. R. Fasel and M. D. Todd, "Chaotic Insonification for Health Monitoring of an Adhesively-Bonded Composite Stiffened Panel," *Mechanical Systems and Signal Processing*, **24**(5), 1420-1430, 2010.

[3] T. R. Fasel and M. D. Todd, "An Adhesive Bond State Classification Method for a Composite Skin-to-Spar Joint Using Chaotic Insonification," *Journal of Sound and Vibration* **329**(15), 3218-3232, 2010.

[4] Srivastava, A. and Lanza di Scalea, F., "Quantitative Structural Health Monitoring by Ultrasonic Guided Waves," *ASCE Journal of Engineering Mechanics*, 136(8), pp. 937-944, 2010.

[5] Srivastava, A. and Lanza di Scalea, F., "Higher-harmonic generation in Nonlinear Waveguides of Arbitrary Cross-section," *Journal of the Acoustical Society of America*, 127(5), pp. 2790-2796, 2010.

[6] T. Fasel, M. B. Kennel, M. D. Todd, E. H. Clayton, M. Stabb, and G. Park, "Damage State Evaluation of Experimental and Simulated Bolted Joints Using Chaotic Ultrasonic Waves," *Smart Structures and Systems*, **5**(4), 329-344, 2009.

[7] Srivastava, A. and Lanza di Scalea, F., "On the Existence of Symmetric or Antisymmetric Lamb Waves at Nonlinear Higher Harmonics," *Journal of Sound and Vibration*, 323 (3-5), pp. 932-943, 2009.

[8] Salamone, S., Fasel, T., Bartoli, I., Srivastava, A., Lanza di Scalea, F., and Todd, M., "Structural Health Monitoring of Adhesively-Bonded Joints in Aerospace Structures," *Materials Evaluation*, Special Issue on Bond Inspection, pp. 828-836, July 2009

[9] Salamone, S., Bartoli, I., Lanza di Scalea, F., and Coccia, S., "Guided-wave Health Monitoring of Aircraft Composite Panels under Changing Temperature," *Journal of Intelligent Materials Systems and Structures*, 20, pp. 1079-1090, 2009.

5.2. Conference Proceedings

[1] Srivastava, A., Bartoli, I., Salamone, S. and Lanza di Scalea, F., “Behavior of Nonlinear Higher Harmonics in Plate and Rod Guided Waves,” Proceedings of 7th International Workshop on Structural Health Monitoring, F-K. Chang, ed., Stanford University, September 9-11, pp. 1832-1839, 2009.

[2] Srivastava, A. and Lanza di Scalea, F., “On the Existence of Antisymmetric or Symmetric Lamb Waves at Nonlinear Higher Harmonics,” Proceedings of SPIE (International Society for Optical Engineering) Smart Structures/NDE 16t^{h} Annual International Symposium – Health Monitoring of Structural and Biological Systems, T. Kundu, ed., San Diego, CA, Vol. 7295, pp. 7295191-72951912, 2009.

[3] Salamone, S., Lanza di Scalea, F. and Bartoli, I., “Temperature Effects in Lamb-wave Structural Health Monitoring Systems,” Proceedings of SPIE (International Society for Optical Engineering) Smart Structures/NDE 16t^{h} Annual International Symposium – Health Monitoring of Structural and Biological Systems, T. Kundu, ed., San Diego, CA, Vol. 7295, pp. 72950O1-72950O12, 2009.

[4] T. R. Fasel, M. Kennel, M. D. Todd, and G. Park, “Damage State Evaluation of Adhesive Composite Joints Using Chaotic Ultrasonic Waves,” Proc. SPIE Smart Structures/NDE 7295, San Diego, California, March 9-12, 2009.

[5] E. Flynn, T. R. Fasel, and M. D. Todd, “The Use Of Evolutionary Algorithms To Tailor Active Sensing Strategies For Enhanced Damage Detection,” 2nd Asia Pacific Workshop on Structural Health Monitoring, Melbourne, Australia, December 2-4, 2008.

[6] T. R. Fasel, M. D. Todd, G. Park, and C. R. Farrar, “Chaotic Ensonification and Pattern Recognition for Joint Assessment,” IECC 2008, Irvine, CA, August 27-29, 2008.

[7] Srivastava, A. and Lanza di Scalea, F., “Quantitative Detection of Bond Defects in Composite Aircraft Panels by Global-Local Ultrasonic Method,” Proceedings of SAMPE Technical

Conference on Materials and Process Innovation: Changing Our World, Long Beach, California, May 18-22, 2008.

[8] T. Fasel, C. C. Olson, and M. D. Todd, "Optimized Guided-Wave Excitations for Health Monitoring of a Bolted Joint," Proc. SPIE Smart Structures/NDE 6935, San Diego, California, March 10-13, 2008.

[9] Srivastava, A., Bartoli, I., and Lanza di Scalea, F., "Global-Local Modeling of Guided Waves for Quantitative Damage Detection," Proceedings of the XXVI International Modal Analysis Conference (IMAC), Society for Experimental Mechanics, Orlando, FL, February 1-3, 2008.

[10] E. H. Clayton, M. B. Kennel, T. R. Fasel, M. D. Todd, M. C. Stabb, and B. J. Arritt, "Active Ultrasonic Joint Integrity Adjudication for Real-time Structural Health Monitoring," Proc. SPIE Smart Structures/NDE 6935, San Diego, California, March 10-13, 2008.

[11] B. J. Arritt, L. M. Robertson, B. K. Henderson, L. Ouyang, S. Beard, E. Clayton, M. D. Todd, A. Zagrai, S. Buckley, J. Ganley, and J. S. Welsh, "Structural Health Monitoring: An Enabler for Responsive Satellites," Proc. SPIE Smart Structures/NDE 6935, San Diego, California, March 10-13, 2008

[12] T. Fasel, M. B. Kennel, M. D. Todd, E. H. Clayton, M. C. Stabb, and G. Park, "Bolted Joint Damage Assessment Using Chaotic Probes," Proceedings of IMAC XXVI: A Conference on Structural Dynamics, Orlando, Florida, February 3-7, 2008.

[13] B. J. Arritt, L. M. Robertson, A. D. Williams, B. K. Henderson, S. Buckley, J. Ganley, J. S. Welsh, L. Ouyang, S. Beard, E. Clayton, M. D. Todd, D. Doyle, and A. Zagrai, "Structural Health Monitoring; an Enabler for Responsive Satellites," Proc. AIAA/ASME/ASCE/AHS/ASC Structures, Structural Dynamics, and Materials Conference, Schaumburg, Illinois, April 7-10, 2008.

6. REFERENCES

Abarbanel, H.D.I. (1996). *Analysis of Observed Chaotic Data*, Springer: New York, NY.

Abbate, A., Koay, J., Frankel, J., Schroeder, S.C. and Das, P. (1997). Signal detection and noise suppression using a wavelet transform signal processor: application to ultrasonic flaw detection, *IEEE Trans. UFFC*, **44**: 14-26.

Allemang, R.J. (2003). The modal assurance criterion – twenty years of use and abuse, *Journal of Sound and Vibration,* **262**(3): 651-675.

Alleyne, D.N., Lowe, M.J.S. and Cawley, P. (1996). The inspection of chemical plant pipework using Lamb waves: defect sensitivity and field experience, In: *Review of progress in quantitative nondestructive evaluation*, Thompson, D.P. and Chimenti, D.E. (eds.), Plenum, New York: 1859–1866.

Al-Nassar Y.N., Datta S.K., Shah A.H. 1991. "Scattering of Lamb Waves by a Normal Rectangular Strip Weldment," *Ultrasonics*, 29: 125-132.

Badii, R., Broggi, G., Derighetti, B., Ravani, M., Ciliberto, S., Politi, A. and Rubio, M.A. (1988). Dimension increase in filtered chaotic signals, *Phys. Rev. Let.,* **60**: 979-982.

Bartoli, I., Marzani, A., Lanza di Scalea, F. and Viola, E. 2006. "Modeling Wave Propagation in Damped Waveguides of Arbitrary Cross-section," *Journal of Sound and Vibration*, 295(3-5):685-707.

Blaise, E. and Chang, F.K. 2001. "Built-in Diagnostics for Debonding in Sandwich Structures Under Extreme Temperatures," *Proc. 3rd Int'l Workshop on Structural Health Monitoring*, Stanford University, CA, 154-163.

Boller, C. and Staszewski, W.J. (2004). Aircraft structural health and usage monitoring, *Health Monitoring of Aerospace Structures – Smart Sensor Technologies and Signal Processing,* W.J. Stazewski, *et al.*, Eds. Wiley: Chichester, West Sussex, UK.

Bray, D. and McBride, D. (1992). *Nondestructive Testing Techniques*, John Wiley & Sons: New York.

Brockwell, P.J. and Davis, (1991) *Time Series: Theory and Methods,* Springer, New York, pp.113-118

Broomhead, D.S. and King, G.P. (1986). Extracting qualitative dynamics from experimental data, *Physica D*, **20**: 217-236.

Broomhead, D.S., Huke, J.P. and Muldoon, M.R. (1992). Linear filters and non-linear systems, *J. Royal Stat. Soc. B,* **54**: 373-382.

Bursi, O.S. and Jaspart, J.P. (1997). Basic issues in the finite element simulation of extended end plate connections, *Computers and Structures,* **43**: 17–42.

Bursi, O.S. and Jaspart, J.P. (1998). Benchmarks for finite element modeling of bolted steel connections, *Journal of Construction Steel Research,* **69**: 361–382.

Castaings, M., Cawley, P. and Farlow, R. (1996). Air-coupled ultrasonic transducers for the detection of defects in plates, In: *Review of progress in quantitative nondestructive evaluation*, Thompson, D.P. and Chimenti, D.E. (eds.), Plenum, New York: 1083–1090.

Castillo, E. (1988). *Extreme Value Theory in Engineering*, Academic Press, San Diego.

Chambers, J.T., Wardle, B.L. and Kessler, S.S. 2006. "Durability Assessment of Lamb Wave-based Structural Health Monitoring Nodes," *Proc. 47th AIAA/ASME/ASCE/AHS/ASC Structures, Structural Dynamics, and Materials Conference*, Newport, RI, Paper #AIAA-2006-2263.

Chamis, C.C. 1984. "Simplified Composite Micromechanics Equations for Hygral, Thermal, and Mechanical Properties," *SAMPE Quarterly,* 15(3):14–23.

Chang Z. and Mal A.K. 1995. "A Global Local Method for Wave Propagation across a Lap Joint," *Numerical Methods in Structural Mechanics ASME,* 204:1-11.
Crawley, E.F. and de Luis, J. 1987. "Use of Piezoelectric Actuators as Elements of Intelligent Structures," *AIAA Journal*, 25:1373-1385.

Davies, M.E. and Campbell, K.M. (1996). Linear recursive filters and nonlinear dynamics, *Nonlinearity*, **9**: 487-99.

Davies, M.E. (1997). Reconstructing attractors from filtered time series, *Phys. D,* **101**: 195-206.

Flynn, E. and Todd, M.D. (2009). Optimal placement of piezoelectric actuators and sensors for detecting damage in plate structures, *Journal of Intelligent Material Structures and Systems*, doi:10.1177/1045389X09338080.

Fraser, A.M. and Swinney, H.L. (1986). Independent coordinates for strange attractors from mutual information, *Physical Review,* **33:** 1134-40.

Giurgiutiu, V. and Zagrai, A. (2002). Embedded self-sensing piezoelectric active sensors for on-line structural identification, *ASME J. Vib. Acoust.*, **124**: 116-125.

Giurgiutiu, V. 2005. "Tuned Lamb Wave Excitation and Detection with Piezoelectric Wafer Active Sensors for Structural Health Monitoring," *Journal of Intelligent Materials Systems and Structures*, 16:291-305.

Goetschel D.B., Dong S.B. and Muki R. 1982. "A Global Local Finite Element Analysis of Axisymmetric Scattering of Elastic Waves," *Transactions of the ASME,* 49:816-820.

Griffiths, B. (2005). Boeing sets pace for composite usage in large civil aircraft, *High Performance Composites*, May Issue.

Guyott, C.H., Cawley, P. and Adams, R.D. (1986). The non-destructive testing of adhesively bonded structures, *Journal of Adhesion*, **20**: 129-159.

Guyott, C.H. and Cawley, P. (1988). Evaluation of cohesive properties of adhesive joints using ultrasonic spectroscopy, *NDT International*, **21**: 233-240.

Hayashi T., Song W.J. and Rose, J.L. 2003. "Guided Wave Dispersion Curves for a Bar with an Arbitrary Cross-section: A Rod and Rail Example," *Ultrasonics*, 41:175-183.

Hooker, M.W. 1998. *Properties of PZT-Based Piezoelectric Ceramics Between –150 and 250° C*, Technical report NASA/CR-208708.

Jones, R.M. 1975. *Mechanics of Composite Materials*, Hemisphere Publishing Corporation, New York.

Kennel, M.B. and Abarbanel, H.D.I. (1992). Determining embedding dimension for phase-space reconstruction using a geometrical construction, *Physical Review A,* **45**: 3403-11.

Kim, Y.H., Kim, D.H., Han, J.H. and Kim, C.G. 2007. "Damage Assessment in Layered Composite Using Spectral Analysis and Lamb Wave," *Composite: Part B*, 38:800-809.

Konstantinidis, G., Drinkwater, B.W. and Wilcox, P.D. 2006. "The Temperature Stability of Guided Wave Structural Health Monitoring Systems," *Smart Materials and Structures*, 15:967-976.

Lanza di Scalea, F., Matt, H., Bartoli, I., Coccia, S., Park, G. and Farrar, C. 2007. "Health Monitoring of UAV Wing Skin-to-spar Joints Using Guided Waves and Macro Fiber Composite Transducers," *Journal of Intelligent Materials Systems and Structures*, 18:373-388.

Lanza di Scalea, F. and Salamone, S. 2008. "Temperature Effects in Ultrasonic Lamb Wave Structural Health Monitoring Systems," *Journal of the Acoustical Society of America*, 124(1):161-174.

Lee, B.C., Manson, G. and Staszewski, W.J. 2003. "Environmental Effects on Lamb Wave Responses from Piezoceramic Sensors," *Materials Science Forum,* 440-441: 195-202.

Lee, H-L. and Saravanos, D.A. 1998. "The Effect of Temperature Dependent Material Properties on the Response of Piezoelectric Composite Materials," *Journal of Intelligent Materials Systems and Structures*, 9:503-508.

Lu, Y. and Michaels, J.E. 2005. "A Methodology for Structural Health Monitoring With Diffuse Ultrasonic Waves in the Presence of Temperature Variations," *Ultrasonics*, 43:717-731.

Mal A.K. and Chang Z. 1999, "Scattering of Lamb Waves from a Rivet Hole with Edge Cracks," *Mechanics of Materials,* 31:197-204.

Mal A.K. and Chang Z. 2000, "A Semi-Numerical Method for Elastic Wave Scattering Calculations," *International Journal of Geophysics,* 143:328-334.

Michaels, J.E. and Michaels, T.E. 2005. "Detection of Structural Damage from the Local Temporal Coherence of Diffuse Ultrasonic Signals," *IEEE Transactions on Ultrasonics, Ferroelectrics and Frequency Control*, 52:1769-1782.

Moniz, L., Pecora, L., Nichols, J., Todd, M.D. and Wait, J.R. (2004). Dynamical assessment of structural damage using the continuity statistic, *Structural Health Monitoring,* **3**(3):199-212.

Nichols, J.M., Todd, M.D. and Wait, J.R. (2003). Using state space predictive modeling with chaotic interrogation in detecting joint preload loss in a frame structure experiment, *Smart Materials and Structures,* **12**(4): 580-601.

Nichols, J.M., Todd, M.D., Virgin, L.N. and Nichols, J.D. (2003). On the use of attractor dimension as a feature in structural health monitoring, *Mech. Syst. Signal. Process.*, **17**(6): 1305-1320.

Nichols, J.M., Todd, M.D., Seaver, M. and Virgin, L.N. (2003). Use of chaotic excitation and attractor property analysis in structural health monitoring, *Phys. Rev. E,* **67**: 016209.

Nichols, J.M., Nichols, C.J., Todd, M.D., Seaver, M., Trickey, S.T. and Virgin, L.N. (2004). Use of data driven phase space models in assessing the strength of a bolted connection in a composite beam, *Smart Materials and Structures*, **13**: 241-250.

Olson, C.C., Todd, M.D., Worden, K., and Farrar, C. (2007). Improving Excitations for Active Sensing in Structural Health Monitoring via Evolutionary Algorithms, *Journal of Vibration and Acoustics*, **129**, 784-802.

Olson, C.C., Overbey, L.A., and Todd, M.D. (2009). An experimental demonstration of tailored excitations for improved damage detection in the presence of operational variability, *Mechanical Systems and Signal Processing*, **23**(2): 344-357.

Olson, C.C., Overbey, L.A., and Todd, M.D. (2009). The effect of detection feature type on excitations bred for active sensing in structural health monitoring, *Journal of Intelligent Material Systems and Structures*, **20**(11): 1307-1327.

Pecora, L.M. and Carroll, T.L. (1996). Discontinuous and nondifferentiable functions and dimension increase reduced by filtering chaotic data, *Chaos*, **6**: 432-439.

Pecora, L.M., Carroll, T.L. and Heagy, J.F. (1997). Statistics for continuity and differentiability: An application to attractor reconstruction from time series, *Fields Institute Communications*, **11**.

Pilarski, A. and Rose, J.L. (1992). Lamb wave mode selection concepts for interfacial weakness analysis, *J. Nondestr. Eval.*, **11**: 237-249.

Raghavan, A. and Cesnik, C.E.S. 2007. "Studies on Effects of Elevated Temperature for Guided-wave Structural Health Monitoring," *Proceedings SPIE*, vol. 6529, 65290A1-65290A12.

Rattanawangcharoen N., Zhuang W., Shah A.H. and Datta S.K. 1997, "Axisymmetric Guided Waves in Jointed Laminated Cylinders," *Journal of Engineering Mechanics,* 123:1020-1026.

Rose, J.L. 1999. *Ultrasonic Waves in Solid Media*. Cambridge, UK: Cambridge University Press.

Sabra K., Srivastava A., Lanza di Scalea F., Bartoli I., Rizzo, P. and Conti, S. 2008, "Structural Health Monitoring by Extraction of Coherent Guided Waves from Diffuse Fields," *Journal of the Acoustical Society of America*, 123:EL8-EL13.

Schulz, M.J., Sundaresan, M.J., McMichael, J., Clayton, D., Sadler, R. and Nagel, B. 2003. "Piezoelectric Materials at Elevated Temperature," *Journal of Intelligent Materials Systems and Structures*, 14:693-705.

Sauer, T., Yorke, J. and Casdagli, M. (1991). Embedology, *J. Stat. Phys.*, **65**: 579-616.

Schreiber, T. (1997). Detecting and analyzing nonstationarity in a time series with nonlinear cross predictions, *Phys. Rev. Lett.,* **78**: 843-846.

Seifried, R., Jacobs, L.J. and Qu, J. (2002). Propagation of guided waves in adhesive bonded components, *NDT&E Int.*, **35**: 317-328.

Shannon, C.E. and Weaver, W. (1949). *The Mathematical Theory of Communication,* University of Illinois Press, Chicago, pp. 75-83.

Sherrit, S., Yang, G., Wiederick, H.D. and Mukherjee, B.K. 1999. "Temperature Dependence of the Dielectric, Elastic, and Piezoelectric Material Constants of Lead Zirconate Titanate (PZT) Ceramics," *Proc. Smart Materials, Structures and Systems*, Bangalore, India, 121-126.

Sodano H.A., Park, G. and Inman, D.J. 2004. "An Investigation into the Performance of Macro Fiber Composites for Sensing and Structural Vibration Applications," *Mechanical Systems and Signal Processing*, 18:683- 697.

Sohn, H., Park, G., Wait, J. R., Limback, N. P., and Farrar, C. R. 2003. "Wavelet-based Active Sensing for Delamination Detection in Composite Structure," *Smart Materials and Structures*, 13:153–160.

Sohn, H. and Farrar, C.R. (2001). Damage diagnosis using time series analysis of vibration signals, *Smart Materials and Structures*, **10**(3): 446-451.

Sohn, H., Farrar, C.R., Hunter, N.F. and Worden, K. (2001) Structural health monitoring using statistical pattern recognition," *J. Dyn. Syst. Meas. Control*, **123**: 706-711.

Sohn, H., Farrar, C.R., Hemez, F.M., Shunk, D.D., Stinemates, D.W. and Nadler, B.R. (2003). A review of structural health monitoring literature: 1996 – 2001, *Los Alamos National Laboratory report*, LA-13976-MS.

Staszewski W., Boller C. and Tomlison G. 2004, *Health Monitoring of Aerospace Structures*, Wiley and Sons, West Sussex, England.

Todd, M.D., Nichols, J.M., Pecora, L.M. and Virgin, L.N. (2001). Vibration-based damage assessment utilizing state space geometry changes: Local attractor variance ratio, *Smart Materials and Structures,* **10**: 1000-1008.

Todd, M.D., Erickson, K., Chang, L., Lee, K. and Nichols, J.M. (2004). Using chaotic interrogation and attractor nonlinear cross-prediction error to detect fastener preload loss in an aluminum frame, *Chaos: An Interdisciplinary Journal of Nonlinear Science,* **14**(2): 387-399.

Wilkie, W.K., Bryant, R.G., High, J.W., Fox, R.L., Hellbaum, R.F., Jalink, A., Little, B.D. and Mirick, P.H. 2000. "Low-cost Piezocomposite Actuator for Structural Control Applications," *Proceedings SPIE*, vol. 3991, 323-334

Williams, R.B., Inman, D.J. and Wilkie, W.K. 2004. "Temperature-dependent Thermoelastic Properties for Macro Fiber Composite Actuators," *Journal of Thermal Stresses*, 27:903–915.

Worden, K., Sohn, H. and Farrar, C.R. 2002. "Novelty Detection in a Changing Environment: Regression and Interpolation Approaches," *Journal of Sound and Vibration*, 258(4):741-761.
Worden, K., Allen, D.W., Sohn, H., Stinemates, D.W. and Farrar, C.R. (2002). Extreme value statistics for damage detection in mechanical structures, *Los Alamos National Laboratory Report,* LA-13903-MS.

Worden, K., and Manson, G. (2007). The application of machine learning to structural health monitoring, *Philosophical Transactions of the Royal Society A*, **365**: 515-37.

Xu, P.C., Mal, A.K. and Bar-Cohen, Y. (1990). Inversion of leaky Lamb wave data to determine cohesive properties of bonds, *Int. J. Eng. Sci.*, **28**: 331-346.